

DIGITAL ACCESS TO SCHOLARSHIP AT HARVARD

Engineered potentials and dynamics of ultracold quantum gases under the microscope

The Harvard community has made this article openly available. Please share how this access benefits you. Your story matters.

Citation	No citation.
Accessed	February 19, 2015 4:26:19 PM EST
Citable Link	http://nrs.harvard.edu/urn-3:HUL.InstRepos:12274204
Terms of Use	This article was downloaded from Harvard University's DASH repository, and is made available under the terms and conditions applicable to Other Posted Material, as set forth at http://nrs.harvard.edu/urn-3:HUL.InstRepos:dash.current.terms-of-use#LAA

(Article begins on next page)

HARVARD UNIVERSITY
Graduate School of Arts and Sciences

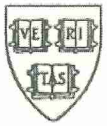

DISSERTATION ACCEPTANCE CERTIFICATE

The undersigned, appointed by the

Department of Physics

have examined a dissertation entitled

Engineered potentials and dynamics of ultracold quantum gases under the microscope

presented by Ruichao Ma

candidate for the degree of Doctor of Philosophy and hereby certify that it is worthy of acceptance.

Signature _____

Typed name: Professor Markus Greiner, Chair

Signature _____

Typed name: Professor Eugene Demler

Signature _____

Typed name: Professor Marko Loncar (SEAS)

Date: May 9, 2014

Engineered potentials and dynamics of ultracold quantum gases under the microscope

A dissertation presented

by

Ruichao Ma

to

The Department of Physics

in partial fulfillment of the requirements

for the degree of

Doctor of Philosophy

in the subject of

Physics

Harvard University

Cambridge, Massachusetts

May 2014

© 2014 Ruichao Ma

All rights reserved.

Dissertation Advisor:
Professor Markus Greiner

Author:
Ruichao Ma

Engineered potentials and dynamics of ultracold quantum gases under the microscope

Abstract

In this thesis, I present experiments on making and probing strongly correlated gases of ultracold atoms in an optical lattice with engineered potentials and dynamics. The quantum gas microscope first developed in our lab enables single-site resolution imaging and manipulation of atoms in a two-dimensional lattice, offering an ideal platform for quantum simulation of condensed matter systems. Here we demonstrate our abilities to generate optical potential with high precision and high resolution, and engineer coherent dynamics using photon assisted tunneling. We also create a system of bilayer quantum gases that brings new imaging capabilities and extends the possible range of our quantum simulation.

To engineer precise optical potentials, we tackle uncontrolled disorder using incoherent light sources and Fourier filtering of lattice beams. We develop a spatially incoherent light source which suppresses disorder caused by defects and scattering in the imaging system. Digital micro-mirror devices are used as spatial light modulators to shape arbitrary potentials with single site resolution.

Next we study photon-assisted tunneling as an example of driven coherent dynamics. We observe sharp, interaction-shifted photon-assisted tunneling resonances, and resolve the multi-orbital shifts. Using photon-assisted tunneling, we drive a quantum phase transition between a paramagnet and an anti-ferromagnet, and observe quench dynamics

at the critical point.

We prepare tunnel-coupled bilayer systems, and use interaction blockade to engineer occupation-dependent inter-plane transport. The site resolved imaging of the bilayer system allows us to circumvent the limitations of parity imaging to directly observe the Mott insulator "wedding cake" structure and density ordering in the anti-ferromagnetic state, and to perform spin-resolved readout of a hyperfine mixture.

Contents

Acknowledgments

The majority of my time over the last five years was spend with the members of the Greiner lab. I have had a great deal of fun working with all of them, day and night, rain or shine.

First of all, I would like to thank my Ph.D. advisor Professor Markus Greiner for taking me under his wings, and for his support and encouragement throughout my years at Harvard. He gives us the freedom to do what we love in lab and decide on the directions to take, yet he is always ready to provide insights and advice on the bigger pictures of the experiment. His expertise in optics and anything light-related never stops to amaze me, and I have learned an enormous amount from him as an experimental physicist.

Waseem Bakr and Amy Peng were the senior graduate students when I first joined the Rubidium experiment, and I thank them for teaching me all about the experiment. Waseem holds the ultimate knowledge and understanding of the machine. He can explain almost any physics question I raised in the lab with such deep intuition, and reading his writing or listening to his talks is simply a pleasure. His efficiency in getting things done is also something I have tried to emulate.

Jonathan Simon was our postdoc who led the experiment during the middle part of my time in the lab. His great many experimental ideas kept us busy for a long time. I benefited a lot from his patient explanations and guidance through thought-provoking questions. It's amazing and inspiring how Jon can write so many Mathematica calculations as if it's his entertainment, which I tried to learn although with very limited progress.

Eric Tai and I entered Harvard the same year, and Philipp Preiss is a year below me. We worked together for the most part of my Ph.D., and I am most grateful for

having the two of them by my side (quite literally too in our busy office). Eric's passion and obsession for precise engineering is impressive, and I wish I can design and build beautiful boards / boxes like he does. And our experiment will benefit from the new control system he built for many years to come. Philipp is the most organized of us all, which is apparent just looking at our notebooks. He has been spearheading many of our recent experimental efforts, and his hard work, calm opinions and suggestions, and good visions have kept the team moving forward.

Rajibul Islam is the second postdoc I worked with, who brought with him his expertise in trapped ions and has been providing valuable inputs for experimental ideas.

Alex Lukin and Matthew Rispoli are the youngest members of the Rubidium team, and they have already brought plenty of laughter to the lab. They are hardworking, quick and eager to learn. I have no doubt that they will have fun and do great science.

The Greiner lab is not complete without all members of the Lithium lab. I thank Florian Huber for teaching all of us about electronics, machining and a whole lot more – I miss the days of the lab RC helicopter fights and I will never forget the wonderful coaching I received from Florian at my first ever ski trip. I thank Widagdo Setiawan for his fresh perspectives and sharp insights, and the cotton candy and mega chocolate bar that kept the lab from starving. I want to thank Kate Wooley-Brown for her blankets from Secret Santa, which kept me warm during the long nights babysitting the experiment. I thank Max Parsons, Sebastian Blatt, and the younger generation Anton Mazurenko, Christie Chiu and Peter Lu, for all the discussions we had and time spent together.

I also enjoyed my time with our visiting students Philip Zupancic, Dylan Cotta, and Gregor Jotzu. In particular I want to thank Philip Zupancic for his wonderful work in building the spatial light modulator setup.

Life at Harvard is enjoyable and exhilarating, but there can always be moments

of confusion, disappointment, or simply bad days. I am most indebted to all the people who have helped me along the way, for their understanding and wholehearted support, and for their kindest encouragement even after I have sometimes let them down. Especially, I thank Jon, Tout Wang, and Philipp for dragging me out of whatever dark corners I have had myself stuck in, at various times. I thank Leizhi Sun for being a great roommate for the last three years, from whom I have heard inspiring journeys. I want to thank Yin Yu for her invaluable encouragement during the writing of this thesis.

I have met numerous wonderful people during my time here which I will not be able to enumerate, and I feel extremely lucky to have them around. I thank people I have worked with in Harvard CSSA, particularly Xu Zhang, Kecheng Li, Lilei Xu, Yu Lei and Tao Tong – we shared many memorable moments. I thank my floor-mates back in Richards Hall for a colorful first year at Harvard, and thank especially Jing Yang for being the best Resident Advisor.

I want to thank all fellow HFLSers at Harvard over the years. I am constantly reminded of our bonds and common believes, how far we've all come along and how far we all aim to go. Among them, Ella Shengru Chou, Colin Jia Zheng and Song He who kept me company the first two years in Cambridge; and Yuyu Feng who is always understanding and encouraging.

I am grateful to all the faculty members and students in and outside of the Center for Ultracold Atoms who have taught me or given me guidance. I miss my fellow classmates in Physics with whom I spent countless nights doing problem sets together in the G1 area. I am also really grateful to all the administrative staff in the Department of Physics for their kind support.

I own my gratitude to faculties and friends back at Nanyang Technological University in Singapore. Especially, I would like to thank my undergraduate research advisor

Associate Professor Rainer Dumke for introducing me into the absolutely awesome field of ultracold atoms and teaching me to become an experimentalist. And Professor Alfred Huan, then department head, for his guidance and inspiration.

Lastly, I would like to thank my parents and grandparents for their love, support and upbringing. I simply would not be here without them.

To my parents for their love and support

Chapter 1

Introduction

Many of the open questions in condensed matter physics today deal with materials with intriguing properties and hence often potential applications. Some examples include high-temperature superconductors [1], fractional quantum Hall systems [2], and low-dimensional magnetic materials [3]. These materials all exhibit strong non-classical correlations due to the strong interactions between the constituent quantum particles, e.g. Coulomb interaction between electrons [4].

Various quantum theories have been put forward that are thought to capture the essential physics of these strongly correlated many-body systems. But despite the simple forms of the Hamiltonians, the theoretical understanding of these proposed models are often very limited. They have no analytical solutions and numerical studies of states with large system size/particle number require formidable resources on classical computers. The dynamics of these systems are even harder to tackle theoretically and numerical methods exist for only a selective range of problems.

Consider a collection of spins each of which can take one of two possible states - spin up or state down. For a classical system, the spin is either up or down. Hence one bit of information is needed for specifying each spin, and the total amount of

information resources to fully describe the state of a classical system scales linearly with the number of particles N. For a quantum system, however, the spins can be in a quantum superposition of all possible spin configurations, in this case 2^N of them, so the number of parameters needed to specify the quantum state scales exponentially with system size. This is a direct result of quantum entanglement in strongly correlated systems, where the states of the constituent particles are highly correlated and can not be treated independently. Given the same available resource on a classical computer, calculating the properties of a quantum mechanical problem could take exponentially longer time than calculating its classical counterpart. Modern computers today allow physicists to exactly simulate usually only a handful of quantum particles. If Moore's law [5] is to be followed, the doubling of classical computer's computational power every two years will only allow us to simulate *one* extra quantum particle in the same time period.

A solution to this problem is the use of quantum simulators, as first proposed by Richard Feynman [6]: in order to simulate a hard and less accessible quantum system, one could use another quantum system that is governed by the same physics (i.e. mathematically equivalent Hamiltonians) but is designed to be easier to control and probe. Recent developments in the field of atomic, molecular and optical physics have made it possible to build quantum simulators in several platforms including cold neutral atoms [7], trapped ions [8], superconducting circuits [9], or photonic systems [10]. These quantum simulators would allow us to test existing models and help us understand strongly correlated material like quantum magnets or high-T_c superconductor. They also allow us to explore systems with exotic properties in parameter regimes not thought to be occurring in nature.

Ultracold atom in optical lattices is a powerful platform for quantum simulation of condensed matter systems [11]. Systems of ultracold atoms cooled into quantum

regime (e.g. Bose-Einstein condensate, or degenerate fermi gas) can be brought into the strongly correlated regime by using Feshbach resonances [12] or optical lattices [13]. Atoms moving in the periodic light potential is analogous to electrons moving in the periodic potential of the ions in solids. Although fermionic atoms would seem more natural for simulating electron gases with the proper quantum statistics, bosonic atoms in lattices are also interesting and can for example represent Cooper pairs in superconductors.

These systems of ultracold atoms offer several advantages: They are clean, essentially dissipation free with long coherence times, required for maintaining entanglement and correlations during the quantum simulation. They offer large tunability over many parameter: for example the lattice spacing and geometries can be altered by changing the laser configuration. The lattice spacings of optical lattices are on the order $\sim 1\mu m$, which is much larger than the lattice spacing in condensed matter systems. This enables optical manipulation and imaging of the quantum states at each lattice site. The much lower energy scales in ultracold atom systems also makes it easier to observe the real-time dynamics of the quantum evolution.

One challenge brought by the small energy scales in lattices (typically in the nano-Kelvin regime) is the extremely low temperatures required to reach the quantum regime where the strongly correlated states emerge. Compared to bosons, Pauli exclusion makes fermions even harder to cool. While systems of ultracold atoms in optical lattices have been cooled to below the energy scales of the direct tunneling to observe e.g. the superfluid to Mott insulator quantum phase transition, the progress towards observing super-exchange based magnetic ordering (e.g. the anti-ferromagnetic ground state of the Fermi Hubbard model) remains limited and extremely challenging. A lot of cooling methods are being investigated to reach the required temperatures [14].

Until recently, experiments with ultracold atoms in optical lattices are mostly studied

using their bulk properties, similar to traditional condensed matter techniques. The development of "quantum gas microscopes" [15, 16, 17] allowed for the first time the ability to image and manipulate single atoms in an optical lattice. With such high resolution imaging, one can probe the local properties of the many body state without having to resort to ensemble averages and directly access the correlation functions in the systems of interest [18, 19, 20]. The same imaging system can also be used to project optical potentials with single site resolution, making it possible to create more complex Hamiltonians, and to prepare intriguing initial states with high fidelity for quantum simulation. Such control of individual atoms in a lattice also makes the system a promising venue for quantum information processing, where the quantum registry can be initialized with high fidelity using e.g. our low entropy Mott insulators, and the qubits can be encoded in either the location or the hyperfine spin of the atoms.

In this thesis, we develop techniques and describe experiments that improve and extend the capabilities of our bosonic quantum gas microscope as a quantum simulator. They are focused on three different aspects:

(1) *Engineer potential landscapes* – Precise shaping of the light potential is necessary for reliable quantum simulation, and the ability to create arbitrary potentials with single site resolution enables the preparation of novel initial states and local excitations.

(2) *Engineer dynamics* – This together with (1) makes it possible to generate a broader range of interesting Hamiltonians with strongly correlated states.

(3) *Improve imaging techniques* – To extend the high resolution imaging to more systems, e.g. more than a single 2D plane, or for multiple spin states.

A quick summary of these experiments are provided as follows, according to the organization of the rest of the thesis:

- Chapter 2 introduces the theory of cold bosons in optical lattices. We summarize the band structure in a lattice, and the mapping to the Bose Hubbard model. The superfluid and Mott insulator states are discussed, together with a description of the mean field phase diagram.

- Chapter 3 gives an overview of the experimental apparatus, the quantum gas microscope. We summarize the typical experimental sequence, including the creating of the ^{87}Rb Bose-Einstein condensate, the loading into the 2D plane, the projection of the lattice and other optical potentials, and the fluorescence imaging scheme with single site resolution.

- Chapter 4 focuses on the techniques used in our experiments to create clean potentials and reduce uncontrolled disorder, crucial for any reliable quantum simulation. We describe the use of temporally incoherent light sources. The Fourier filtering setup for the 2D lattice is shown. We also show a method to create spatially incoherent light sources, and experimentally test their performance in reducing disorder in projected potentials. A few different methods of characterizing the disorder is discussed.

- Chapter 5 continues with the topic of engineered potentials, and describe the use of spatial light modulators for projecting arbitrary potential landscapes with single site resolution. We describe use of digital micro-mirror devices as spatial light modulators in two different configurations.

- Chapter 6 shows an example of engineering dynamics in our quantum simulator. We induce photon assisted tunneling in a tilted Mott insulator using lattice amplitude modulation. The tunneling resonances and the multi-orbital shifts of these resonances are measured. We show that the induced coherent dynamics can be used to drive quantum phase transitions between a paramagnet and an

anti-ferromagnet, and to observe quench dynamics when the system is tuned to the critical point.

- Chapter 7 describes experiments to manipulate and detect atoms in a bilayer system. By tunnel couple two adjacent planes, we observe controlled coherent dynamics of a bilayer quantum gas. We develop methods to image both planes with single site resolution, which enabled imaging without the parity-projection. This allows us to obtain the images of the Mott insulator "wedding cake" structure and observe the formation of doublon-hole pairs across a magnetic quantum phase transition. We also demonstrate spin-resolved imaging using the bilayer system.

- Chapter 8 gives a summary of the work in this thesis.

Chapter 2

Theory of ultracold bosons in optical lattices

2.1 Optical dipole potential and optical lattices

Optical forces play a crucial role in the cooling, trapping and manipulating of neutral atoms [21]. Atoms can interact with the light field with both conservative and dissipative forces. The dissipative scattering force results from the absorption of photons that excites the atom, followed by irreversible spontaneous emission as the atom decays from the excited state. The atoms gain momentum through the absorption of photons, but the recoil from spontaneous emission is random in direction and averages to zero net momentum change. This dissipative force is the basis of most laser cooling techniques, where near resonant light is used.

On the other hand, the conservative dipole force is created through the interaction of the light field with the light-induced dipole moment of the atom. This causes a shift in the energy of the atom called the ac-Stark shift. When the light frequency is sufficiently far detuned from atomic resonances so that spontaneous emissions are

negligible, the energy shift acts as a conservative potential that's proportional to the light intensity at the position of the atom.

For a two level atom in a monochromatic laser field where the laser detuning is large and the rotating wave approximation can be used, the conservative dipole potential and spontaneous scattering rate are given by:

$$V_{dipole}(\mathbf{r}) \approx \frac{3\pi c^2}{2\omega_0^3}\frac{\Gamma}{\Delta}I(\mathbf{r}) \tag{2.1}$$

$$\Gamma_{sc}(\mathbf{r}) \approx \frac{3\pi c^2}{2\hbar\omega_0^3}\left(\frac{\Gamma}{\Delta}\right)^2 I(\mathbf{r}) = \frac{1}{\hbar}\frac{\Gamma}{\Delta}V_{dipole}(\mathbf{r}) \tag{2.2}$$

where the atomic transition has a frequency of ω_0 with linewidth Γ, and the laser field has a frequency of ω and intensity $I(\mathbf{r})$. The laser detuning is $\Delta = \omega - \omega_0$. The dipole force thus attracts atoms to regions of higher intensities for red-detuned light, and to regions of lower intensities for blue-detuned light. The heating from scattering in the dipole potential can be reduced by going to larger laser detunings and increasing laser intensities to keep the same depth of the potential. By engineering the spacing intensity profile, we can create almost any potential landscapes for the atoms.

In order to study condensed matter physics problems using ultracold atoms, it's natural to place the atoms in a periodic potential much like how electrons in solids are subject to the periodic potential of the nucleus. Using the optical dipole force, such optical lattice potentials can be created with standing waves formed by counter-propagating laser beams [22]. The resulting lattice has a sinusoidal intensity variation with a period of $\lambda/2$ where λ is the wavelength of the light.

Optical lattices in higher dimensions can be created using pairs of laser beams traveling in different directions. The resulting potential will depend on the geometry of the beams and also the polarization and relative phase of the lattice beams [23, 24], and is in general non-separable due to interference between the beams along different

axes. To make a separable optical lattice, such interference patterns can be avoided for beams with orthogonal polarizations between the lattice axes. Alternatively, one can use slightly different laser frequencies between the different lattice directions and the fast changing relative phase time averages to wash out the interference pattern.

2.2 Non-interacting atoms in optical lattices

For non-interacting atoms in a one-dimensional lattice, the Hamiltonian can be written as:

$$H = \frac{\hat{p}^2}{2m} + V(x) \quad \text{with} \quad V(x) = V_{latt}(1 - \cos^2(kx)) \tag{2.3}$$

where k is the wavevector of the light used to create the lattice and m is the mass of the atom.

According to Bloch theorem, the eigenfunctions of this periodic system take the form:

$$\psi_q^{(n)}(x) = e^{iqx/\hbar} \cdot u_q^{(n)}(x) \tag{2.4}$$

where u is a function with the same periodicity as the lattice. The wavefunctions are labeled by the the band index n and the quasi momentum (or crystal momentum) q. The quasi momentum takes the place of the linear momentum in free space, and is defined in the Brillouin zone $-\hbar k \leq q \leq \hbar k$. This reduction of momentum space is due to the periodicity of the Hamiltonian, and can be understood as the result of the perfect Bragg reflection of the wavefunctions at the Brillouin zone boundary. As q is varied, the energy eigenvalues in each band n changes smoothly. In this thesis, we use the convention that the ground band is label by $n = 0$.

This band structure $E_q^{(n)}$ can be obtained by writing the periodic functions V and

u in Fourier series:

$$V(x) = \sum_r V_r e^{i2rkx} \tag{2.5}$$

$$u_q^{(n)}(x) = \sum_s c_s^{(n,q)} e^{i2skx} \tag{2.6}$$

For the potential $V(x)$ in Equation 2.3, only two terms of the Fourier sum are nonzero: $V_{-1} = V_1 = -V_{latt}/4$, ignoring the constant offset. The time independent Schrödinger equation then reads:

$$\sum_l H_{l,l'} \cdot c_l^{(n,q)} = E_q^{(n)} c_l^{(n,q)} \quad \text{with} \quad H_{l,l'} = \begin{cases} (2l + q/\hbar k)^2 E_r & \text{if } |l - l'| = 0 \\ -V_{latt}/4 & \text{if } |l - l'| = 1 \\ 0 & \text{otherwise} \end{cases} \tag{2.7}$$

The recoil energy $E_r = \hbar^2 k^2 / 2m$ is the energy an atom gains when it absorbs (or emits) a photon with wavevector k from the lattice light, and it serves as a convenient unit for the energy scales in the lattice. The secular equation (Eqn. 2.7) can be solved numerically by truncating the sum over l which corresponds to a truncation at the high energy.

Band structure and Bloch wavefunctions

The resulting band structure is plotted in Figure 2.1 for various values of the lattice depth. At zero depth, the band structure is simply the parabolic dispersion of the free particle folded into the Brillouin zone. As the lattice depth increases, band gaps open where the bands touch and becomes bigger while the individual bands become flatter. For deep lattices in the so called tight-binding limit, atoms in the lowest bands see approximately an array of harmonic potentials at the minima of the lattice and the

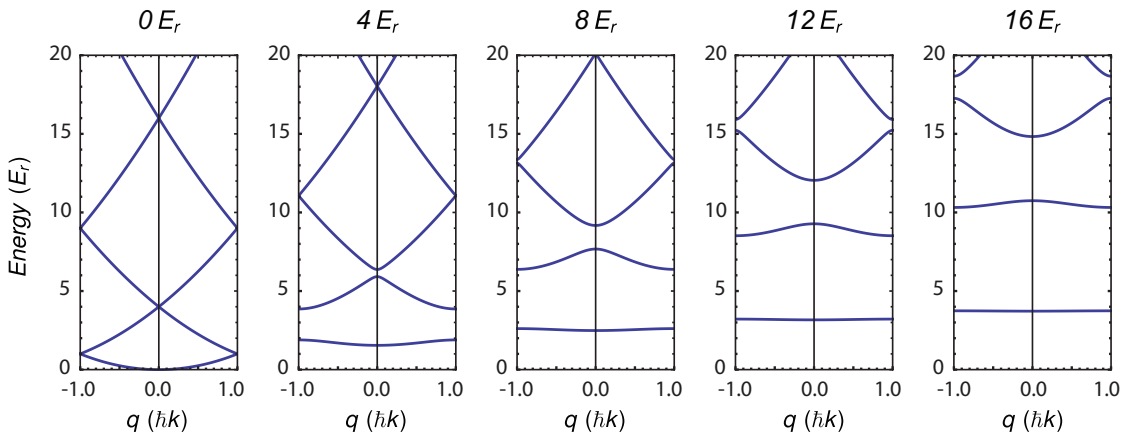

Figure 2.1: Band structure of a one dimensional sinusoidal lattice for different lattice depths, plotted in the first Brillouin zone. Calculated through direct diagonalization of Eqn. 2.7, with l truncated at 6. The constant energy offset in $V(x)$ ignored in Eqn. 2.7 does not effect the dynamics of the system at any given lattice depth, but is added back in the plots to give the proper absolute energy across the different depths.

lowest bands become flat with a spacing equal to the trap frequency ω_{latt} given by:

$$\frac{\hbar\omega_{latt}}{E_r} = \sqrt{4 \cdot \frac{V_{latt}}{Er}} \tag{2.8}$$

The Bloch wavefunctions and the corresponding densities for $q = 0$, $\hbar k/2$ and $\hbar k$ are shown in Figure 2.2. Each Bloch wave can take on an arbitrary additional phase, but only the wavefunctions at the center ($q = 0$) and the edge ($q = \pm\hbar k$) of the Brillouin zone can be made to be purely real.

Wannier wavefunctions

The Bloch wavefunctions (Eqn. 2.4) form a set of complete energy eigenstates for the lattice Hamiltonian (Eqn. 2.3). For any particular band n, they describe atoms with a defined quasi momentum q that are maximally localized in momentum space but completely delocalized in position space. An alternative orthonormal basis for the

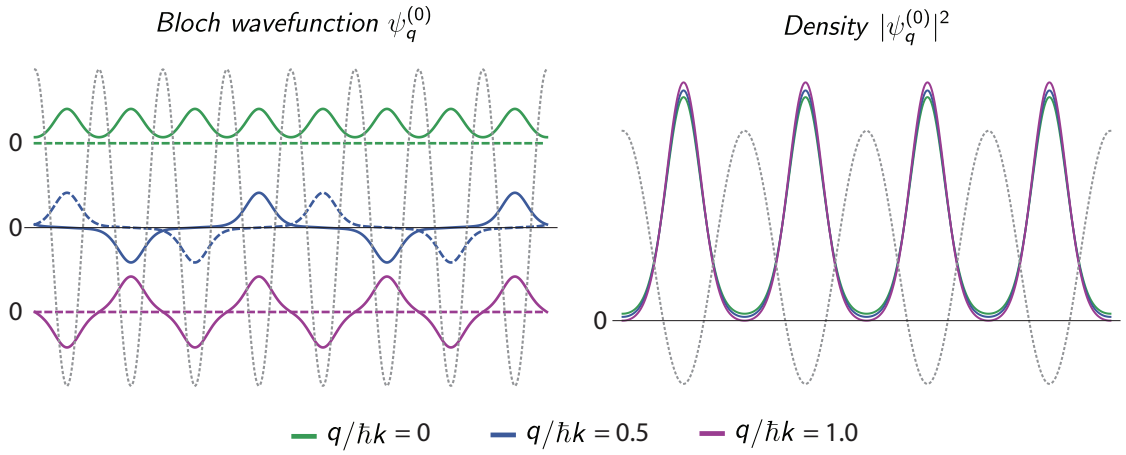

Figure 2.2: The ground band Bloch wavefunctions $\psi_q^{(0)}(x)$ of an $8E_r$ lattice, with quasi momentum $q = 0$, $\hbar k/2$ and $\hbar k$. *Left:* The real part (solid line) and imaginary part (dotted line) of the Bloch wavefunction; *Right:* the probability density. The lattice potential is shown in gray with arbitrary vertical scale.

system is the set of Wannier functions that describe atoms localized in position space at each lattice site x_i. They are a convenient basis for describing lattice systems in the atomic limit and can be constructed as a superposition of all Bloch wavefunctions in the Brillouin zone:

$$\omega_n(x - x_i) = \mathcal{N}^{-1/2} \sum_q e^{-iqx_i/\hbar} \psi_q^{(n)}(x) \tag{2.9}$$

Here $\mathcal{N}$ is a normalization factor. However this definition is insufficient to construct the Wannier wavefunctions. Given the set of Bloch wavefunctions obtained via the direct diagonalization of Equation 2.7 or otherwise, the Bloch function at each q can still take an arbitrary overall phase. The phases need to be set correctly to produce the proper Wannier wavefunction that is maximally localized on site i.

For the case of a one-dimensional lattice, we could follow a simple recipe for choosing the complex phases [25]. Consider the Wannier wavefunction $\omega_n(x - x_i)$ at site i. From the symmetry of the potential, we know the Wannier functions in even bands (ground

band $n = 0$, second excited band $n = 2$, etc.) are symmetric with respect to $x = x_i$, while those in odd bands are anti-symmetric. In addition, the Bloch wavefunctions that make up the Wannier functions in Equation 2.9 also have the same symmetry. To create a wavefunction maximally localized at x_i, we want all the Bloch wavefunctions on the right hand side of Equation 2.9 to add constructively at $x = x_i$: For even bands, we pick the phase of the Bloch wavefunctions such that the amplitude of the Bloch wavefunctions at $x - x_i$ is real and positive. For odd bands, the constituent Bloch wavefunctions always have zero amplitude at $x = x_i$, and we pick the phase such that the derivative of the Bloch wavefunctions at $x = x_i$ is real and positive.

Mathematically, we define the properly phase adjusted Bloch wavefunctions as:

$$\psi_q^{(n)}(x) \to \begin{cases} \psi_q^{(n)}(x) \cdot \mathrm{Exp}\left(-i\ \mathrm{Arg}\left[\psi_q^{(n)}(x_i)\right]\right) & n \text{ even} \\ \psi_q^{(n)}(x) \cdot \mathrm{Exp}\left(-i\ \mathrm{Arg}\left[d\psi_q^{(n)}(x)/dx\big|_{x=x_i}\right]\right) & n \text{ odd} \end{cases} \tag{2.10}$$

Then using Equation 2.9 to calculate the proper Wannier functions as the maximally localized states possible. For even bands, the wavefunction has the highest amplitude at $x = x_i$; for odd bands, the wavefunction has the sharpest slope. In both cases, far away from x_i, the Bloch wavefunctions have varying phases and amplitude and the sum destructively interfere to give vanishing amplitude of the Wannier function. It can be verified that the Wannier functions constructed using the current procedure are purely real.

Figure 2.3 (a) shows the Wannier functions of the lowest four bands in an $8E_r$ deep lattice. While the ground state has population mostly confined in the single site of the potential, the higher bands quickly start to have significant population into the neighboring sites. In Figure 2.3 (b), the ground state Wannier function for three different lattice depths are plotted. For increasing lattice depth, the Wannier function gets narrower with smaller amplitudes that extend into the neighboring sites. In deep

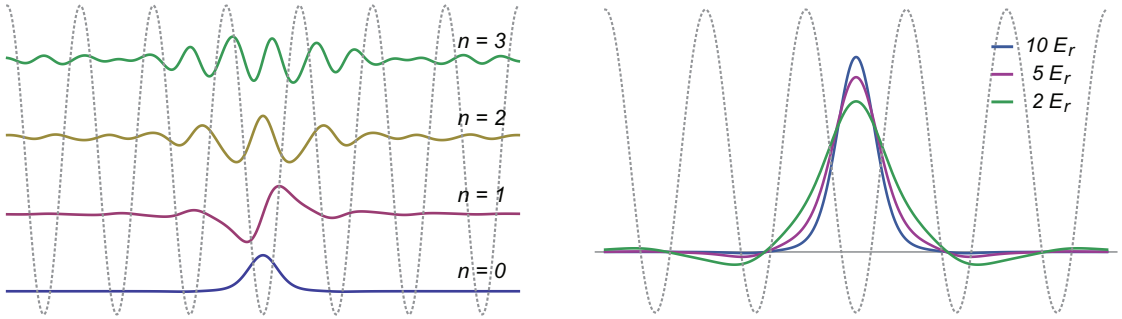

Figure 2.3: **(a)** The 4 lowest band Wannier wavefunctions $\omega_n(x)$ of an $8E_r$ lattice, showing alternating even and odd parities. **(b)** The ground band Wannier functions for lattice depths 2, 5 and $10E_r$. The wavefunction gets more localized with increasing lattice depth. The lattice potential is shown in gray with arbitrary vertical scale.

lattices, the Wannier functions get closer to the harmonic oscillator wavefunctions. But due to the finiteness of the lattice (as opposed to the infinite harmonic potential), there always exists non-negligible amplitude in the wings of the Wannier functions that are crucial for an accurate description of the system.

2.3 The Bose Hubbard model

Atom-atom interaction

The unique advantage in experiments with ultracold atoms is the precise control of the effective atom-atom interaction. Using magnetic Feshbach resonances [12], the sign of the interaction can be changed between being attractive or repulsive, the interaction can be effectively turned off or turned to the strongly interacting unitary limit. In optical lattice experiments, the interaction energy scales are determined by the depth of the lattice, which can be varied over a few orders of magnitude simply by changing the laser power used to create the lattices.

The interaction between two atoms in dilute gases can be described as an inter-

atomic potential $V(\mathbf{r})$, where $\mathbf{r}$ is the inter-particle distance. Qualitatively, the potential is strongly repulsive at short distances (on the order of a few Bohr radii a_0) due to the Coulomb interaction of the atoms' electron cloud. At long distances, the interaction is approximately given by the attractive van der Walls force arising from the mutually induced electric dipole-dipole interaction $\propto -C_6/r^6$ [26].

At the temperatures of ultracold atom experiments, atoms interact primarily through elastic scattering. Although the exact shape of the inter-atomic potentials are hard to determine, such details are not necessary for describing the scattering properties at low energies because the atoms do not have sufficient kinetic energy to overcome the centrifugal barrier and only the lowest partial wave scattering process contributes. Thus for bosons at the low energy limit, only s-wave scattering takes place and the inter-atomic interaction can be well approximated by a short-range contact interaction characterized by a single parameter, the s-wave scattering length a_s. Take the simplest form of a delta function for the contact potential, we have:

$$V(\mathbf{r}) = \frac{4\pi\hbar^2 a_s}{m}\ \delta(\mathbf{r}) \tag{2.11}$$

For ^{87}Rb the s-wave scattering lengths in both the $F = 1$ and $F = 2$ ground states are almost identical, at $a_s \approx 100\ a_0 \sim 5$ nm [27].

Interacting bosons in optical lattices

We start by writing the Hamiltonian for bosons in a trapping potential $V(x)$, interacting with the contact interaction in Equation 2.11:

$$\begin{aligned} H = &\int d^3x\ \hat{\Psi}^\dagger(x)\left(-\frac{\hbar^2}{2m}\nabla^2 + V(x)\right)\hat{\Psi}(x) \\ &+ \frac{1}{2}\frac{4\pi\hbar^2 a_s}{m}\int d^3x\ \hat{\Psi}^\dagger(x)\hat{\Psi}^\dagger(x)\hat{\Psi}(x)\hat{\Psi}(x) \end{aligned} \tag{2.12}$$

Here $\hat{\Psi}$ is the bosonic field operator, and $V(x) = V_{latt}(x) + V_{ext}(x)$ contains both the lattice potential V_{latt} and any slowly varying external potential V_{ext}, for example confinement from a harmonic trap. It is convenient to use the Wannier wavefunctions as the basis for the Hamiltonian. If the dynamics of the atoms have energy scales much smaller than the band spacing of the optical lattice, excitations to higher bands are negligible. This is the case for ultracold atoms cooled to the sub-micro-Kelvin to nano-Kelvin regime and loaded in conservative lattices with depths in the tens of kHz range. We can then expand the field operator in terms of the ground band Wannier functions:

$$\hat{\Psi}(x) = \sum_i \hat{a}_i \; \omega_0(x - x_i) \tag{2.13}$$

Here $\hat{a}_i$ and $\hat{a}_i^\dagger$ are the annihilation and creation operators for a boson on the lattice site at x_i. They follow the bosonic commutation relations $[\hat{a}_i,\hat{a}_j^\dagger] = \delta_{ij}$. Equation 2.12 can then be written as:

$$H = -\sum_{i,j} J_{ij} \; \hat{a}_i^\dagger \hat{a}_j + \sum_{i,j,k,l} \frac{U_{ijkl}}{2} \; \hat{a}_i^\dagger \hat{a}_j^\dagger \hat{a}_k \hat{a}_l + \sum_i (\epsilon_i - \mu)\hat{n}_i \tag{2.14}$$

where the on-site occupation operator is $\hat{n}_i = \hat{a}_i^\dagger \hat{a}_i$. The external potential on each site is $\epsilon_i = V_{ext}(x_i)$ and μ is the chemical potential that can be viewed as the constraint for total particle number in the grand canonical ensemble description. J_{ij} are the tunneling matrix elements that describe tunneling between any two sites i and j. U_{ijkl} give the various interaction induced terms. For example U_{0000} is the on-site interaction, while U_{1010} is the nearest neighbor interaction. From the Wannier functions, we can calculate:

$$\begin{aligned} J_{ij} &= -\int \omega_0^*(x - x_i) \left(-\frac{\hbar^2}{2m}\nabla^2 + V_{latt}(x) \right) \omega_0(x - x_j) \; d^3x \\ U_{ijkl} &= \frac{4\pi\hbar^2 a_s}{m} \int \omega_0^*(x - x_i)\omega_0^*(x - x_j)\omega_0(x - x_k)\omega_0(x - x_l) \; d^3x \end{aligned} \tag{2.15}$$

The tunneling matrix elements can also be obtained directly from the band structure. Intuitively, tunneling of the Wannier functions can be seen as a result of the interference between the constituent Bloch wavefunctions: For example, nearest neighbor tunneling is to a good approximation the interference between $\psi^{(0)}_{q=0}$ and $\psi^{(0)}_{q=\hbar k}$ in Figure 2.3(a), which happens as a rate of $(E^{(0)}_{q=\hbar k} - E^{(0)}_{q=0})/4$.

Formally, using Equation 2.9 in the expression of J in Equation 2.15, the mth neighbor tunneling in the nth band $J^{(n)}_{0m}$ is given by the amplitude of the Fourier transform of the nth band dispersion $E^{(n)}_q$ that corresponds to a period of $2\hbar k/m$ in the momentum q space:

$$J^{(n)}_{0m} = -\sum_q E^{(n)}_q e^{-iqm\pi/\hbar k} \tag{2.16}$$

Tight binding approximation

In addition to the single band (i.e. ground band) approximation applied above, we take the tight-binding approximation valid for deep lattice depths. In this limit, the Wannier wavefunctions are sufficiently localized so that all higher order tunneling processes and higher order interaction terms can by ignored. Keeping only the nearest neighbor tunneling $J \equiv J_{01}$ and the on-site interaction $U \equiv U_{0000}$, Equation 2.14 results in the celebrated Bose Hubbard Hamiltonian:

$$H_{BH} = -J\sum_{\langle i,j\rangle} \hat{a}^\dagger_i \hat{a}_j + \sum_i \frac{U}{2}\hat{n}_i(\hat{n}_i - 1) + \sum_i (\epsilon_i - \mu)\hat{n}_i \tag{2.17}$$

In the tight binding limit, the dependence of J and U on lattice depth V_{latt} can be qualitatively described by approximating the Wannier functions with Gaussian ground state wavefunction for the Harmonic oscillator. J is closely related to the amplitude in the tails of the wavefunction, and it drops exponentially with increasing V_{latt}. U on the other hand increases only slightly at higher depths due to the narrower spatial spread of the wavefunction, with a $(V_{latt})^{1/4}$ dependence in each spacing dimension. Hence the

ratio J/U can be varies over a wide range by tuning the lattice depth.

The values of J and U calculated from the Wannier wavefunctions are plotted in Figure 2.4, using parameters in our experiment with ^{87}Rb . The recoil energy for the 680 nm spacing two-dimensional square lattice is $2\pi \times 1240$ Hz. The interaction U is calculated for equal lattice depth in both directions in the plane, and an out-of-plane trap frequency of 6 kHz. The scattering length is determined experimentally. Figure 2.5 shows the ratio between interaction and tunneling.

2.4 The superfluid to Mott-insulator transition

The Bose Hubbard Hamiltonian has two distinct quantum phases, and the quantum phase transition between the two phases are driven by quantum fluctuations that persist even at zero temperature. We start by describing the two states in a homogeneous lattice ($\epsilon_i = 0$) before taking into account the effect of external confining potentials.

Small U/J: superfluid phase

In the limiting of weak interactions the kinetic tunneling term dominates. Because of the positive sign of J, atoms in the ground state prefer to delocalize over the whole lattice. For vanishing interaction ($U/J = 0$), all atoms are Bose-condensed in the Bloch state at $q = 0$ and the exact ground state wavefunction is:

$$|\Psi_{SF}\rangle = \left(\hat{a}^\dagger_{k=0}\right)^N |0\rangle \propto \left(\sum_i \hat{a}^\dagger_i\right)^N |0\rangle \tag{2.18}$$

where $|0\rangle$ is the vacuum. This superfluid state can be viewed as an array of tiny Bose-Einstein condensates at all lattice sites, whose phases are locked together over the whole lattice by the tunneling. The phase $\hat{\phi}_i$ and atom number $\hat{n}_i$ on each lattice site are conjugate variables. Therefore the well-defined phase of the superfluid state

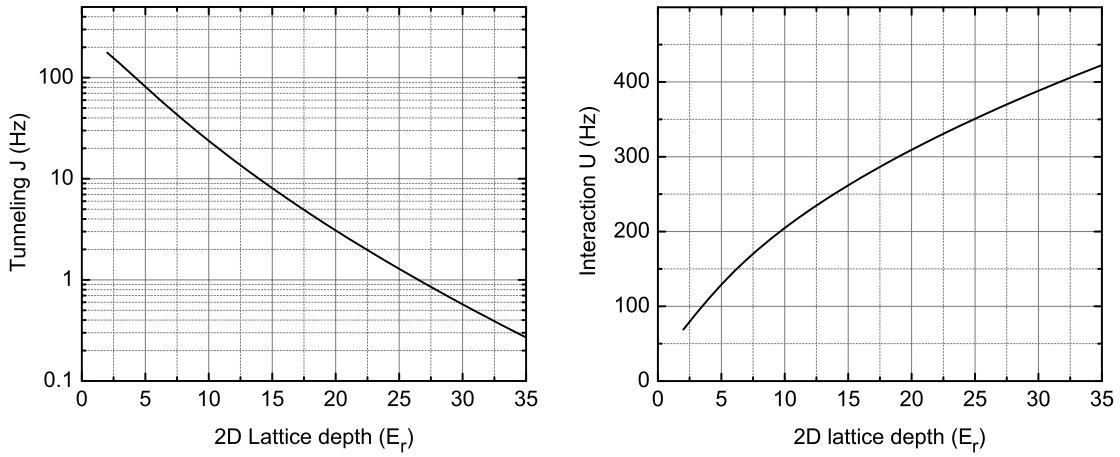

Figure 2.4: Tunneling and interaction in the Bose Hubbard model, calculated for our 2D lattice. Qualitatively, the tunneling rate approximately decreases exponentially with increasing lattice depths; while the interaction has a square root dependence on lattice depth in the 2D case.

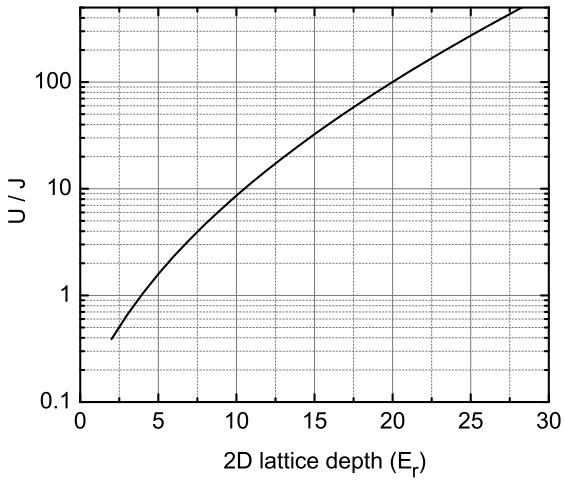

Figure 2.5: The ratio between interaction and tunneling, from values plotted in Fig. 2.4.

implies that the particle number fluctuates on each lattice site, which is apparent from the right hand side of Equation 2.18. For a given average atom density $\bar{n}$, the local atom number distribution $P(n)$ follows a binomial distribution:

$$P(n) = \frac{1}{n!}\, e^{-\bar{n}}\ (\bar{n})^n \tag{2.19}$$

The superfluid phase is characterized by: (a) Non-zero value of the order parameter $\psi \equiv \langle a_i \rangle$, (b) no finite gap between the ground state and the excited states and (c) finite compressibility $\kappa = \partial n/\partial \mu$ – as the chemical potential increases, $\bar{n}$ also increases continuously, as seen from Equation 2.19.

Large U/J: Mott insulating phase

When the interaction dominates over the tunneling, the ground state of the system is an insulating phase. In the limit $J \to 0$, the kinetic term vanished and the remaining terms in the Hamiltonian (U and μ) are both local on each site and commutes with the on-site occupation $\hat{n}$. So for a given chemical potential μ in a homogeneous lattice, the atom number on each site is fixed and constant over the lattice. The on-site occupancy is obtained by minimizing the energy on the lattice site as $n = \lceil \mu/U \rceil$. The Mott insulator wavefunction with n atoms per site is:

$$|\Psi_{MI}\rangle = \prod_i \left(\hat{a}_i^\dagger\right)^n |0\rangle \tag{2.20}$$

In the Mott insulator, the phase coherence between different lattice sites is lost, and the order parameter ψ is zero. The elementary excitation in the Mott insulator is hopping of one atom from one site to its neighbor, at a energy cost of U. Since the atom number per site n takes a step like function with increasing chemical potential μ, the Mott insulator is incompressible.

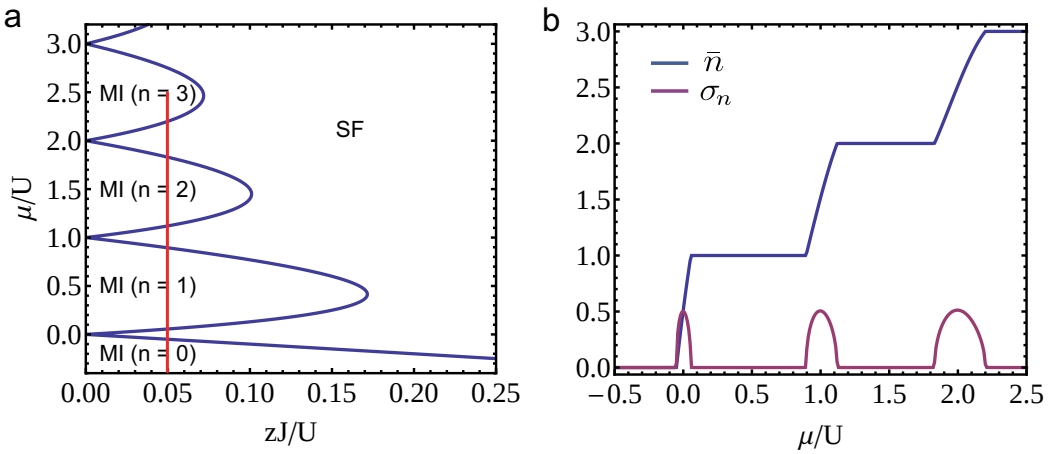

Figure 2.6: (a) Mean field phase diagram of the Bose-Hubbard model, showing the Mott insulator lobes surrounded by the superfluid region. The lobes get smaller with increasing atom number as a result of stronger quantum fluctuations due to Bosonic enhancement of tunneling. (b) The mean atom number and variance at $zJ/U = 0.05$, as the chemical potential is varies, corresponding to the red line in (a). The density shows the famous wedding cake structure.

Mean-field phase diagram

The phase diagram of the Bose Hubbard model can be understood from a mean field approach, and the transition between the superfluid and Mott insulator is a second order transition that can be described by a simple Laudau theory [28].

The μ/U–zJ/U mean field phase diagram is plotted in Figure 2.6(a), showing the Mott insulator lobes with different occupation numbers and the superfluid region. z is the coordination number, i.e. the number of nearest neighbors for each lattice site.

We start from a point inside a Mott insulator lobe with $n = n_0$. At constant chemical potential, slight change in J/U does not affect the state because it takes a finite energy U in order to change the particle number on any site. As J/U increases, the energy gap gets smaller while the tunneling gets stronger. Eventually at the phase boundary, the reduction in energy from the kinetic term overcomes the energy gap from

interaction, and the Mott insulating state is destroyed. The Mott insulator lobes shrink with increasing n_0 due to stronger quantum fluctuations from bosonic enhancement.

It's worth noting that in a homogeneous lattice with constant μ (therefore constant atom number), the Mott insulator can only be reached from the superfluid by reducing J/U if the total atom number is an integer multiple of the number of sites. Otherwise there will always be some atoms delocalized on top of a Mott insulator, and the overall state is a superfluid.

At a fixed value of J/U, if the chemical potential is varied, the many-body state goes through the Mott lobes with different n, separated by superfluid regions. This is indicated by the red line in Figure 2.6(a). The mean atom number per site $\bar{n}$ and the variance of atom number $\sigma_n = \sqrt{\bar{n^2} - (\bar{n})^2}$ along the red line is plotted in Figure 2.6(a). The curves are calculated with a Gutzwiller variational wavefunction [29] truncated to only states with $n = n_0, n_0 \pm 1$, which is a valid approximation for the strongly interacting limit. Such a spatially varying chemical potential can be realized for atoms confined in a harmonic trap where the chemical potential increases from the trap center, leading to the well-celebrated "wedding cake" shell structure which has been experimentally observed [30, 31].

Chapter 3

Quantum gas microscope: a recap

Experiments described in this thesis are carried out in our quantum gas microscope, where an ultracold quantum gas of bosonic Rubidium 87 atoms are loaded into a two dimensional square optical lattice at the focus of a high resolution imaging system with single site resolution (Fig. 3.1). In this chapter we give an overview of the apparatus and describe the experimental procedures for preparation, manipulation and detection of the ultracold gases. A number of experiments in this thesis are based on extensions to what is described in this chapter. Further details on the apparatus can be found in previous theses [32, 33, 34].

3.1 Creating the Bose-Einstein condensate

Each experimental run starts with ^{87}Rb atoms loaded into a magneto-optical trap, where we gather about 10^9 atoms at a temperature of $\sim 40\,\mu$K after cooling in an optical molasses. The atoms are polarized into the $|F = 1, m_F = -1\rangle$ state, and transported magnetically [35] into the ultra-high vacuum science glass cell. The forced RF evaporation is performed in an oblate QUIC trap [36] to produce a 3D Bose-Einstein

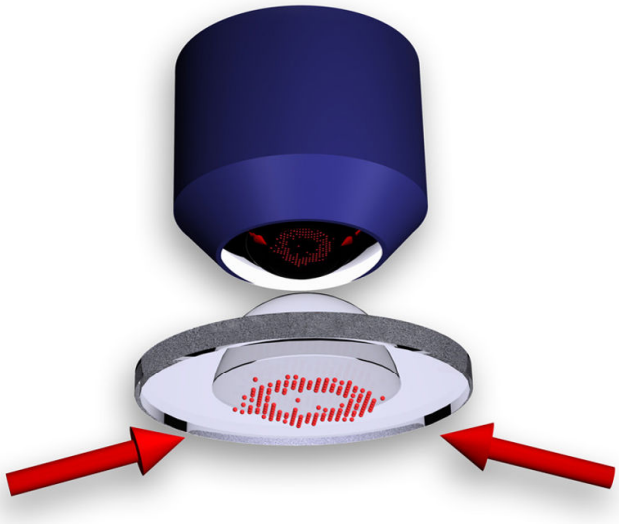

Figure 3.1: A conceptual illustration of the quantum gas microscope. A 2D quantum degenerate gas of ^{87}Rb atoms trapped about 10 μm away from the surface of the last lens of a high numerical aperture imaging system. This last lens consists of the glass hemisphere optically contacted to a super-polished glass substrate.

condensate with about 5×10^4 atoms.

3.2 Loading the condensate into the two dimensional plane

The high numerical aperture imaging system we use gives us diffraction limited performance with a resolution close to the wavelength of the fluorescence light. This implies also a very short depth of focus for the imaging system and atoms $\sim 1\,\mu$m away or more would already be out of focus and contribute only to a washed out background patch of fluorescence. We thus work primarily with a single 2D layer of atom in our experiments.

To study physics in 2D systems, the Bose-Einstein condensate needs to be loaded into a tightly confining 2D planar trap where the motion in the direction perpendicular to the plane is completely frozen out. Further more, tighter confinement leads to stronger interactions which is favorable for reaching the strongly correlated regime.

We use a two stage standing wave setup to prepare the single atomic layer. Both standing waves are created by reflecting blue-detuned far off-resonant laser beams off of the surface of the super-polished substrate, at shallow angles. The spacings of the standing waves are determined by the incident angles of the beams.

The condensate is first moved to $\sim 10\mu m$ below the surface of the substrate surface and loaded into the first anti-node of the standing wave with a period of $\approx 9.2\mu$m, which we call the "big lattice". The big lattice has an incident angle of $\approx 75°$ from below, which can be tuned slightly.

Next a second vertical standing wave with a 1.5μm lattice spacing is ramped on that we call the "axial lattice". It has an incident angle of 87.6°. The atoms in the big lattice will now sit at the sixth anti-node plane of the axial lattice. The big lattice

is then turned off, and the 2D physics is carried out in the axial lattice. The depths of the big and axial lattices are ramped smoothly to make sure that the loading and transfer are adiabatic and all atoms remain in the ground state in the vertical direction (also referred to as the axial direction). In addition, the condensate is aligned to the big lattice plane by varying the vertical position of the magnetic trap minimum with a small offset field. The big lattice plane and the axial lattice plane are aligned by slightly varying the spacing of the big lattice and look at the loading efficiency.

By placing the anti-node of the big lattice carefully with respect to the axial anti-nodes, it is possible to load atoms into a neighboring axial plane or even deliberately load two adjacent planes simultaneously. This is utilized in Chapter 7 for creating bilayer quantum gases.

The incident beams for both the big lattice and the axial lattice are elliptically shaped so that in the plane of the atoms they have relatively circular intensity profiles. They are far blue-detuned with a wavelength of 755 nm and a spectral width of 3 nm. The incident beams are s-polarized which ensures proper interference and leads to the resulting standing waves having an anti-node at the substrate surface.

3.3 High resolution imaging system and lattice projection

The 2D quantum gas is at the focus of the high resolution imaging system, as illustrated in Figure 3.2. A long working distance microscope objective with a numerical aperture of NA = 0.55 sits outside of the vacuum glass cell. A glass hemisphere is inside the glass cell and is optically contacted to the super-polished substrate under which the atoms are located. The hemisphere acts as a final lens for the objective. Refraction at the substrate surface causes a "solid immersion" effect that boosts the effective NA of the

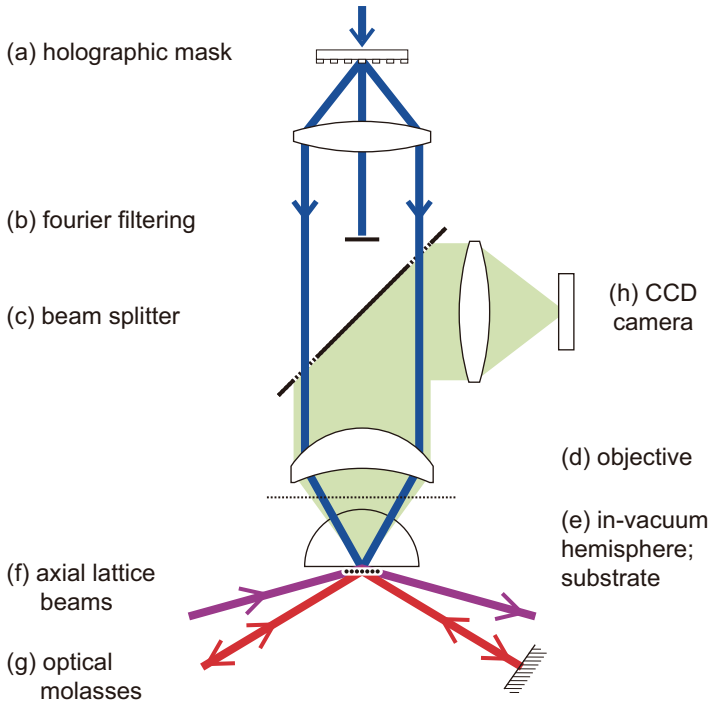

Figure 3.2: Illustration of lattice projection and imaging in the quantum gas microscope.

imaging system by a factor of the refractive index of the glass to NA = 0.8, resulting in a diffraction limited resolution of $\approx 600\,\mathrm{nm}$ at the design wavelength of 780 nm.

Instead of using interfering counter-propagating laser beams as in most optical lattice experiments, the 2D lattice in our apparatus is created by direct projection of holographic masks onto the atoms through the objective. The lithographically manufactured holograms act as phase gratings whose geometry determines the structure of the projected lattice. For the current square lattice we use, two orthogonal 1D holograms each produces the lattice in one direction. With the projection scheme the lattice spacing is set by the spacing of the grating on the hologram and is independent of the wavelength used. This allows us to use broadband light for the physics lattice, or to significantly change the lattice depth at similar lattice powers by switching the wavelength between far-detuned and near-resonant. A more detailed description of the optical lattice setup is found in Section 4.3.

Most of our experiments works with less than a few hundred atoms in regions of tens of lattice sites across. With the condensate trapped in the axial lattice, a tightly focused red detuned "dimple" beam is adiabatically turned on at the center cloud to collect a small number of atoms. The atom number is controlled precisely by the final depth of the dimple potential. The rest of the atoms are expelled by turning off the magnetic trap that has been providing the radial confinement. The dimple potential also has the advantage of selecting only the coldest atoms at the center of the initial cloud. The atoms in the dimple are then adiabatically released into a harmonic dipole trap, created by either a red-detuned Gaussian beam or a blue-detuned doughnut (Laguerre–Gaussian) beam. Both the dimple and dipole potentials are projected through the objective.

The conservative 2D lattice is then turned on adiabatically. The far detuned lattice has the same wavelength as the axial lattice at 755 nm with a spectral width of 3 nm,

and is referred to as the "physics lattice" since the coherent quantum evolution we want to study happens here. The lattice spacing is $a = 680\,\text{nm}$, which gives a recoil energy of $E_r = 2\pi \times 1240\,\text{Hz}$.

Many of the experiments discussed in this thesis start with Mott insulators in a deep physics lattice. Starting with atoms in the harmonic trap, the 2D lattice is ramped up in about 400 ms to $45\,E_r$ in both directions to drive a transition from the superfluid to the Mott insulator state. The widths of the Mott insulator shells and the atom number can be varied by the dimple depth, and frequency of the harmonic trap typically in the range of $40-60$ Hz. We can prepare Mott insulator regions of different occupancies with a high fidelity of $> 99\%$ [18].

For imaging the atoms at the end of the experiments, the 2D lattice depth is increased rapidly to $\sim 5000\ E_r$ to project the many-body state onto the space of local Fock states on each site. This is done by switching the wavelength of the lattice to $\sim 30\,\text{GHz}$ blue detuned to the ^{87}Rb D1 line at 795 nm, and this deep lattice is referred to as the "pinning lattice" in which tunneling is turned off and the atoms are pinned to each lattice site. An axial pinning lattice derived from the same light source is used to increase the lattice depth in the axial direction at the same time.

Heating of atoms in lattice potentials occurs when atoms off-resonantly scatter the lattice photons and either fall back to the ground band (ground-band scattering) or to an excited band (inter-band scattering) [37, 38]. The former causes decoherence of the wavefunction, and is suppressed in a blue detuned lattice where atoms sit near the intensity minima. The inter-band heating rate however is identical in deep lattices of red or blue detuning [38].

3.4 Fluorescence imaging

We collect fluorescence photons from the atoms to form the high resolution images. While the atoms are being trapped in the deep pinning lattice, we illuminate the cloud with near-resonant optical molasses beams to perform in lattice sub-Doppler cooling. The molasses beams are red-detuned 80 MHz to the $F = 2$ to $F' = 3$ transition of the D2 line near 780nm. Light on the D2 $F = 1$ to $F' = 2$ transition is also added for repumping.

The molasses setup consists of two beams each along one axis of the 2D lattice. The first one travels along x and illuminates the substrate surface at an angle of 8° from the surface with s-polarization. The reflected beam is retro-reflected with orthogonal polarization (p-polarized) and travels through the same path, as shown in Figure 3.3. This creates periodic variations in both the intensity and polarization along x and along the vertical direction. The polarization gradient leads to Sisyphus cooling in the $lin \perp lin$ configuration [39, 40]. The second molasses beam enters along y in a similar configuration to provide the polarization gradient and hence cooling along y. The frequency of the two molasses beams are offset by 7 kHz so that their mutual interference pattern averages out in time. In addition, the retro-reflector for the x molasses is shaken normal to the beam at 100 Hz to move its intensity/polarization pattern by more than one period along x. Both the frequency offset and the spatial shaking help ensure that all lattice sites in the 2D plane experience a uniform time-averaged cooling and fluorescence rates.

In Section 7.2.1 we will take another look at the molasses configuration and make use of their intensity gradient in the axial direction to image two adjacent plane of atoms.

The photons scattered by the atoms during the polarization cooling is collected by

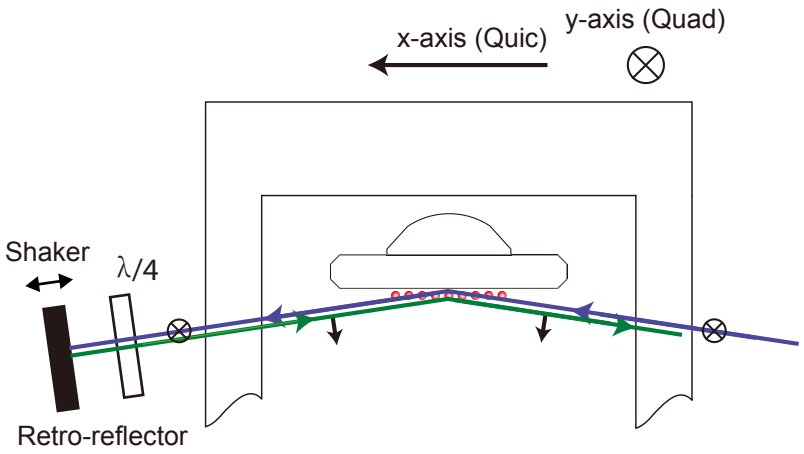

Figure 3.3: The geometry of the molasses beam along x-axis of the 2D lattice. The beam is incident from the right with s-polarization and is reflected at the substrate surface. The polarization is then rotated by 90° with a quarter waveplate and retro-reflected along the same path. The two counter-propagation beams produce Sisyphus cooling in the $lin \perp lin$ configuration. The retro-reflecting mirror is mounted on a piezo mount that allows it to be shifted along the beam direction. See also [34].

the imaging system and recorded on an EMCCD camera (Andor Ixon). During the typical exposure time of 500 ms, about 2000 photons per atom are collected on the camera, which is about 10% of all photons scattered. The lattice projection path and imaging path are combined with a non-polarizing beam splitter above the objective.

For atoms strongly confined to the same site of a deep lattice, illumination of near-resonant light leads to light-assisted collisions that excite pairs of atoms to molecular states [41, 42]. For red-detuned light, the pair of atoms are excited to the attractive molecular potential and accelerated towards smaller inter-atomic distance. In this process, the atoms can gain enough momentum to escape the lattice, via either a transition to a more deeply bound molecular state or the radiation of a red-shifted photon. In our pinning lattice, atom pairs undergo light-assisted collisions and leave the trap on a time scale of a few hundred μs, long before they can scatter enough photons. Therefore we are only sensitive to the parity of the on-site occupation number: Sites originally with even number of atoms will have zero atoms left so they appear dark, while sites with odd number of atoms will have one atom left and appear bright. Such "parity imaging" is present in all experiments using fluorescence imaging in a deep lattice [43, 18, 16].

The obtained fluorescence images are analyzed by fitting the amplitude of the point spread function on each site. The point spread function of the imaging system and the lattice structure are separately determined from images with sparsely populated atoms. The fitted amplitudes have a clear bimodal distribution, which allows us to determine the presence or absence of an atom on each site with high fidelity.

The experiment is repeated many times to give the average atomic density or expectation value of any other observables.

Chapter 4

Reducing uncontrolled disorder with incoherent light sources

The effectiveness of quantum simulation using ultracold atoms depends critically on the ability to engineer potential landscapes with high precision.

To study critical phenomena near quantum critical points, for example, the potential is often required to be homogeneous over a large scale. Otherwise the system will simply fragment into separated regions that transition independently, which hinders the ability to create entanglement over large number of sites and thus complex many-body strongly correlated states.

Experimentally, laser beams with large Gaussian profiles should produce near homogeneous potentials over the small region near the center. Alternatively the superposition of beams with different spatial profiles or special purpose spatial light modulators can be used to give near flat or other forms of smooth optical potentials. Unfortunately, even though the light potentials we intend to project have well defined profiles (e.g. a perfectly clean lattice, or a perfect Gaussian potential), aberrations and scattering from imperfections in the imaging system all contribute to uncontrolled

corrugations and defects in the potentials the atoms experience. In this chapter, we seek methods to create smooth precise potentials despite the unavoidable imperfections of the optical system, and to measure and characterize any remaining disorder. Such knowledge is crucial for calibrating other parameters of the system, or benchmarking the quantum simulator's performance.

Disordered potential is interesting in its own right, leading to e.g. Anderson localization [44] or Bose glass phases [45], and many open questions remain in the interplay between strong disorder and strong interactions [46]. Once we have the ability to make very clean potentials, disorder or impurities can be introduced in a controlled way.

For coherent light, disorders appear when the otherwise clean beam interferes with even trace amount of stray reflection or scattering. As an illustrative example of the heterodyning effect of interference, we consider an incoming coherent light field that is scattered by imperfections in the media. For a scattered intensity of one part in ten thousand $I_{sc} = 10^{-4} I_0$, the scattered field amplitude is $E_{sc} = \pm 10^{-2} E_0$. The resulting intensity from the interference of the two is $I \propto |E_0 + E_{sc}|^2 \approx I_0 \left(1 \pm 2E_{sc}/E_0\right)$, corresponding to a 4% peak to peak variation in light intensity thus in the dipole potential the atoms see. In contrast, if the scattered field is incoherent with the incoming field, the two would only add in intensity, leading to a much smaller 0.01% variation. Therefore we expect the use of incoherent sources to greatly reduce uncontrolled disorder in the projected optical potentials.

4.1 Disorder in optical lattice potentials

For the lattice potentials, the two primary effects of disorder and inhomogeneities are variations in the energy offset, and/or variations in the lattice depth on different lattice sites.

Consider the Hubbard model, energy offsets correspond to changes in the local chemical potential. Variations that are relatively small ($\leq \min(J, U)$) and smooth (over a few sites or slower) can usually be described by some local field in a similar fashion to the local density approximation. If the variation in offset are bigger than the characteristic energy scales (U and J) and have sharp spatial features, it can freeze dynamics on the affected lattice sites – atoms on these sites are effectively "stuck" due to the big energy offset and appear as static impurities in the lattice. On the other hand, disorder in the lattice depth causes variations in J, U, as well as in the offset via the zero point energy given by $\hbar\omega/2$.

As an order of magnitude estimation, let's take a typical $10E_r$ physics lattice. The lattice depth in our case is about $V_{latt} \sim 4E^2 \approx 10\,\text{kHz}$, the trap frequency $\omega_{latt} \approx 7\,\text{kHz}$. Tunneling $J \approx 20\,\text{Hz}$ and interaction $U \approx 200\,\text{Hz}$. Assuming in a small region of the lattice there is now one percent variation in the field amplitude of one of two beams $\delta E = 1\% \times E$, so $\delta I = 2\% \times I$. This leads to changes in:

- Offset – The potential cause by the light intensity near the bottom of the lattice sites $\epsilon \sim (\delta E)^2 \approx 0.25\,\text{Hz}$.

- Zero point energy – The local interference contrast (and thus the lattice depth) is varied by $\delta E/E$. The trap frequency varies by $\delta\omega/\omega \sim (1 - \sqrt{1 - \delta E/E})$ and the zero point energy changes by $\epsilon \approx 17\,\text{Hz}$.

- J – Scales approximately exponentially with trap frequency, $J \propto \exp(-2\omega_{latt}/E_r)$. So tunneling changes by $\delta J \approx 0.06J \approx 1Hz$.

- U – Consider two dimensional case, in which $U \sim (\sqrt[4]{V})^2$. Thus $\delta U \approx 1Hz$.

Therefore we see for an optical lattice, the primary effect of disorder in the beam profile is a change in the zero point energy that contributes as a chemical potential term in

the Hamiltonian. To ensure that this resulting disorder in the local chemical potential is smaller than the energy scale of the dynamics J (and U), the intensity disorder on individual beam of the lattice need to be well below the one percent level.

The non-zero offset intensity at the lattice sites for our 2D lattice is further complicated by the chromatic focal shift of our objective, which can cause reduction in the interference contrast when using the broadband light sources described in Section 4.2. For an achromatic optical system, the projection method we use for lattice creation would ensure the spacing and phase of the lattice in the image plane to be constant regardless of the wavelength. However, if the system has a chromatic focal shift, the different wavelength components focus at slightly different planes, and the their phases in the plane of the atoms can vary if the beams are not traveling exactly along the optical axis. The custom objective we currently use has an effective focal length that changes by $\sim 1\,\mu$m per 1 nm change in wavelength. For the 3 nm wide (FWHM) physics lattice, the interference contrast dropped to 97% if the lattice beams are off center by 2% of the aperture diameter in the Fourier plane, and to 80% contrast if off by 5%. The chromatic focal shift also leads to a chromatic shift in magnification that causes lattices at different wavelengths to have slightly different spacings. Its effect on the contrast and geometry of the 3 nm wide physics lattice is negligible over the size we are interested in.

There are also other situations where intensity imbalance in lattice beams causes big energy offsets. Of particular concern in our experiments is the axial lattice (and similarly the big lattice) that provides the vertical confinement. It is created by reflecting light off of the *uncoated* substrate surface at a shallow angle, so the intensity is only partially reflected. This geometry gives rise to gradients in the axial trapping frequency and the offset energy. Furthermore, the location where the trap frequency is maximum (and thus most uniform) does not coincide with where the offset is most uniform.

So for experiments where a uniform trap frequency is desired (e.g. those involving coherent excitation to higher bands), the remaining gradient in offset might have to be compensated by either an additional optical potential or a magnetic field gradient.

4.2 Temporally incoherent light source

To eliminate interference between the lattice light and stray light from reflections at optical surfaces (for example at the various lens surfaces, or the glass cell), we use broadband "white" light with a short coherence length on the order of $1\,\mu$m. The interference needed to produce the lattice structure is still present, because of the projection method used in our quantum gas microscope. The in-plane lattice along each axis is created by illuminating the holographic mask with a single beam, so the two momentum components of the light that interfere to give the lattice travel through exact same optical path lengths (OPL). For the vertical lattices which are reflected at the substrate surface, the OPL difference between the incident and reflected beam is $2d\cos\theta_i$ where d is the distance from the surface and θ_i is the incident angle. In our beam setup, this is much smaller than the coherence length of the lattice light.

For the blue-detuned lattice potentials, we use a fiber coupled superluminescent LED source (Exalos EXS7510). Interference filters cut the bandwidths down to a full width at half maximum (FWHM) width of $\approx 3\,$nm centered at $755\,$nm, corresponding to a coherence length of $\approx 190\,\mu$m. It is than passed through multiple stages of amplification using solid-state waveguide tapered amplifiers (Eagleyard) to produce enough optical power for the lattices. For the red-detuned dimple beam and confinement beam, we use broadband light derived from an amplified spontaneous emission (ASE) source (Superlum S830) that is filtered to a spectral width of $\sim 1\,$nm centered at $840\,$nm, and also amplified by tapered amplifiers.

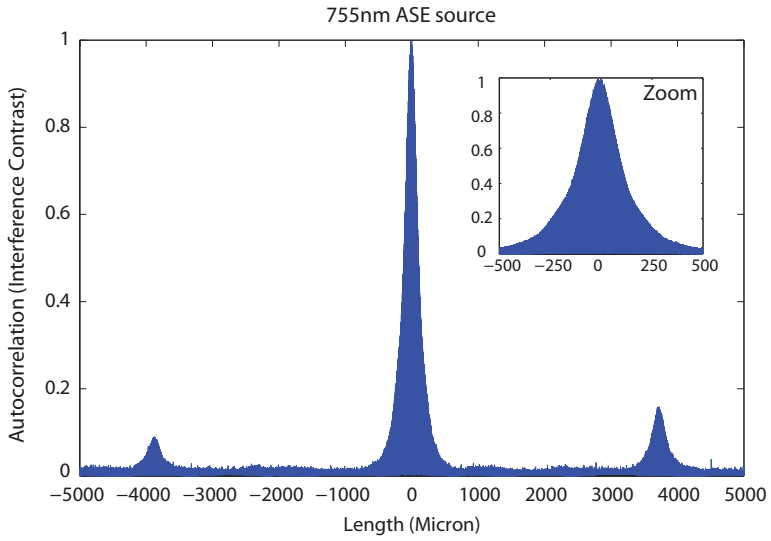

Figure 4.1: Coherence length of the blue detuned lattice light: Plotted is the interference fringes from a Michelson interferometer. The period of the oscillation $\lambda/4$ (too small to see in the plot) gives the absolute length scale, while the envelop of the fringes gives the coherence length. Small revivals are seen at an OPL of $\sim 4\,\mathrm{mm}$ away.

After the beams are passes through in fibers to the experiment table, interference filters are again used to clean up the spectra, and block any resonance light. Trace amounts of resonant light can be generated from the broadband ASE of the tapered amplifiers or from nonlinear processes in the optical fibers. The blocking of the resonant light is critical for achieving the long coherent life time of atoms in the conservative lattice. For the near-resonance pinning lattice, blocking ASE at 780 nm reduces backgrounds counts during fluorescent imaging.

The measured coherence length of the 755 nm light used for the lattice is shown in Figure 4.1. The light is interfered with itself in a Michelson interferometer with moving retroreflectors (Burleigh wavemeter WA-20), and the coherence is obtained from the interference contrast as a function of the OPL difference. The FWHM coherence length is about 200 nm, and a OPL of $\sim 1\,\mathrm{mm}$ is needed to eliminate interference. There are small revivals that are about 4 mm away at a contrast ratio of $\approx 10\%$. This

corresponds to an intensity of $\sim 10^{-4}$, and most likely comes from etaloning effect during the spectral filtering or amplification stages.

4.3 Spatial filtering in the Fourier plane

Using temporally incoherent sources for the optical potentials, we have eliminated undesirable interference between light that are separated in time by much more than the coherence time $t_{coh} \sim c/l_{coh}$. But components with different spatial frequencies can still interfere. For the 2D lattice, the two spatial frequency components at $\pm k_L$ interfere to give the periodic structure. Any other spatial frequency components will interfere with these two to produce corrugations and disorder on the lattice. One way to reduce such disorder is to spatially filter in a Fourier plane to leave only the wanted spatial frequencies. We do this at the Fourier plane at the back surface of the objective, right before the beams enter the microscope objective.

In the experiment, the 2D lattice along each axis has an overall Gaussian intensity profile of waist $w \sim 100\mu m$ in the plane of the atoms. The Fourier plane profile are two Gaussians with waist $w_{FP} = \lambda f/\pi w \sim 15\mu m$. Imperfections in the optical system that creates phase and amplitude variations in the Fourier plane: The holographic mask leaves some intensity in the zeroth order, aberrations in the optical setup distorts the wavefront and thus the Fourier plane profile, and dust and imperfect lens surfaces could scatter light into all spatial frequencies.

The 2D lattice setup

The optical setup for projection of the 2D lattices is shown in Figure 4.2. The lattice is generated by imaging two holographic masks (one for each axis) onto the atoms with the 400 mm lens and the objective in a $4f$ configuration. The Fourier plane of the

imaging system sits at the back surface of the objective. Only the +1 and −1 diffraction orders from the holograms are collected inside the aperture of the objective, to give a sinusoidal lattice in the plane of the atoms. The polarization of the lattice beams are aligned perpendicular to the lattice directions to ensure proper interference at the atom plane, hence the two axes of the 2D lattice have orthogonal polarizations and they are combined on a polarizing beam-splitter cube. The 755 nm physics lattice and the 795 nm pinning lattice are combined before the hologram. The paths for fluorescence imaging and projection of light potentials through the objective are combined with the lattice projection path with a non-polarizing beam-splitter.

Pinholes for spatial filtering

The detailed setup for Fourier filtering of the 2D lattices is illustrated in Figure 4.3. Because of the wavelength difference between the physics and pinning lattices, the spacing between the ±1 orders of the hologram are different in the Fourier plane. The full Fourier plane aperture of the objective is 18 mm. The ±1 orders are *sim* 14 mm apart and in both order the 755 nm lattice and the 795 nm lattice are separated by roughly 0.7 mm. The 755 nm physics lattice are filtered by pinholes of 150 m diameter. The pinning lattice is insensitive to disorder as long as there's enough depth to pin the atoms during imaging, thus they are passed through pinholes of much larger diameter at $\sim 600\,\mu$m. These bigger pinholes allow us to fine tune the relative position between the pinning lattice and the physics lattice. Both pinholes are machines on a blackened aluminum sheet. To block any light from the 755 nm lattice that might leak through the bigger pinhole, a thin dichroic interference filter (Laseroptik) is epoxied on top of the big pinhole which blocks 755 nm light but transmits at 795 nm. Each pinhole assembly is mounted on a two-axes stepper motor translational stage, and can be moved in the Fourier plane.

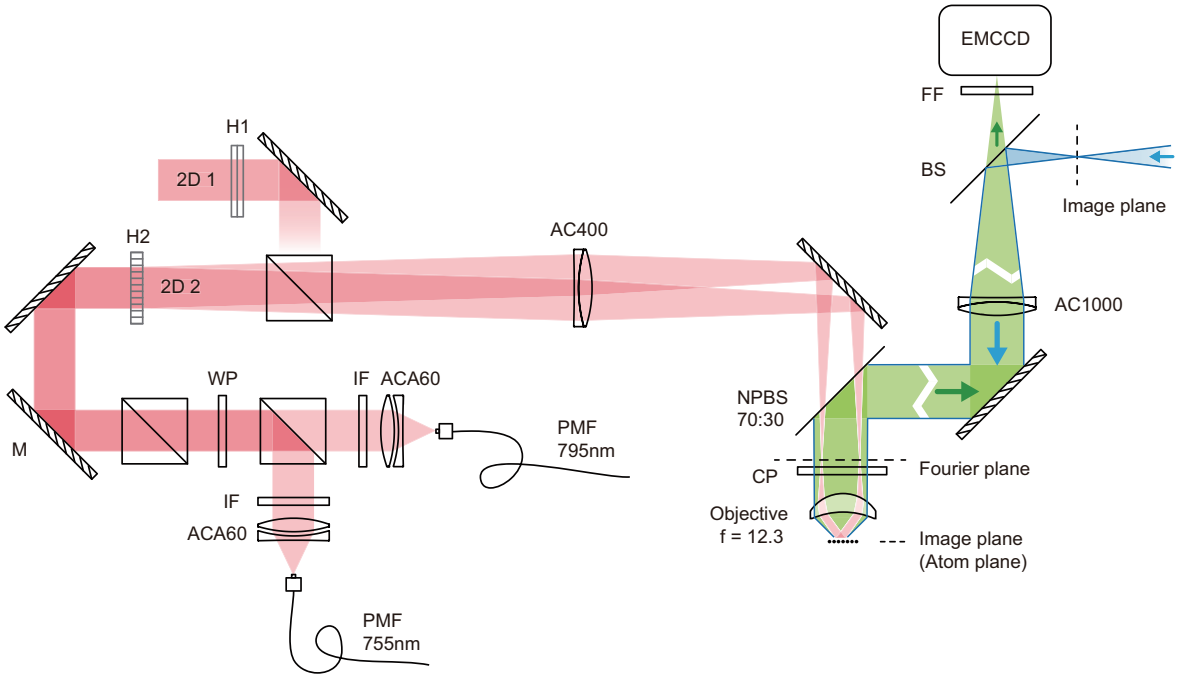

Figure 4.2: The 2D lattice setup. Each holographic mask gives lattice structure in one direction. The lattices of two different wavelengths are combined using a bi-wavelength wave-plate (*WP*: λ retardation for 795nm, $\lambda/2$ for 755nm). For clarity, the lattice 2D1 is not shown beyond the combining polarization beam splitter cube. A non-polarizing beam splitter above the objective combines the lattice path (*Red*) and the imaging path (*Green*). The imaging path has a one meter lens that images the atoms onto an EMCD camera (Andor Ixon) with a magnification of ~ 80. A compensation plate (*CP*) is placed in the Fourier plane of the imaging path to correct for aberrations [32]. The imaging path is also used to project other potentials onto the atoms through the microscope (*Blue*). The slightly different angles of the 755nm and 795nm lattice after the hologram and the spatial filtering setup are omitted here, and detailed in Figure 4.3. Distances are not drawn to scale.

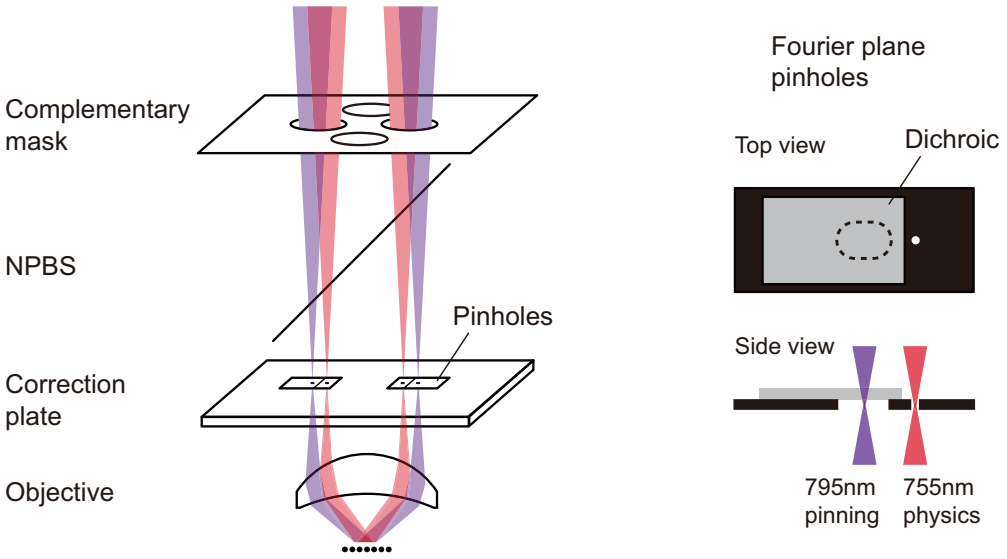

Figure 4.3: Illustration of the lattice beams around the Fourier plane, showing the pinhole assembly and complementary mask for spatial filtering. For clarity only beams and pinholes for one lattice axis are shown. Also not shown are the translational stages that move the pinholes in the Fourier plane. Distances, and sizes of the beams and pinholes are not drawn to scale.

In addition to the pinholes, a complementary mask covers the rest of the Fourier plane not already covered by the pinhole assemblies. In particular, it blocks the residual light in the zeroth order of the holograms at the center of the Fourier plane. The mask is placed above the beam splitter plate to avoid blocking the imaging path.

Alignment

The position of the lattice beams can be monitored directly on the EMCCD camera, by imaging the small amount of light that is reflected at the substrate surface and comes out back through the objective. The lattice beams are centered in the Fourier plane, and the focus of the beams are tweaked to have the tightly focused Fourier plane waists positioned exactly at the plane of the pinholes. The pinhole assemblies are aligned

individually by moving the translational stages and optimizing the filtered beam profile on the camera after having passed the pinhole.

The pinning lattice is aligned to co-propagate with the physics lattice, the dots in the Fourier plane are symmetric around the dots of the physics lattice. Because of the chromatic focal shift of the objective, the phases of the pinning lattice and the physics lattice may not be perfectly identical. When the pinning lattice is ramped on quickly to freeze hopping of the atoms in the physics lattice, an offset in the phases of the lattices lead to additional heating and is detrimental to the imaging fidelity.

We fine tune the phasing using Kapitza-Dirac scattering of atoms in a 2D superfluid. For a certain pulse time, the powers of the 755nm and 795nm lattice are adjusted so that individually they each imprint the same amount of phase on the atoms. Then when the pulse time is halved with both lattices on simultaneously, the atoms will only diffract by the same amount if the two lattices are perfectly in phase hence the depth doubled. To adjust the relative phase between the two lattices, the pinning lattice is moved along the lattice direction in the Fourier plane.

It's worth noting that the chromatic shift of the objective causes the lattice constants of the physics lattice and pinning lattice to differ by $\sim 1/300$. This limits the the effective field of view of the quantum gas microscope to on the order of ~ 100 sites, which is much bigger than the many body systems of interest.

The nearly circular Mott insulator shells after applying the Fourier filtering of the lattice beams are shown in Figure 4.10.

Limitations of spatial filtering

The spatial filtering scheme is effective in filtering out higher spatial components generated before the Fourier plane of the objective. But any disorder created after the pinholes will affect the atoms. The more than 10 surfaces of the custom objective can

also contribute to minute amount of scattering, and any scattering at the substrate surface could lead to significant disorder on the atoms due its proximity to the cloud.

The exact shape of the filtered potential is sensitive to tiny variations in the alignment of the pinholes, making the potentials susceptible to drifts in the pinhole position. Mechanical vibrations of the pinhole assemblies might also lead to intensity noise on the filtered potential. It's also hard to switch to different lattice configurations where the shape and the locations of the beams in the Fourier plane are different, and would require new pinhole and mechanical designs.

4.4 Spatially incoherent light source

While spatial filtering works by trying to block any unwanted spatial components that interfere to give disorder on the beams, we now seek a method that tries to wash out the interference of these spatial components by making the beam *spatially incoherent*.

As an example, consider disorder due to scattering from a small circular opaque scatterer place between the light source and a screen. For a single incident beam, we would see an Airy pattern on the screen which comes from diffraction at the scatterer. If the incident beam comes in at a different angle, the Airy pattern gets shifted from the center of the screen. Now if the scatterer is illuminated by incident beams from a range of different angles that do not interfere, the Airy disk is effectively shifted around and gets "washed out" in the image plane, to give a much smoother (less-disordered) output beam. In the language of Fourier optics, different angles in the image plane corresponds to different spatial frequency components of the imaging system. Just as a spread of different temporal frequencies results in temporally incoherent light, a spread of spatial frequencies leads to spatially incoherent light.

Such a configuration can be realized using an array of parallel beams and a single

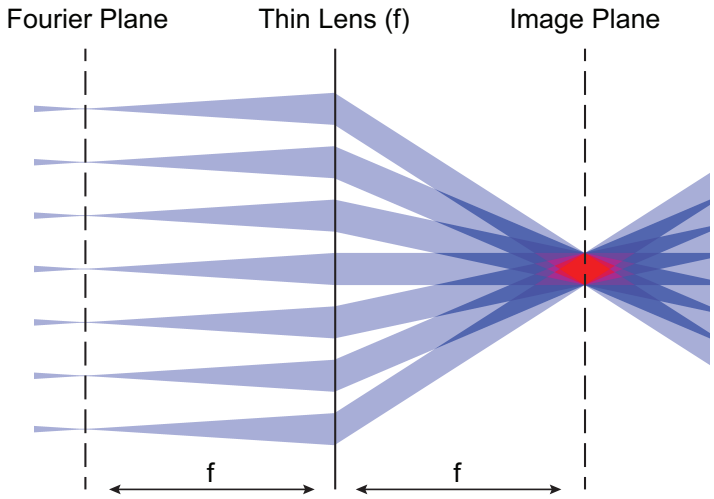

Figure 4.4: Illustration of spatial incoherent light: Each position in the Fourier plane corresponds to a spatial frequency component, and mapped to an angle in the image plane. We seek to have a spread of different spatial frequencies and thus a spread of different angles at which the image plane is simultaneously illuminated.

lens, as illustrated in Figure 4.4. A single lens maps the position in the Fourier plane onto angles in the image plane, and angles in the Fourier plane onto position in the image plane. If instead of a single focused beam in the Fourier plane, there are an array of parallel beams in the Fourier plane. These beams will all intercept in the image plane at different angles, but form an image identical to that from a single beam, as long as the different beams are temporally incoherent and do not interfere with each other.

4.4.1 Etalons for generating spatially incoherent source

We use mirror coated etalon plates to create the array of parallel beams in the Fourier plane, as shown in Figure 4.5(a). This is the same configuration as what is used for creating a virtually images phased array (VIPA) [47]. The front surface of the etalon is half AR coated for the entrance beam and half high reflectivity mirror coated,

the back surface of the etalon is coated with a partially transmitting mirror coating with a gradient in the transmission. The gradient coating is designed so that most of the incident power is distributed relatively uniformly across the output beams. The thickness of the etalon is such that the OPL difference between adjacent beams is longer than the coherence length of the light used, so that the n different beams remain incoherent. To create a 2D array of beams, a second etalon can be used. It needs to be more than n times thicker than the first one so that no two beams in the array interfere. This also means to keep the spacing of the beams the same in both directions, the thicker etalon need to be designed for a much smaller incident angle. Figure 4.5(b) shows an image of the array created in the Fourier plane, showing $\sim 20 \times 20$ beams with a spacing of 1 mm. The waist of the beams is $\sim 50\,\mu$m. The beams have different sizes in the Fourier plane because of their different OPL traveled inside the etalons, but they still have the exact same intensity profile in the image plane.

4.4.2 Performance of spatially incoherent light

Qualitative behavior

We can intuitively understand the effectiveness of using spatially incoherent light for reducing disorder. We try to relay an optical image (e.g. of a smooth light potential) from one image plane to another using spatially incoherent light, assuming we also have access to a Fourier plane of the imaging system.

If a point scatterer is localized in the Fourier plane, the spacial profile in the image plane does not change. This is because a single spatial component cannot create any structure in the image plane. It can only contribute to a small global offset in the image plane.

For scatterers situated in between the Fourier plane and the image plane, the

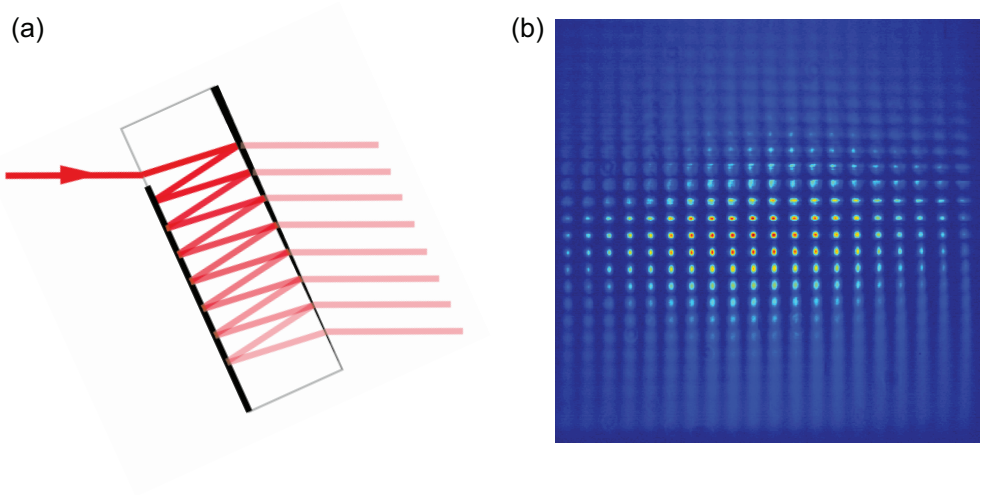

Figure 4.5: Generating the spatially incoherent source. (a) Illustration of the etalon design. An array of parallel beams are created after the etalon. The entrance surface is anti-reflection/high-reflection coated, while the exit surface is gradient coated to give a desired intensity profile over the array of beams. For creating a 2D array, two etalons with very different thickness are used to avoid interference between any two beams. (b) Image of a 2D array of $\sim 20 \times 20$ dots, with a spacing of 1 mm and waist of $\sim 50\,\mu$m. Note that despite the different waist location of all the dots and therefore the different size in the Fourier plane, all dots will overlap in the image plane with the same beam size.

scattering pattern gets averaged by the different beams. We expect this to be more effective the closer the scatterer is to the Fourier plane. Close to the Fourier plane, the point scatterer is sampled by only one or a few of the beams, thus the disorder gets suppressed by the maximal factor of N, N is the total number of independent beams in the Fourier plane (or different spatial "modes"). As beams travel closer to the image plane, they come together and gradually start to overlap. Therefore for scatterers closer to the image plane, the averaging becomes less effective as more beams are affected by the scatterer.

When the scatterers are exactly in the image plane. Since all beams in the spatially incoherent setup overlap exactly in the image plane, the intensity disorder from the scatterer will be images directly onto the atoms and cannot be corrected. One such example is dust particle on the holographic masks. Since the lattice spacing is the smallest feature that can be created on the atoms, the scattering from dust particles on the hologram with sizes smaller than that of the lattice spacing at the hologram ($\sim 30\,\mu$m) are effectively filtered by the objective aperture. Even for scatters with comparable sizes to the hologram spacing, the resulting disorder is localized in the image plane and only effect few isolated sites. Common dust particles that come to rest on optics and cannot be easily blown away have sizes in the range from sub-micron to $\sim 10\,\mu$m and falls into the situation we just described.

Qualitatively, we expect that if the spatially incoherent light source has a larger spread in the Fourier plane, it would be able to correct for disorder created from a distance closer to the image plane. At the same time, we will have a smooth potential in the image plane up to a higher spatial frequency.

Quantitative test setup

To study the performance of the spatially incoherent light setup, we use the setup shown in Figure 4.6. A 2 mm asphere is used to create a beam with a waist of 100 μm placed at the Fourier plane where the etalons are. The thin etalon has a thickness of 1 mm placed at $\sim 45^\circ$ while the thicker etalon has a thickness of 15 mm at $\sim 2^\circ$ in the other direction. An array of 10×10 dots are retained from the output of the etalons with a spacing of 1 mm and approximately uniform intensity distribution. The coherence length of the 3 nm wide 755 nm source ensures that all dots remain incoherent to each other. A single lens then focus these Fourier plane dots onto a single spot in the image plane. In order to have a large diameter beam in the image plane to cover the hologram, the size of the Fourier plane is shrunk by a factor of 10 using a 10:1 telescope in 4F configuration. From there, a single 100 mm lens is placed $2f$ away to image the shrunken Fourier plane onto the Fourier plane of the objective. The hologram is placed right next to the 100 mm lens. To correct for the wavefront curvature created by the single lens imaging, a field lens of 200 mm focal length is placed in the Fourier plane of the objective. This field lens also ensures that the hologram is properly imaged onto the focal plane of the objective. Another identical objective is used in reverse together with a one meter lens to image the image plane profile on a CCD beam profiler. The objectives used in the test setup are *achromatic* microscope objectives (Edmund Optics, effective $f = 10$ mm, NA $= 0.6$).

We simulate disorder by placing a dusty microscope slide between the hologram (in the image plane) and the field lens (in the Fourier plane), it's distance to the hologram is denoted d.

An aperture is placed after the etalons with a diameter of D, which controls how many Fourier plane dots (modes) are used. D is varied between 2 mm when only a single dot is passed, to 12 mm when roughly all dots are passed. This corresponds to a

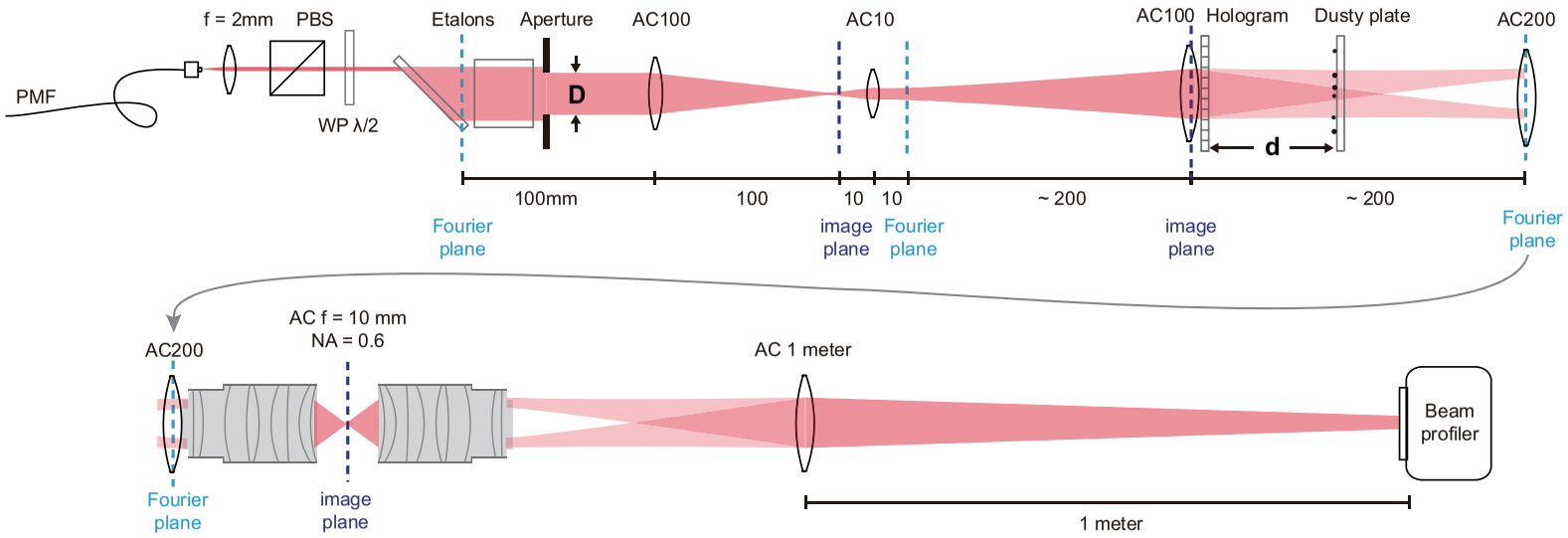

Figure 4.6: The setup used to test the performance of spatially incoherence sources. The degree of incoherence can be varied by the Fourier plane aperture D. The dist plate at distance d from the hologram can be moved anywhere between the image plane and the Fourier plane to study the resulting disorder.

Fourier plane spread of $\sim 1.2\,\text{mm}$. The spacing between the ± 1 orders of the lattice is $\sim 7\,\text{mm}$ in the Fourier plane for in this setup. This gives a ratio of the Fourier plane spread of the incoherent source to the Fourier plane separation for the lattice structure $\Delta k/k_{latt}$ of $\approx 1/3$. This value is close to what we could use for the actually lattice generation, since a bigger spread of the incoherent source would not be able to fit through the Fourier plane of the objective.

Figure 4.7 shows the measured image plane profile over a region equivalent to 50 by 50 lattice sites, for the limiting cases of $D = 1\,\text{mm}$ and $D = 12\,\text{mm}$ and various values of d. All diffraction orders expect the $+1$ order from the hologram are blocked so that we can observe the disorder on an individual beam caused primarily by the dust plate.

To quantify the disorder, we take the frequency spectra of the images, and calculate the radially averaged power spectral density:

$$S(k) = \frac{\int_{|\mathbf{k}|\approx k} |\mathcal{I}(\mathbf{k})|^2 \, d\mathbf{k}}{\int_{|\mathbf{k}|\approx k} d\mathbf{k}} \tag{4.1}$$

where $\mathcal{I}(\vec{k})$ is the two dimensional Fourier transform of the recorded image plane intensity, and the spatial frequency k is measured in units of the inverse lattice spacing $1/a$. The power spectral densities for the images in Figure 4.7 are plotted in Figure 4.8.

For the spatially coherent case ($D = 2\,\text{mm}$, a single dot in Fourier plane), the dust plate creates disorder in the form of Airy disks. For small values of d, the Airy disks from different dust particles remain separated in space and contain high spatial frequency and relatively large amplitude intensity ripples. From the noise spectrum, we can see disorder with characteristic length scales from a few up to tens of lattice sites. As the dust plate is moved away from the image plane, the Airy disks expand and interfere where they overlap because of the spatial coherence. As a result of the expansion, the spatial frequency of the ripples reduces, so does the amplitude. In the noise spectrum, the spectral power in the higher spatial frequencies are increasingly

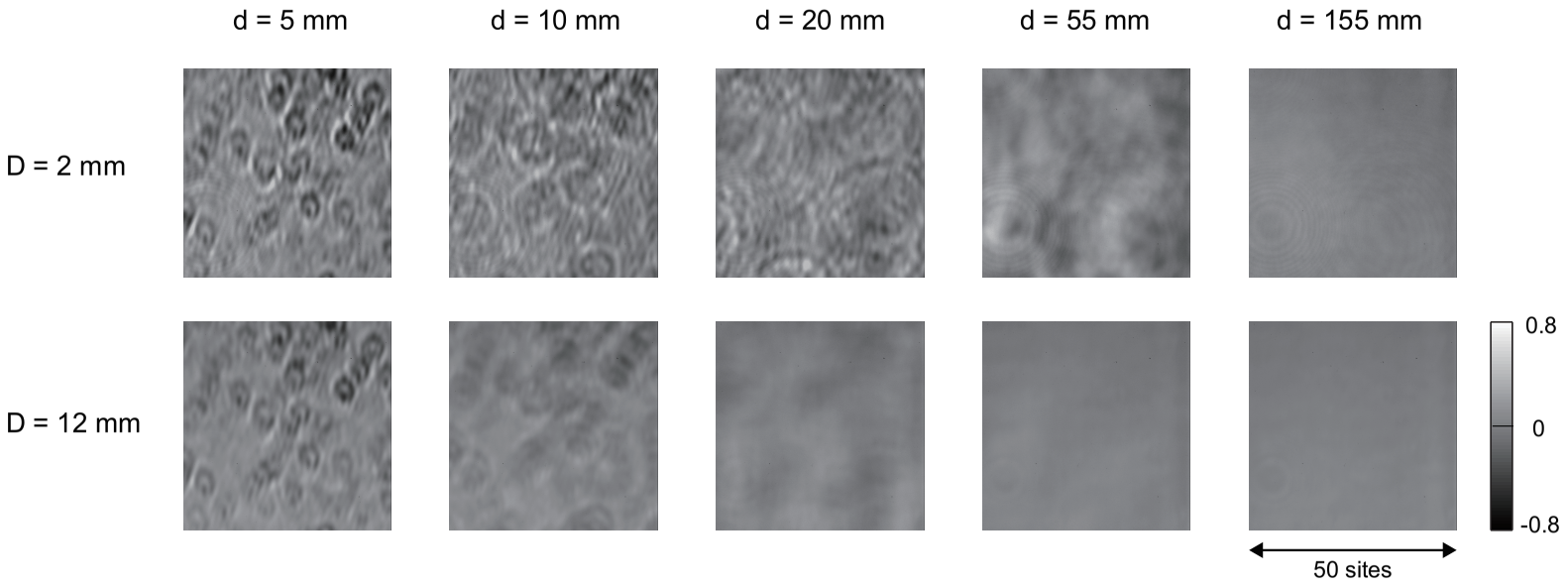

Figure 4.7: Images from the test setup illustrated in Figure 4.6, showing disordered potential caused by dust particles placed in various positions between the image plane and the Fourier plane. Top row for spatially coherent source, and bottom row for spatially incoherent source. A constant DC offset has been removed from the images to show the disorder. The color bar is in units of the DC offset.

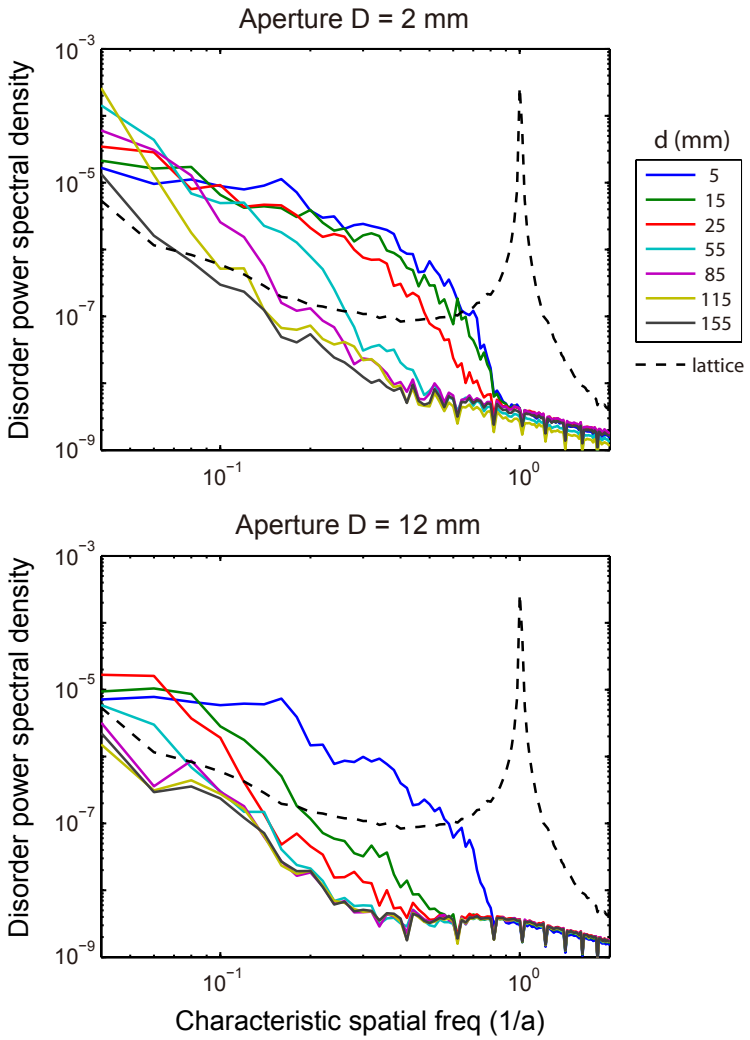

Figure 4.8: The radially averaged power spectral density of the disorder with varying positions of the dust plate, for both the coherent source ($D = 2\,\mathrm{mm}$) and spatially incoherent source ($D = 12\,\mathrm{mm}$). Normalized to power at DC. The dotted curve shows the lattice frequency at $1/a$ but its power is not properly normalized. The sharp dips on the curves are artifacts of the discrete Fourier transform.

suppressed. Eventually when the dust plate is placed close to the Fourier plane, the image plane profile is affected only slightly with low spatial frequency variations.

For the spatially incoherent case ($D = 12\,\mathrm{mm}$), the situation remains the same for dust in the vicinity of either the image plane or the Fourier plane. For intermediate planes, the spatial incoherence washes out the interference between Airy disks from different dust particles (or equivalently between different spatial components), and reduces the amplitude of the disorder. This is immediately seen in the noise spectra when comparing to the spatially coherent case.

In Figure 4.9 we plot the power spectral density for different distance of the dust plate from the image plane d, and for each d vary the amount of incoherence by changing D. The suppression of disorder show the same qualitative behavior as the discussion above. For the most incoherent source ($D = 12\,\mathrm{mm}$), we see significantly reduced disorder for dust particles no closer than 10% of the focal distance from the image plane. In the spatial frequency ranges corresponding to a few up to 10 lattice sites, we see residual spectral power of the disorder close to 10^{-8} level (corresponding to $\sim 0.04\%$ peak to peak intensity variation). The disorder remains below 10^{-6} level ($\sim 0.4\%$ peak to peak intensity variation) for ranges up to tens of lattice sites.

From results of the test setup, we believe the spatially incoherent light source could be used to create the physics lattice and other optical potentials in our experiment that are essentially disorder free on the scale of the Bose Hubbard dynamics, over fairly large regions.

4.4.3 Big lattice setup and characterization

We use the spatially incoherent light source for reducing disorder in the big lattice. In Chapter 7, the big lattice is utilized for the creation of a bilayer system and a smooth intensity profile in the plane of the atoms ensures homogeneous tunnel coupling between

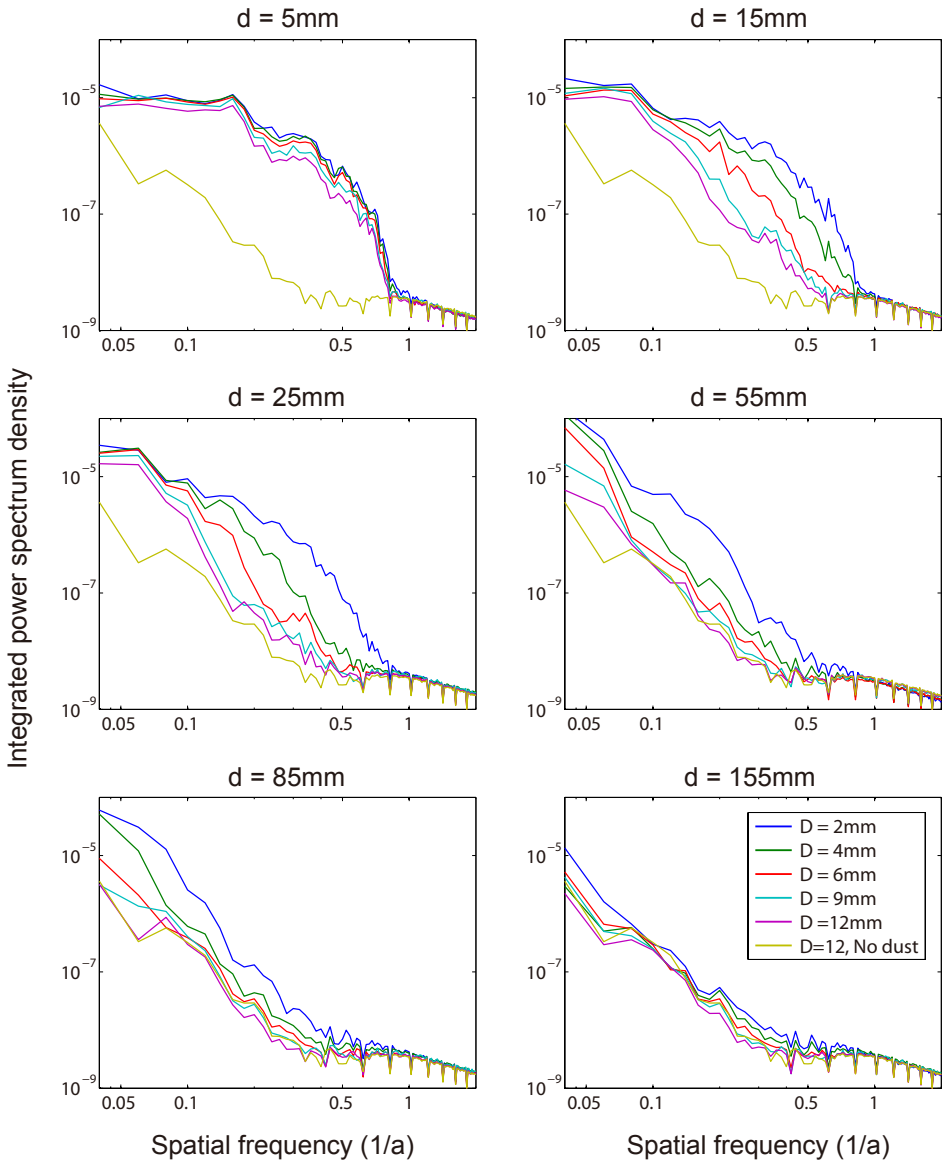

Figure 4.9: The radially averaged power spectral density with different positions of the dust plate (d), and different degree of incoherence (D). Normalized to power at DC. Sharp peaks at higher spatial frequencies are artifacts of the discrete Fourier transform.

the two planes.

The big lattice beam is reflected off of the substrate surface at a shallow incident angle which determines the spacing of the big lattice and its relative phase with the axial lattice. Therefore for the big lattice, only a 1D spread of wavevectors along the direction normal to its plane of incidence can be used for the incoherent light source. The same would be true if you want to use spatially incoherent light for the axial lattice.

For the big lattice setup, a linear array of 10 dots with relatively uniform intensity is created in the Fourier plane using the gradient-coated etalon. The beams are then compressed to an elliptical shape using an anamorphic prism pair. The prism pair minimizes aberrations (compared to e.g. using a high aspect ratio cylindrical telescope), which could cause the different Fourier plane dots to not overlap exactly in the image plane and hence degrade the disorder-correcting performance of the spatially incoherent setup.

The remaining disorder in the big lattice is characterized by measuring the variation of the trap frequency over the 2D cloud, described in detail the next section (Fig. 4.11). We measure a variation in the vertical trap frequency of 1% across a region of about 30 by 30 lattice sites, corresponding to 2% variation in the big lattice depth.

4.5 Characterization of disorder

The homogeneity of the lattice potential and the remaining disorder can be experimentally characterized in several ways.

Mott insulator shell shape

The shape of the Mott insulator shells is a direct indication of the local chemical potential, which in a harmonic confinement should show perfectly circular shells. Deviations from

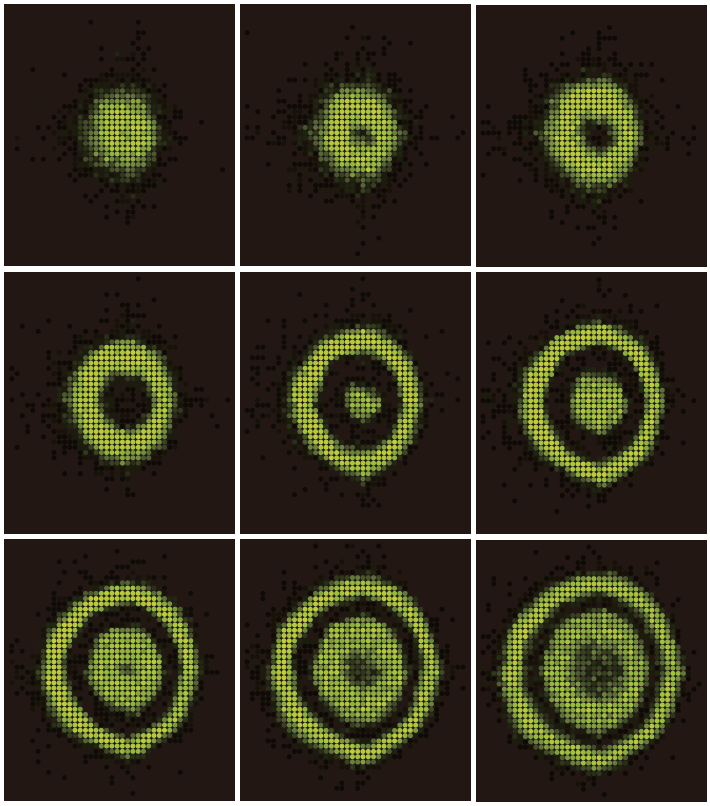

Figure 4.10: Averaged atom-number distribution in Mott insulators with increasing atom number, showing up to an $n = 4$ region. Since the imaging is only sensitive to the parity of the occupation number, we observe alternative bright and dark shells. Spatial filtering of the lattice beams before the objective reduces disorder, resulting in nearly circular shells.

round shells indicate disorder in the on-site offset from the 2D lattice or the dipole beam used to create the harmonic trap. By comparing the shape of the Mott insulator shell perimeters to the shape of the superfluid in the same harmonic trap, we can isolate the disorder from the lattice. This allows us to measure offset disorder down to values on the order of a fraction of U.

The nearly round Mott insulator shells after applying the spatial filtering in the Fourier plane (Sec. 4.3) are shown in Figure 4.10. The remaining variation in chemical potential from lattice disorder is on the order of tens of Hz around the shells.

2D time-of-flight expansion

Another way of measuring corrugations in an optical potential, is by looking at the trajectory of atoms moving in this potential landscape. For example, we can measure the atom distribution of a trapped condensate after a time-of-flight in the 2D plane. Disorders in the potential act like scattering barriers and causes spatial variations in the atomic density after the time-of-flight expansion. By varying the initial momentum of the expansion, we probe disorder on the order of the corresponding kinetic energy. In the limit of $k \to 0$, we are essentially measuring the local density of a condensate inside the trapping potential and thus the local chemical potential variations.

Modulation spectroscopy

Disorder in the trap frequency at each site can be measured via lattice modulation. By modulating the amplitude of the lattice at multiples of the trap frequency, atoms can be coherently excited into higher bands [48]. The tunneling rate in higher bands are several orders of magnitude bigger than that in the ground band, so the excited band population can be made to tunnel out of the lattice. By measuring the population left in the ground band as a function of the modulation frequency, we can accurately measure the trap frequency at each lattice site.

As an example, the disorder in the big lattice using the spatially incoherent setup is measured in Figure 4.11. The excitation frequency from the ground band to the 4th excited band is measured across the 2D plane. The spatial resolution of the quantum gas microscope allows us to probe the disorder locally, while the modulation offers high spectral resolution.

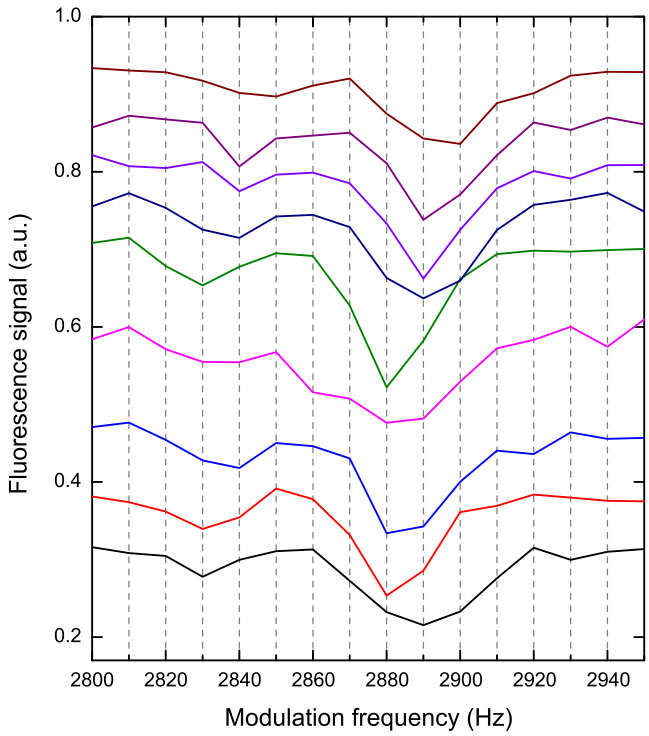

Figure 4.11: Modulation spectra of the big lattice in the axial direction. The big lattice is amplitude modulated to excite the atoms from the ground band to the 4th excited band. The excited population are ejected from the lattice and the remaining ground band population is imaged. The different curves show the averaged fluorescence signal over region of ~ 5 by 5 lattice sites each, and cover a total region of about 30 sites across. We observe a shift in the resonance of less than 20 Hz, corresponding to 2% lattice depth variation. The curves are vertically offset for visual clarity.

Chapter 5

Creating arbitrary potential with spatial light modulators

The ability to create arbitrary light potential on the smallest scale of a single lattice site would make it possible to initialize a wide range of initial states for the quantum simulation. It also enables the creation of localized excitations. The space- and time-resolved propagation of these excitations contains important information on the underlying many-body states [49, 50]. Shaped potentials with high spatial resolution also open the possibility of creating e.g. channels and boundaries for inducing controlled transport or realizing a single atom transistor [51].

In our complex imaging system, aberrations can distort the wavefront and severely affect the fidelity of the light potential we try to create. The ability to optically address single lattice sites relies on the diffraction limited performance of the imaging system. If aberrations in the projection path can not be corrected, the point spread function of the imaging system will be smeared out, making it impossible to create potentials with single site resolution.

Aberration correction and beam shaping can be achieved by using conventional

phase plates or amplitude masks. For example, we use glass correction plate in the Fourier plane of the objective to compensate for imaging aberrations arising from a design change of the imaging system (atoms now sit $\sim 10\mu m$ from the substrate surface, compared to $3\mu m$ in the original evanescent wave trap design [52]). As another example, spiral phase plates can be used to create different types of vortex beams. The limitation of these phase plates or masks is that they need to be specially designed and manufactured for each specific situation. This can be difficult when we need to create and vary arbitrary potentials, and when the aberrations are chromatic and we want to work with multiple wavelengths simultaneously.

In our experiments, we instead use adaptive optics as spatial light modulators (SLMs).

5.1 Digital micro-mirror device (DMD) as spatial light modulator

The spatial light modulators we use are digital micro-mirror devices. They are an array of tiny mechanical mirrors that can independently be switched to be in one of two angular positions. When a mirror is in the "ON" position, the incident light is reflected into the output direction; and in the "OFF" position, the mirror is tilted to reflect the light away from the output direction. The *DLP* series from Texas Instruments that we use have typically 1024×768 micro-mirrors (pixels) with a pitch of 10.8 μm, and a fill factor of $> 90\%$. The two angular positions of the mirrors are symmetric about the normal to the chip.

The rectangular array of micro-mirrors acts like a 2D diffraction grating. Illuminating the DMD uniformly from a single incident angle will result in a 2D grid of diffraction orders that leaves the DMD at angles that satisfy the grating equation. These angles

are determined by the pitch period of the DMD chip and the wavelength of the light used. The intensity distribution between the diffraction ordered is determined by the angle of the mirror at "ON" position, and the shape of the mirror which gives the overall envelop of the diffraction pattern. In our experiments we fix the incident angle such that the diffraction order with the highest intensity comes out normal to the DMD chip. This helps ensure that the plane of the DMD where the light being modulated is normal to the optical axis of our imaging system. All other diffraction orders are blocked.

Apart from DMDs, another type of SLMs are available based on liquid crystal display (LCD) technologies. Using the birefringence of liquid crystal, these SLMs can be configured to provide amplitude modulation or phase modulation. Liquid crystal based SLMs need to be driven by AC electric fields at a few kHz, making the modulated light to "blink" at the same frequency. This however can be a serious drawback for cold atom experiments where the trap frequency and other relevant energies are on the same kHz frequency range, and the blinking could lead to heating and decoherence. Since the light being modulated passes through the liquid crystal material, LCD SLMs have damage threshold lower then that of DMD SLMs. The optical properties of liquid crystal are also relatively temperature sensitive.

5.2 DMD in image plane

A first configuration of the DMD is to place it in an image plane of the optical system, so that it acts as an amplitude mask that is directly projected onto the plane of the atoms. The limitations to achieving arbitrary potential landscape for the atoms in this configuration come from the binary-amplitude nature of the DMD and the optical performance of the imaging system.

Although each pixel of the DMD can only be in one of the two states, we can achieve gray scale images by using multiple pixels for each lattice site. If the magnification is set so that a 10×10 pixel region on the DMD maps onto a single lattice site, the intensity the atoms see on that site will be the average over the 100 pixels because the numerical aperture of the imaging system does not support any feature smaller then a single site. We can thus achieve gray scale amplitude modulation at the expense of less effective resolution along each direction. The resolution of current DMD devices allows us to cover a region of more than 100×100 lattice sites, while having more than 100 levels of gray scale.

The intensity profile of the incident beam $I_{inc}(x, y)$ on the DMD can be measured with a camera in an intermediate image plane. To create a potential with intensity profile $I_{target}(x, y)$, the target intensity reflectance we want to generate on the DMD is:

$$R(x, y) = I_{target}(x, y)/I_{inc}(x, y) \tag{5.1}$$

The desired amplitude reflectance, $r(x, y) = \sqrt{R(x, y)}$, is then used by the binarization algorithm to generate the binary DMD pattern. For a given binarization algorithm, the delivered power as a function of the amplitude reflectance may not follow exactly the square root form. The exact functional form can be determined experimentally and used for the pattern generation.

For any given analog amplitude profile we want to create, we must find proper algorithms that minimizes errors introduced during the binarization of the profile used for the DMD. For a desired reflectance profile $r(x, y)$ with gray scale values in the range $[0, 1]$, the most naive approach is to set a fixed binarization threshold at 0.5, so that all pixels with $r > 0.5$ are turned on and the rest turned off. It's easy to see that the binarized images created using such a fixed threshold (sometimes referred to as average dithering) exhibit sharp artificial boundaries where $r \approx 0.5$. The pixelation of these

boundaries leads to strong artifacts at isolated spacing frequencies. This is illustrated in Figure 5.1(b).

Random dither algorithms can be used to eliminate these artifacts (Fig. 5.1(c)). Instead of a fixed threshold, the threshold is made to vary around 0.5 randomly for each pixel:

$$r_{bin}(x,y) = \begin{cases} 1, & \text{if } r(x,y) > 0.5 + f_{rand}() \\ 0, & \text{otherwise} \end{cases} \tag{5.2}$$

The random dither function f_{rand} is a random number generator with a distribution centered around zero, and values between ± 0.5. It is evaluated independently for each pixel. The effect of the random threshold is to smear out the artificial boundaries, and distributes the errors introduced by binarization into all spatial frequencies. One choice for f_{rand} is simply white noise.

In our real imaging system with a finite aperture size, only spatial frequencies inside of the numerical aperture passes through to reach the atoms. Therefore the atoms do not see noise created during binarization that have spatial frequencies outside of the objective Fourier plane. This makes it possible to design error diffusion algorithms [53] which push the dithering error away from lower spatial frequencies and out into higher spatial frequencies. The higher spatial frequency noise is then filtered out either by the finite NA imaging system or by further filtering with an iris in the Fourier plane.

A vast number of error diffusion algorithms are present which are originally developed for printing and digital image processing, and a common and simple one is the Floyd-Steinberg algorithm [54] which we use here to illustrate the principles of error diffusion.

Without error diffusion, the binarization (Eqn. 5.2) is applied independently on each pixel. The dithering error $\epsilon(x,y) = r_{bin}(x,y) - r(x,y)$ is also independent on each pixel giving rise to the relatively flat noise spectrum. With Floyd-Steinberg, the binarization is done in a sequential order. For each pixel the error is diffused into its neighboring

pixels that have not yet been processed to bias the dithering threshold on those pixels and locally compensate the error in r_{bin}. This is done by distributing $\epsilon(x, y)$ into the target reflectance of its neighbors according to the distribution:

$$\begin{pmatrix} \rightarrow & \rightarrow & \rightarrow & \rightarrow & \rightarrow \\ \rightarrow & \rightarrow & * & \frac{7}{16} & \cdots \\ \cdots & \frac{3}{16} & \frac{5}{16} & \frac{1}{16} & \cdots \\ & & \vdots & & \end{pmatrix} \tag{5.3}$$

The pixel with the asterisk is the currently binarized pixel at location (x_0, y_0), and the ones with the arrows are already processed. The arrows indicate the processing direction from left to right and from top to bottom. Each time the binarization error $\epsilon(x_0, y_0)$ is distributed to the four neighbors with the weights above by adding them to $r(x, y)$ before those neighboring sites are binarized. Thus if a particular pixel has been rounded up to 1 during the binarization, it becomes more likely for its neighbors to be rounded down to 0. Averaged over regions bigger than the size of the kernel above, the binarization error will now be close to zero. Hence the low spatial frequency binarization errors are greatly reduced. The removed noise is shifted to higher spatial frequencies, in the current example into error with period of ~ 2 pixels due to the alternating bias. This is illustrated in Figure 5.1(d).

It should be noted that the error diffusion algorithms are usually applied on top of the random dithering method. Algorithms with more complex kernel distributions or/and rastering sequences could give better error diffusion performances. It is also possible to apply the error diffusion algorithm multiple times iteratively to refine the result.

Another source of imperfection when projecting the target potential onto the atoms is aberration in the imaging system, which distorts the point spread function to inhibit

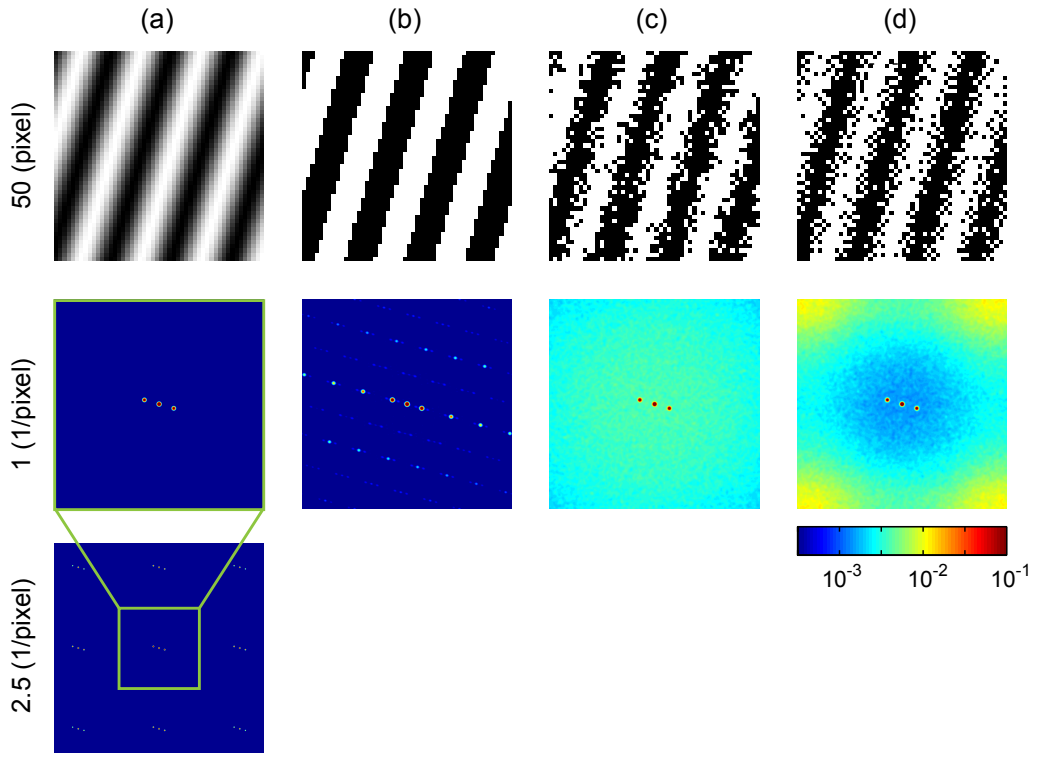

Figure 5.1: Binarization and error diffusion algorithm. (a) Gray scale image of a periodic intensity pattern we want to project (*Top*), whose Fourier transform is shown as two symmetric peaks at frequency of the periodic variation and a DC component (*Middle*). The grating created by the pixels of the DMD gives the different diffraction orders separated by the inverse pixel spacing (*Bottom*), and only one of them is passed through the imaging system. (b) Using a deterministic binarization method, artifacts appear at boundaries between regions of ON and OFF pixels. They are localized in the Fourier plane and can have any particular spatial frequency. (c) With random dither, the artifacts are eliminated by distributing the binarization error over the whole Fourier plane. (d) Applying the the Floyd-Steinberg error diffusion algorithm with random dither, the binary pattern appears more fine-grained compared to (c), and binarization errors are pushed to higher spatial frequencies. Note that if the DMD is setup with a magnification such that the pattern spacing here ($\sim$15 pixel) corresponds to one lattice site, then the physical aperture of the imaging system has a diameter defined approximately by the 3 dots, a region inside which binarization error is significantly suppressed by the error diffusion algorithm.

the projection of features with close to single site resolution. However for projecting beams with smooth, slowly varying profiles, distortion from aberrations is usually fairly small.

In summary DMD, placed in the image plane is best suited for creating relatively large scale smooth potentials with moderate intensities on the atoms. For creating small features with size close to a single site, only a few micro-mirrors are used which makes it extremely power inefficient. The errors from binarization also become more prominent when trying to generate small or sharp features, or patterns that require a big dynamic range.

Our setup in the experiment uses a DMD in the image plane with a demagnification of 15 pixel : 1 lattice site, and red-detuned light of wavelength 840nm with 1nm spectral width. It has been used for example to correct for long range disorder in the chemical potential in a Mott insulator [18].

Since the DMD used in this configuration only offers amplitude modulation, it is not possible to create light potentials with non-trivial phase topologies, e.g. vortex beams. This is in contrast to the DMD configuration introduced in the next section where an amplitude grating displayed on the DMD offers both phase and amplitude modulation.

5.3 DMD in Fourier plane

Another configuration for using DMD for spatial light modulation is to place the DMD in the Fourier plane of the imaging system. The amplitude modulation applied on the DMD will then be the Fourier transform of the potential we want to apply on the atoms. By using the DMD as an *amplitude grating*, it is possible to apply arbitrary phase modulation in addition to amplitude modulation. This makes it possible to create any light potentials for the atoms, including those with complex phase structures

[55]. In addition, the DMD in the Fourier plane can be used to measure the wavefront distortions in the imaging system and then exactly compensate the aberrations as a phase modulation in the Fourier plane. We have developed methods to use the atoms as probes to directly measure and null aberrations. This self-calibration capability ensures that we can always achieve diffraction limited performance and create arbitrary potential landscapes with single site resolution. The operational principal of our setup is similar to the one demonstrated in [56] for micro-trapping with optical tweezers.

A detailed description of our setups can be found in [57]. A one-dimensional amplitude grating is displayed on the DMD, and the first diffraction order is used as the output to be projected onto the atoms. The spacing of the amplitude grating determines the angle at which the first order emerges from the DMD which is in the Fourier plane, and corresponds to position information in the image plane. The DMD covers the whole aperture of the Fourier plane, thus includes all spatial frequency components. The amplitude of each frequency component can be changed by varying the width of the "ON" fringe in the grating. And the phase of the light at each position in the Fourier plane can be arbitrarily varied by shifting the phase of the amplitude grating locally. Examples of light potentials created using this setup are shown in Figure 5.2.

Contrary to the previous configuration with DMDs in the image plane, DMDs in the Fourier plane are better suited for creating small sharp features on the atoms. Large spatial scale potentials in the atom plane corresponds to using only a small region of the Fourier plane, and the DMD could start suffering from binarization errors, resolution limitations, and power inefficiency. Thus the two configurations complement each other and it is beneficial to have both available for effective quantum simulations.

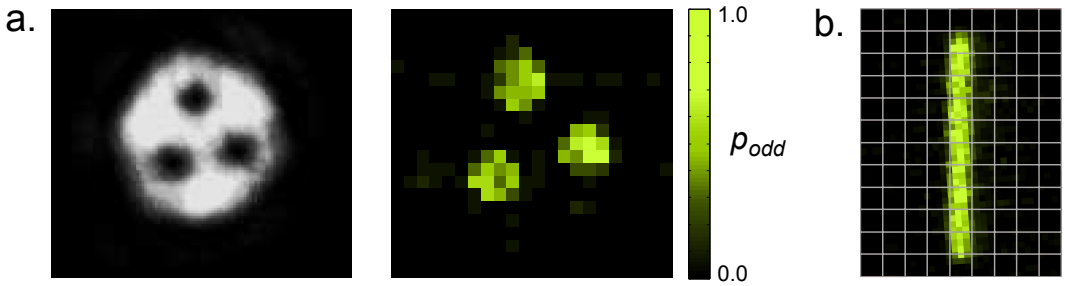

Figure 5.2: Examples of light potentials created with the DMD used as an amplitude grating in the Fourier plane. (a) Left: a blue detuned vortex beam with three vortices each with a phase winding of 2π, Right: small 2D condensates loaded into the repulsive potential and trapped at the center of the vortices, shown as averaged p_{odd} where each pixel corresponds to one lattice site. (b) A single shot image of a line of 10 atoms. A Hermite-Gauss beam is created with the DMD which traps a single line of atoms in a Mott insulator, while the rest of the atoms are ejected.

Chapter 6

Engineering dynamics with photon assisted tunneling

Portions of this chapter have previously appeared in the following paper:

> R. Ma, M. E. Tai, P. Preiss, W. Bakr, J. Simon, and M. Greiner, "Photon-Assisted Tunneling in a Biased Strongly Correlated Bose Gas," *Phys. Rev. Lett.* **107**, 1 (2011).

Advances in low-dissipation condensed matter materials have enabled studies of coherent dynamics in strongly correlated many-body systems [2]. Among other intriguing features, such systems may be excited to and studied in metastable states far from equilibrium. Such excitation takes a variety of forms, but is often realized by photon-assisted tunneling, where external photons provide the requisite excitation energy to drive spatial reorganization into long-lived excited states. This has been achieved via microwaves in coupled quantum dots [58, 59] and Josephson junctions [60], terahertz radiation in semiconductor superlattices [61], and near-single-cycle pulses in condensed matter systems [62].

Ultracold atoms offer a pristine platform for photon-assisted control [63, 64, 65] and probing [66, 67, 68, 69] of strongly-correlated states and the corresponding ordering. Here the photons are usually introduced by classical modulation of either the lattice phase [63, 64, 70] or amplitude [71, 65]. These engineered photons have been used to generate large-scale, coherent super-Bloch oscillations [65, 63, 64] and further employed for precision measurement of applied forces [71, 72]. Weak interparticle interactions have been shown to act as a decoherence channel that damps Bloch (and super-Bloch) oscillations and may be tuned away with a Feshbach resonance [73, 74]. Modulation with additional spatial variation provides a promising route to gauge fields [75, 76] and other exotic topological effects [77].

There is also a growing drive to investigate photon-assisted tunneling in the strongly interacting regime. Modulation spectroscopy presently provides the best temperature measurement of fermionic Mott insulators in the approach to quantum magnetism in the Fermi-Hubbard model[68]. Strong photon dressing may be used to null and even negate tunneling [78], a technique that has been employed to drive the superfluid-Mott insulator transition [79] and to simulate classical magnetism [80]. Coherent control of cotunneling was recently demonstrated by driving an optical double well [81].

6.1 Photon-assisted tunneling in a double-well

We consider photon-assisted tunneling driven by amplitude modulation of the lattice depth. It's instructive to begin with bosonic atoms in a biased, tunnel-coupled double well with time-dependent tunneling rate $J(t)$. The bias between the left and right wells is E, and the on-site interaction is U. The Hamiltonian for this system using the bosonic operators is given by:

$$H = -J(t)(a_l^\dagger a_r + a_r^\dagger a_l) + \frac{E}{2}(a_l^\dagger a_l - a_r^\dagger a_r) + \frac{U}{2}(a_l^{\dagger 2} a_l^2 + a_r^{\dagger 2} a_r^2)$$

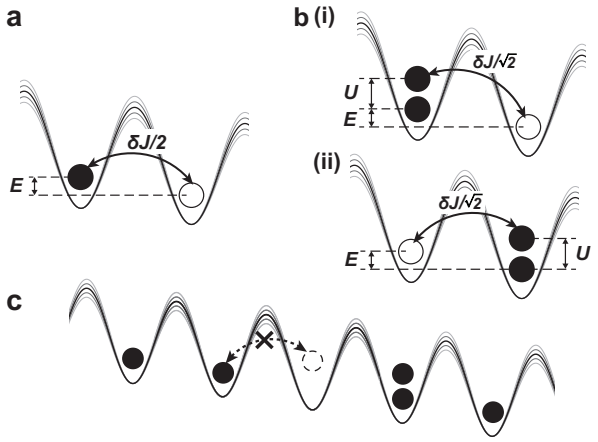

Figure 6.1: Photon-assisted tunneling. (a) For a single atom in a biased double well, tunneling is induced by lattice depth modulation at a frequency given by the energy gap E. (b) When there is one atom in each well, the energy gaps become $U + E$ for the right atom to tunnel onto the left atom (i) and $U - E$ for tunneling in the other direction (ii). The effective tunneling under modulation is Bose-enhanced by a factor of $\sqrt{2}$. (c)The double well physics may be extended to a one-dimensional lattice at unity filling (e.g. $n = 1$ Mott insulator). There is then an interaction blockade preventing photon-assisted tunneling on adjacent sites due to the resulting energy mismatch. Arrows denote photon-assisted tunneling, with open (closed) circles denoting the initial (final) location of the atom.

Here $a_l^\dagger$ ($a_r^\dagger$) is the bosonic creation operator for the left (right) well.

In the simple limit of large bias $E \gg |J(t)|$, no modulation ($J(t) = J$), and a single atom initially localized in the right well, tunneling to the left well is off-resonant. This off-resonant Rabi oscillation populates the left well with a small probability of $P_l(t) \approx 4J^2/E^2$.

By modulating the tunneling rate at the bias frequency E, $J(t) = J + \delta J \cos Et$, population is resonantly transferred between the two wells (Fig. 6.1(a)), resulting in full-amplitude Josephson-like tunneling oscillations occurring with an effective Rabi-frequency given by $\delta J/2$. The modulation provides the atom with photons with the

requisite energy to enable tunneling. The lattice is created by photons with frequency ω_L, and the modulation adds side bands at frequencies $\omega_L \pm E$. Thus the tunneling can be viewed as the result of a two photon process where the atom absorbs a photon from the carrier and emits into one of the sideband, or vice versa.

If instead we begin with two strongly interacting ($U \gg |J(t)|$) atoms, one on each site of the double well, the energy cost to tunnel now becomes $U + E$ ($U - E$) for the atom in the right (left) well to tunnel to the left (right) well (Fig. 6.1b. i,ii). By modulating at these new frequencies, one can induce tunneling in one direction or the other. Because of the indistinguishability of the atoms, the effective tunneling rate will be Bose-enhanced to $\delta J/\sqrt{2}$.

The double well picture can be directly extended to atoms localized in a one-dimensional optical lattice (Fig. 6.1(c). As in the double well case, tunneling is strongly suppressed in a Mott insulator by the repulsive onsite interactions [13]. A constant force resulting from an energy shift per lattice site of $E \neq U$ produces a tunneling energy gap that is dependent on the tunneling direction. Modulating the depth of the lattice (and hence, primarily, the tunneling rate) at a frequency equal to the energy gap enables the atoms to tunnel resonantly onto their neighbors. After such a photon-assisted tunneling event, two adjacent lattice sites each initially containing n atoms become a site with $(n + 1)$ atoms and a site with $(n - 1)$ atoms.

6.2 Modulation spectroscopy in a tilted lattice

We start with two-dimensional Mott insulators. At an initial depth of $45E_r$ in both lattice directions, tunneling between sites is negligible on the time scale of the following experiment.

A magnetic field gradient applied along the x direction produces a lattice tilt of

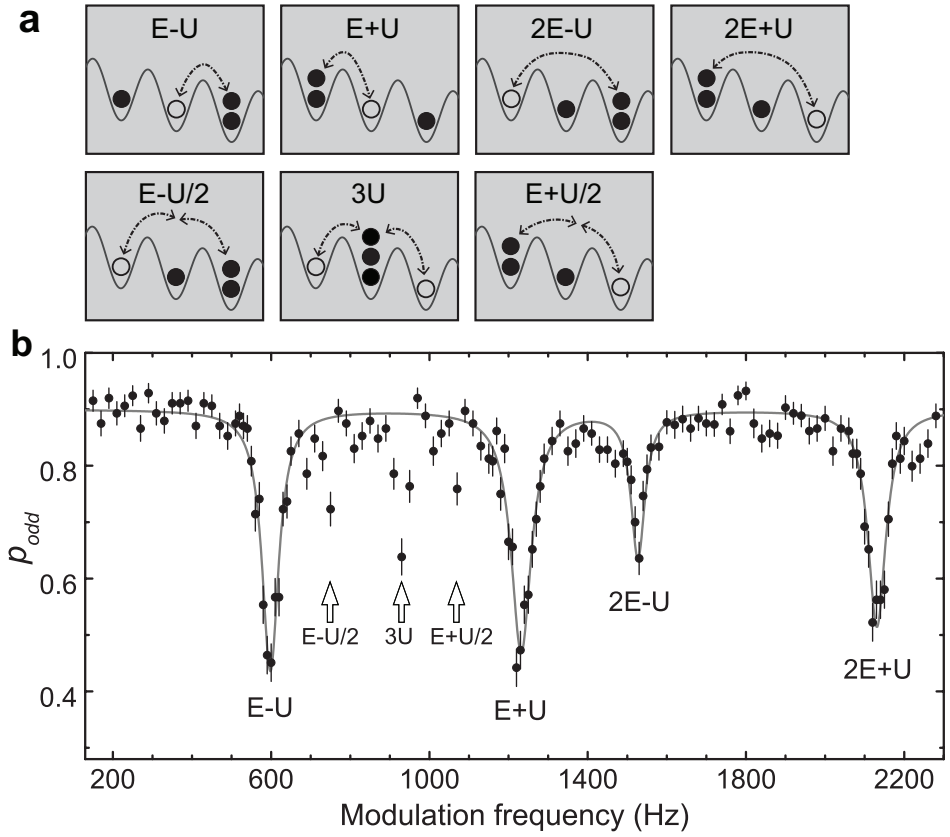

Figure 6.2: Modulation spectroscopy. (a) Schematic of the observed tunneling processes. (b) The occupation probability p_{odd} versus the modulation frequency. p_{odd} drops at each of the tunneling resonances, as many doublon-hole pairs are produced. Each resonance is labeled in accordance with the corresponding process described in (a). The modulation of the $9E_r$ x-lattice by $\pm 15\%$ corresponds to a Bose-enhanced photon-assisted tunneling rate of $2\pi \times 8$ Hz. p_{odd} is averaged over a region of 25 lattice sites for 8 realizations. The solid curve is a four-Lorentzian fit to the $E \pm U$, $2E \pm U$ features. In this letter, all errors in p_{odd} reflect 1σ statistical uncertainties in the region averages.

48 Hz/Site per Gauss/cm for our Mott insulator, prepared in the $|F = 1, m_f = -1\rangle$ state. The harmonic confining potential is compensated to minimize inhomogeneities in the tilt [82]. While applying a tilt of $E = 2\pi \times 915(10)$ Hz per lattice site, the lattice along x is adiabatically ramped down to $9(1)E_r$, converting the system into uncoupled 1D chains with tunneling rate $J = 2\pi \times 30(7)$ Hz and measured onsite interaction $U = 2\pi \times 317(10)$ Hz. Modulation of the x-lattice depth produces photon-assisted tunneling, which in a Mott insulator changes the parity of the onsite occupation as measured by our fluorescent imaging with single-site resolution. The experiment is repeated under the same conditions in order to compute the probability p_{odd} of odd occupation on each lattice site.

Figure 6.2 shows p_{odd} versus modulation frequency in an $n = 1$ Mott shell when the x-lattice is modulated by $\pm 15\%$ for 500 ms, sufficient time for damping of the many-body oscillations. The principal features are peaks at $E \pm U$ which correspond to the creation of nearest neighbor doublon-hole pairs, and $2E \pm U$ which correspond to a second-order process creating next-nearest neighbor doublon-hole pairs. The dependence of the resonance locations on the tilt E has been separately verified. We are also able to identify narrow resonances consistent with higher-order processes at $E \pm U/2$ and $3U$, which require two assisted tunneling events as illustrated in Figure 6.2. The principal peaks have typical widths of $\sim$60 Hz, set by residual lattice disorder.

6.3 Occupation-sensitive photon-assisted tunneling

6.3.1 Interaction induced multi-orbital effects in optical lattices

The Bose-Hubbard Hamiltonian (Eqn. 2.17) is derived under two approximations: The tight-binding approximation assumes deep lattices where the Wannier wavefunctions are sufficiently localized so that we can keep only the onsite interaction and nearest-neighbor tunneling terms. For the single band approximation, the interacting many-body wavefunction is constructed from only the ground band single particle wavefunctions. In the single band (or single *orbital*) model the on-site interaction term is:

$$U_{\mathrm{SO}}(n) = \frac{U}{2} n(n-1) \tag{6.1}$$

If we do not ignore the other bands of the optical lattice, atom-atom interactions can induce virtual excitations from the ground band to higher bands. Such small admixtures of higher bands modify the shape of the ground state wavefunction and lead to renormalized values of the tunneling and interaction. This multi-orbital shift [83, 84] makes the interaction strength dependent on the atom number, and we can write the interaction energy on a site with n atoms in terms of effective multibody interactions U_n:

$$\begin{aligned} U_{\mathrm{MO}}(n) = &\frac{U_2}{2!} n(n-1) + \frac{U_3}{3!} n(n-1)(n-2) \\ &+ \frac{U_4}{4!} n(n-1)(n-2)(n-3) + \ldots \end{aligned} \tag{6.2}$$

The interaction strength is the overlap integral between the density of the two atomic wavefunctions. So intuitively for repulsive interaction, as more atoms are added onto a lattice site, they repel each other which makes the overall wavefunction less localized

and results in a reduced pairwise interaction. This implies that U_3 will have an opposite sign as U_2. Note that these are *effective* multibody interactions, originating from only the two particle s-wave contact interaction due to the multi-orbital effects.

6.3.2 Calculating multi-orbital shifts

Variational method

A first estimation of the the multi-body interactions U_n can be obtained by a variational calculation. Assuming Gaussian wavefunctions for the n atoms localized on the same site, the interaction energy can be estimated by minimizing the ground state energy over the width of the Gaussian.

Perturbation theory

The multi-orbital shifts can also be calculated using perturbation theory. In [84], the effective three-body interactions U_3 is calculated as a summation over contributions from virtual excitations to higher bands. For higher occupancies or higher order multi-orbital effects, the number and complexity of the virtual processes increase drastically, making this approach difficult.

Lowest dressed band picture

To systematically calculate and include multi-orbital processes, one can define an effective lowest-band representation where the localized lowest energy states are dressed with contributions from higher bands [85, 86]. The full Hamiltonian for interacting bosons in a lattice can be written as the ground band Hamiltonian (Eqn. 2.14) with an additional summation over all vibrational bands. For example, the interaction term

will read:

$$H_{int} = \frac{1}{2} \sum_{\alpha_i,\alpha_j,\alpha_k,\alpha_l} \sum_{i,j,k,l} U_{i,j,k,l}^{\alpha_i,\alpha_j,\alpha_k,\alpha_l} \ \hat{a}_{i,\alpha_i}^{\dagger} \hat{a}_{j,\alpha_j}^{\dagger} \hat{a}_{k,\alpha_k} \hat{a}_{l,\alpha_l} \tag{6.3}$$

where α_i is the band index and

$$U_{i,j,k,l}^{\alpha_i,\alpha_j,\alpha_k,\alpha_l} = \frac{4\pi\hbar^2 a_s}{m} \int \omega_{\alpha_i}^*(x - x_i)\omega_{\alpha_j}^*(x - x_j)\omega_{\alpha_k}(x - x_k)\omega_{\alpha_l}(x - x_l) \ d^3x \tag{6.4}$$

Following the procedure described in [86], the goal is to find an effective lowest band basis for the interacting many-body system so that the interacting induced energy shifts and higher order processes can be expressed in the resulting effective single band model.

A complete eigenbasis for the single particle problem is the basis of Wannier functions on each site i. For the non-interacting many-body system, we can choose the eigenbasis to be local Fock states in all bands on each site:

$$\{|n_{i,\alpha=0},\ n_{i,\alpha=1},\ n_{i,\alpha=2},\ \cdots\rangle\}$$

With interactions, these states still form a complete basis, and on each lattice site we can diagonalize the many-body interacting Hamiltonian projected onto the local Fock space. The eigenstates then form a eigenbasis for localized states with contributions from all higher bands:

$$\left\{\left|\psi_m^{(n)}\right\rangle_i\right\}$$

where n is the local particle number, and m is the new state index. The low-energy space of the system is then formed by all local ground states ($m = 0$) with different particle number on each site i:

$$\left\{\left|\psi_{m=0}^{(n=0)}\right\rangle_i, \left|\psi_{m=0}^{(n=1)}\right\rangle_i, \left|\psi_{m=0}^{(n=2)}\right\rangle_i, \cdots\right\}$$

The effective lowest band for the system consists of all product states over the low energy space on each lattice site, and any many-body operators can be expressed in the

new dressed basis. The multi-orbital interaction energy $U_{mo}(n)$ we are interested in, is then simply the expectation value of the on-site interaction operator (corresponding to $i = j = k = l$ in Equation 6.3) for the dressed ground state $\psi^{(n)}_{m=0}$.

This lowest-dressed band approach allows the systematic inclusion of all higher order interaction induced effects. For example, the next order contributions from Equation 6.3 are nearest neighbor terms: the nearest neighbor interaction containing terms of the form $\hat{a}^\dagger_{i,\alpha_1}\hat{a}^\dagger_{j,\alpha_2}\hat{a}_{i,\alpha_3}\hat{a}_{j,\alpha_4}$, pair tunneling of the form $\hat{a}^\dagger_{i,\alpha_1}\hat{a}^\dagger_{i,\alpha_2}\hat{a}_{j,\alpha_3}\hat{a}_{j,\alpha_4}$, and the density-induced single particle tunneling of the form $\hat{a}^\dagger_{i,\alpha_1}\hat{a}^\dagger_{i,\alpha_2}\hat{a}_{i,\alpha_3}\hat{a}_{j,\alpha_4}$. Here i and j are two neighboring sites.

6.3.3 Measuring multi-orbital shifts with photon-assisted tunneling

The multi-orbital shifts have been observed by using quantum phase revival spectroscopy [83]. Here we take advantage of the high spectral and spatial resolution of our modulation spectroscopy, to direct measure the multi-orbital shifts and demonstrate occupation-sensitive photon-assisted tunneling.

For the Mott insulator shell with n atoms per site, the photon-assisted tunneling resonance at $U - E$ corresponds to the conversion of n atoms on each of two adjacent sites to $(n-1)$ and $(n+1)$. Thus, using the expression for multi-orbital interaction (Eqn. 6.2), the energy cost of this process is

$$\delta U_{\mathrm{MO}} = U_{\mathrm{MO}}(n+1) + U_{\mathrm{MO}}(n-1) - 2U_{MO}(n) - E$$

The photon-assisted tunneling resonances of the $n = 2$ and $n = 3$ shells are therefore shifted by $\delta^{n=2}_{\mathrm{MO}} = U_3$ and $\delta^{n=3}_{\mathrm{MO}} = 2U_3 + U_4$ relative to that of the $n = 1$ resonance. Using the multiband perturbation calculation [84] we predict $U_3 = 2\pi \times -23(1)$ Hz, while a

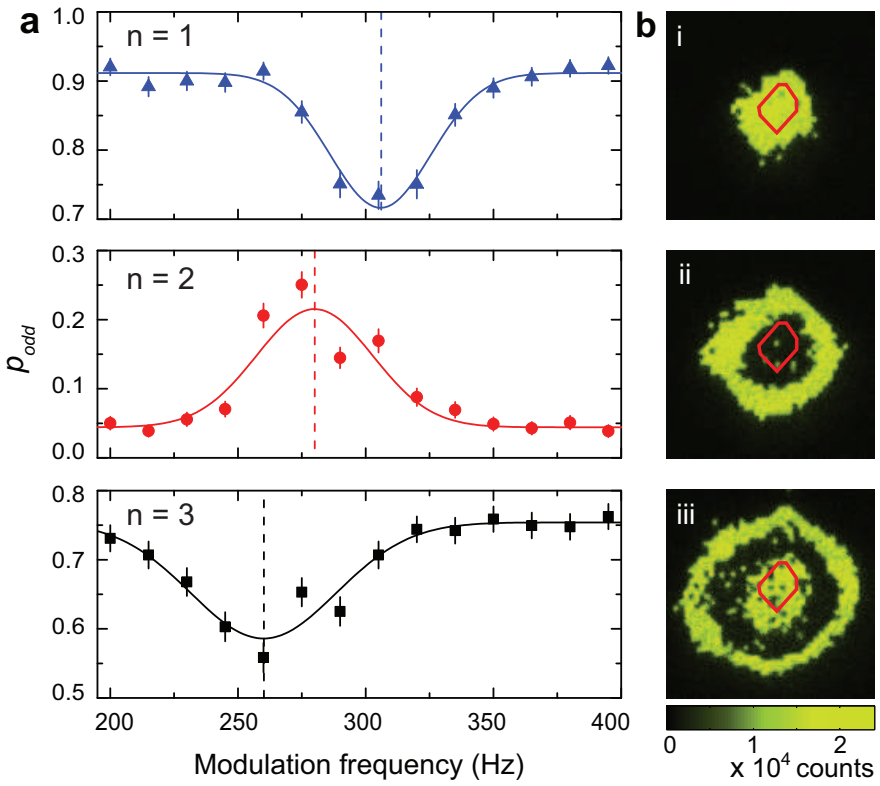

Figure 6.3: Number-sensitive photon-assisted tunneling using multiorbital shifts. (a) Modulation spectra of the $U - E$ resonant peaks in $n = 1, 2, 3$ Mott insulator shells. Fitted to Gaussian profiles (solid curves), the peaks are located at 306(2) Hz, 280(3) Hz, and 260(3) Hz respectively (dashed lines). (b) *In situ* images of the $n = 1, 2, 3$ Mott shells ($i - iii$) without modulation, with the 49-site region studied in (a) enclosed by the red solid line.

variational calculation (over Gaussian wavepacket r.m.s. size) yields $U_4 = 2\pi \times 6(1)$ Hz for our experimental parameters. The errorbars arising from uncertainty in the measured $U_2 = 429(15)$ Hz (in an $18E_r$ x-lattice).

Figure 6.3 shows a shell-resolved measurement of the tunneling resonance frequency for tilt $E = 2\pi \times 120(15)$ Hz. We observe shifts of $-26(5)$ Hz and $-46(5)$ Hz for the $n = 2$ and $n = 3$ shells relative to the $n = 1$ shell. The theory, discussed above, predicts $-23(1)$ Hz and $-40.3(1)$ Hz, respectively. The imperfect agreement for the $n = 3$ shell likely arises from higher-order effects such as superexchange interactions between adjacent lattice sites, which are not included in the aforementioned model and become increasingly important for larger occupations.

We have shown that we can drive photon-assisted tunneling in regions with different occupancy at different frequencies. For example, the $n = 3$ resonance and the $n = 1$ resonance are sufficiently separated in frequency that tunneling can be enabled for only one of them, or be tuned independently by applying a bichromatic modulation. Such occupancy-sensitive tunneling could be used to engineer exotic phases in a wide range of extended Hubbard models.

6.4 Quantum magnetism with photon-assisted tunneling

In a recent experiment in our quantum gas microscope, we have realized simulation of a one dimensional quantum Ising model using tilted one dimensional Mott insulators [82]. The effective magnetic model is obtained by mapping the many-body system's charge degree of freedom (i.e. atomic density distribution) to spins in a spin-1/2 chain with anti-ferromagnetic Ising interaction [87]. Here we show that photon assisted tunneling can be used to drive such a quantum phase transition and study the dynamics of

many-body states near the quantum critical point.

6.4.1 Anti-ferromagnetic Ising model in 1D optical lattices

In this section, we give a brief summary of the mapping from Bose-Hubbard dynamics to the spin Hamiltonian and describe the experimental observables.

The system we consider is a one-dimensional $n = 1$ Mott insulators in the deep Mott regime ($U \gg J$), as illustrated in Figure 6.4. When a small uniform tilt of E per site is applied along the 1D lattice, tunneling between lattice sites is suppressed by the energy gap in the Mott insulator of $\sim U$. If the tilt is increased, eventually at $E \approx U$ each atom in the Mott insulator can move resonantly onto its neighbor and tunneling dynamics is restored. However, if one atoms has tunneled from its original location in the Mott insulator, its neighboring atoms can no longer tunnel because of the energy gap of $\sim U$ created by the tunneled atom. This constraint is the origin of the spin interaction in the effective magnetic model. At tilts of $E > U$, it become energetically favorable for the atoms to tunnel onto its downhill neighbor, but the constraint that no two neighboring atoms can tunnel simultaneously let to a density wave ordering of the atoms.

Mapping to spin model

Sachdev *et al.* formulated the effective spin chain by associating a spin-1/2 to each link connecting two neighboring sites. An atom not tunneled on the link is defined as spin up along z-axis of the Bloch sphere ($S_z = +1/2$); and an atom tunneled corresponds to spin down ($S_z = -1/2$). An atom in the superposition of left and right on the link would correspond to a spin pointing in the $x - y$ plane of the Bloch sphere. The tunneling constraint now forbids neighboring down spins. We identify the Mott state as the paramagnetic state while the density ordered state as the anti-ferromagnetic state.

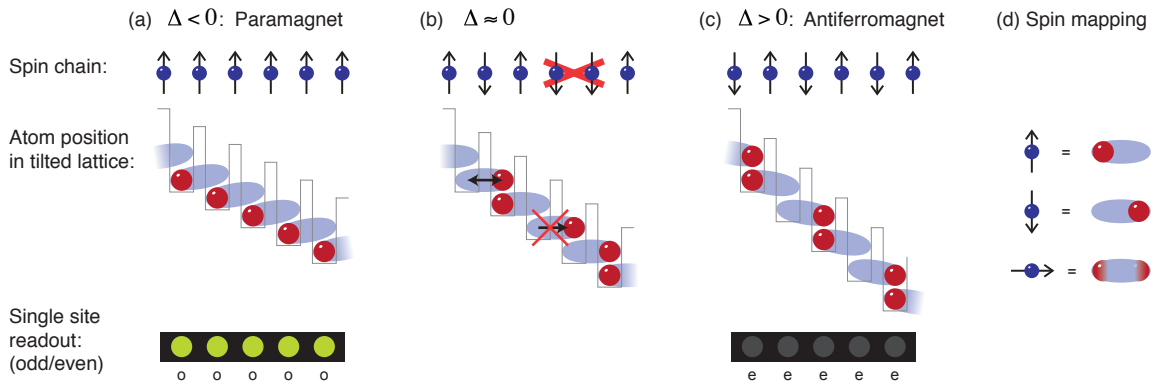

Figure 6.4: The Mott insulator in tilted 1D lattice and the mapping to a spin model. (a) As the lattice is being tilted, the atoms remain in the state with one atom per site as long as the tilt per lattice E is smaller than the energy gap to tunnel which is the interaction U. (b) At the critical tilt $E \approx U$, atoms can tunnel onto the neighboring site downhill, which the constraint that no two neighboring atoms can tunnel at the same time. (c) For large tilt, it's energetically favorable for all atoms to tunnel, but the constraint limits only every other atom to tunnel. (d) The spin model is derived by associating a spin-1/2 to each link between two sites. The constraint on tunneling forbids neighboring down spins, and leads to an effective spin-spin interaction. In the spin model, the Mott state is identified as the paramagnetic phase (PM) and the staggered state at large tilt is the anti-ferromagnetic phase (AF). Bottom: Experimental signature of the phase transition: With parity detection of our microscope, the PM phase is all bright whereas the AF phase is all dark. Figure adopted from [32].

The physics in the constrained subspace is formally mapped to a 1D anti-ferromagnetic Ising Hamiltonian with effective longitudinal and transverse magnetic fields:

$$H = \mathcal{J} \sum_i \left(S_z^i S_z^{i+1} - h_z S_z^i - h_x S_x^i \right) \tag{6.5}$$

The effective magnetic fields are given by:

$$h_z = 1 - \Delta/\mathcal{J} \text{ , and } \; h_x = 2\sqrt{2}J/\mathcal{J} \tag{6.6}$$

Here S_z^i and S_x^i are spin-1/2 operators for the ith spin. The term $S_z^i S_z^{i+1}$ represents the anti-ferromagnetic interaction with strength $\mathcal{J}$. In the real system, the strength of $\mathcal{J}$ is the strength of the constraint and is on the order of the interaction U. The longitudinal magnetic fields orients the direction of the spins and is determined by the energy difference between spin up and spin down. Thus it is related to the energy cost for an atom to tunnel $\Delta = E - U$. The transverse field causes the spins to flip and is therefore directly related to the atomic tunneling rate J.

The Ising Hamiltonian (Eqn. 6.5) exhibits a second order quantum phase transition between a paramagnetic and an anti-ferromagnetic ground state, for finite values of h_x. The transition is driven by quantum fluctuations caused by the non-commuting terms of the Hamiltonian h_z and h_x. The part of the phase diagram we are probing with the current experiments is the multi-critical region near $h_z \sim 1$ and finite $h_x \ll 1$ [82]. We drive the transition between the paramagnetic and anti-ferromagnetic ground states by adiabatically sweeping the longitudinal field h_z.

Spin observables

The average magnetization of the spin chain is given as the chain averaged expectation value of the spin along the longitudinal field:

$$\langle \bar{S}_z \rangle = \frac{1}{N} \sum_i \langle S_z^i \rangle \tag{6.7}$$

S_z is mapped to the atom position, so this quantity can be extracted from the fluorescent images of the tilted Mott insulator. Since the microscope is only sensitive to the parity of the on-site occupation, the paramagnetic chain $|1111\cdots\rangle$ will appear bright, whereas a perfect anti-ferromagnetic chain $|0202\cdots\rangle$ will appear completely dark. It can be shown that p_{odd} is related to S_z through the relation $\langle \bar{S}_z \rangle = p_{odd}/2$.

Another observable is the Neel order parameter for the transition that measures the long range anti-ferromagnetic ordering:

$$O = \left\langle \left(\frac{1}{2} \sum_i (-1)^i S_z^i \right)^2 \right\rangle \tag{6.8}$$

The order parameter is zero in the paramagnetic state and becomes non-zero in the anti-ferromagnetic state. Direct measurement of the order parameter requires knowledge of the exact atom number on each site, without the limitations of parity detection. In Section 7.4.1 we demonstrate a method of imaging beyond the parity limit, using a coupled bilayer system. Another approach to obtain the full number statistics is to load only a single line of atoms in each experimental run, using for example the line trap created with the DMD as described in Section 5.3. Before imaging, a short expansion along the direction perpendicular to the chain reduces the atom density to well below one atom per site so that there is a vanishing probability of sites with more than one atom. The recorded atom distribution is then summed along the expansion direction to recover the number distribution on the chain. The expansion is performed in the

conservative physics lattice, with the depth along the chain held high to prevent any tunneling along that direction.

In our previous experiment, density noise correlation measurements was used to obtain information of the order parameter [82].

6.4.2 Quantum magnetism with photon assisted tunneling

To drive the transition between the two magnetic ground states, we adiabatically change the longitudinal field. In previous experiments, this is realized by change the lattice tilt. Near the transition the tilt E compensates for the energy gap U.

With photon assisted tunneling, the photons created by modulation provides the energy to compensate for the interaction gap, and takes the role of the tilt. For a fixed initial tilt E, the critical modulation frequency happens at the $U - E$ resonance. At this modulation, frequency while the modulated tunneling is initially resonant at *every* site, once an atom has tunneled both of its neighbors are blocked by the resulting energy gap. Using modulation enables us to rapidly control the longitudinal field h_z by varying the modulation frequency ω_{mod}.

We drive the quantum phase transition by performing a Landau-Zener sweep of the modulation frequency across the $|U - E|$ resonance of the $n = 1$ shell, and subsequently *back*, adiabatically creating and destroying doublon-hole pairs. Figure 6.5 shows such a sweep, demonstrating a quantum phase transition between paramagnetic ($p_{odd} = 1$) and anti-ferromagnetic ($p_{odd} = 0$) many-body ground states. The $\sim 80\%$ conversion into doublon-hole pairs is limited by atom loss (due to the long 1 second sweep), noise on the lattice tilt, and residual lattice disorder. The transition once again demonstrates the coherence and reversibility of the modulation-driven tunneling.

The rapid tunability of the lattice modulation enables us to perform a nearly instantaneous quench of the magnetic model to the vicinity of the critical point $\omega_{mod} = E - U$.

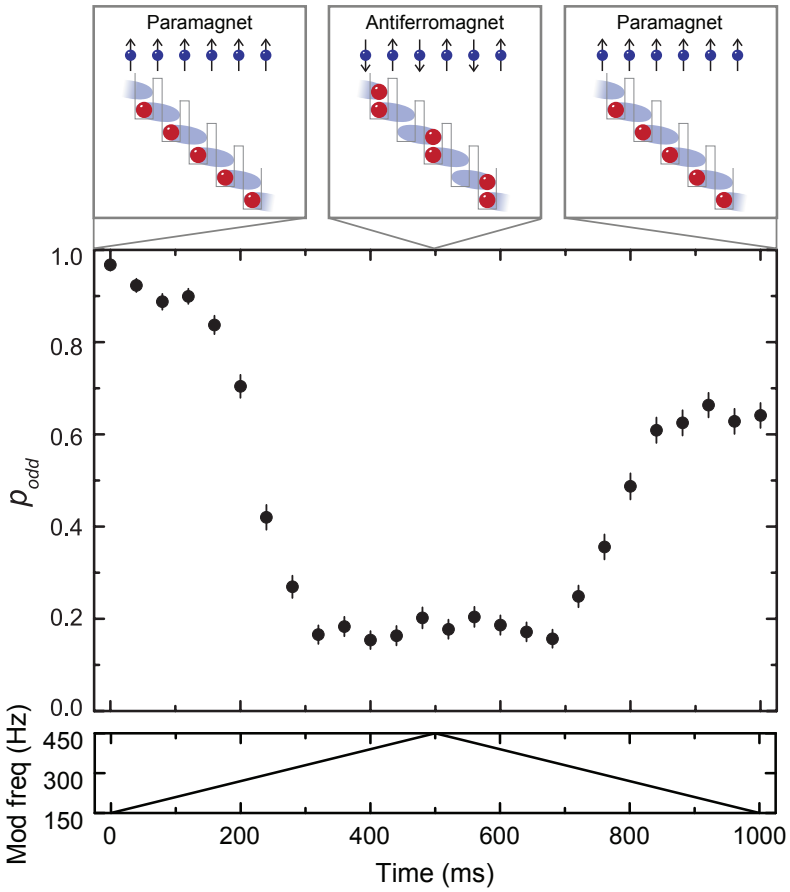

Figure 6.5: Quantum magnetism by lattice modulation. For an $n = 1$ Mott shell tilted by $E = 2\pi \times 710(25)$ Hz, the modulation frequency is chirped linearly from 150 Hz to 450 Hz and back in a total of 1 second, thus tuning through the $|U - E|$ resonance to produce doublon-hole pairs and then back to restore the double-hole pairs to singly-occupied sites (illustrated above). The magnetic model [82] maps this to a quantum phase transition from the paramagnet to an anti-ferromagnet and back. The lattice depths are $18E_r$ and $45E_r$ in the x- and y- directions, respectively, corresponding to an onsite interaction energy of $U = 2\pi \times 416(15)$ Hz. The x-lattice depth is modulated by $\pm 70\%$, producing a Bose-enhanced photon assisted tunneling rate of $2\pi \times 7.4$ Hz.

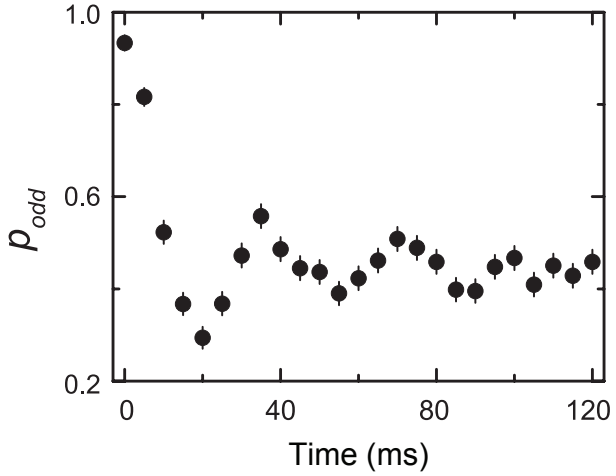

Figure 6.6: Dynamics of a many-body quench in the magnetic model, from the paramagnetic ground state to the quantum critical point. It is produced by driving at $\omega_{mod} = E - U$, for $E = 2\pi \times 890(10)$ Hz and $U = 2\pi \times 317(10)$ Hz, for a reduced x-lattice depth of $9E_r$. The photon-assisted tunneling rate (with $\pm 17\%$ lattice depth modulation) is $2\pi \times 8.1$ Hz.

The subsequent dynamics are shown in Figure 6.6, where the average magnetization of the spin chain exhibits oscillations which are damped by the many-body collective effects [88, 89]. While the fast oscillation corresponds to the spin flipping rates in the magnetic model, the damping rate at the critical point is determined by the effective system size. Comparing to results in [89], our data is consistent with chain lengths of ~ 15. The quench dynamics could also be slightly modified by residual lattice disorder.

6.5 Outlook

Using photon-assisted tunneling to induce dynamics offers substantial flexibility, because the phase, amplitude, and frequency of the tunneling may be arbitrarily controlled by changing the modulation parameters. The high resolution afforded by our quantum gas microscope also enables locally controlled photon-assisted tunneling, where the modulation is provided by a beam focused on particular sites.

We have realized occupation-sensitive control of tunneling by making use of effective multi-body interactions from multi-orbital effects. This has immediate applications in the generation of low-dimensional anyons which are particles with fractional statistics. In the proposal by Keilmann et al. [90], anyons are created by bosons in a 1D lattice with photon-assisted tunneling, and could lead to interesting phases and a statistically induced phase transition. In this scheme the statistics of the anyons can be arbitrarily tuned from bosons to fermions with the phase of the external modulation. With our quantum gas microscope, we could be able to create an anyon locally and measure its statistics by interfering with an undressed boson in time-of-flight expansions.

Naturally, photon assisted tunneling can be used to realize a variety of extended Hubbard models. For example, dominant coherent three-body interactions can be achieved, by effectively turning off the two-body interaction via lattice modulation

and leaving the multi-orbital U_3 as the leading order process [91]. On the other hand, tunable second-neighbor couplings could be engineered through multi-chromatic modulation schemes, and the dynamics of such systems could be driven and studied by time-dependent tuning of the modulation parameters.

Another important application of photon-assisted tunneling is in creating artificial gauge fields for ultracold atoms. Many of the most fascinating effects in solid state materials appear in strong magnetic fields, including the fractional quantum Hall effect [2]. Neutral atom however do not feel the Lorentz force in a magnetic field, and to simulate an effective magnetic field one could use the Coriolis force in rotation systems [92], or near-resonant Raman coupling between hyperfine states [93]. For a 2D lattice gas in a homogeneous magnetic field pointing perpendicular to the plane, the atoms (or electrons) pick up the Aharonov-Bohm phase when they move around a closed plaquette. This phase can be reproduced (and hence an artificial magnetic field created) if the tunneling matrix element in the lattice has a spatially varying phase [94, 76]. Following the proposal by Kolovsky [75], photon-assisted tunneling has been used to produce a homogeneous artificial magnetic field in 2D lattices [95, 96]. Very recently, the Meissner effect for bosons has been observed in a ladder system under uniform artificial magnetic field [97].

Chapter 7

Bilayer quantum gases under the microscope

Dimensionality plays an crucial role in the dynamics of interacting many body systems. In solid state systems, exceptional material properties can arise from reduced and mixed dimensionality. Some prominent examples include bilayer graphene [98, 99], electron-hole bilayer systems[100] and high-T_c superconductors, in which superconductivity is thought to arise from electron pairing in quasi-two-dimensional systems[101].

To date, quantum gas microscope experiments with single site resolution have been constrained to strictly two-dimensional systems [18, 16], with atoms residing in the focal plane of the imaging setup. Here, we present a scheme for high-fidelity fluorescence imaging of a bilayer system with single-site resolution. Using the combination of our axial lattice and big lattice as an optical superlattice in the out-of-plane direction, we realize a resonant system of two planes with full control over the inter-plane energy offset and tunnel coupling.

We make use of different fluorescence levels of atoms in different planes to achieve a sequential readout of the system. This also allows us to extend our imaging capabilities

for a 2D gas: we use interaction blockade to engineer transport to the second plane, to circumvent of the limitations of parity detection to resolve lattice occupation numbers of $n = 0$ to $n = 3$ in one plane. We also apply a magnetic field gradient to obtain spin-dependent transport between the planes and demonstrate spin-resolved readout.

7.1 Preparation of a resonant bilayer system

In our experiments, the quantum gases are compressed in the direction of gravity (the z-direction) in two-dimensional layers at the focus of our imaging system. After the two stage standing wave loading sequence (Sec. 3.2), the confinement in the axial (z-) direction is provided by the axial lattice with a spacing of $d = 1.5\,\mu$m and a corresponding recoil energy of $E_r = 2\pi \times 250\,$Hz. To bring two planes of the axial lattice into resonance, we turn back on the big lattice with a spacing of $9.2\,\mu$m, which now serves as a $6\times$ superlattice. The phasing between the axial lattice and the big lattice can be tuned by changing big lattice's angle of incidence. In combination with the constant gradient of $g = 2\pi \times 3.2$ kHz per axial well from gravity, we obtain a resonant double-well system in the z-direction (Fig. 7.1). The residual offset Δ between the two axial planes of interest can be tuned by varying the depth of the big lattice, while the inter-plane tunnel-coupling J is controlled by the depth of the axial lattice. All other axial planes are sufficiently offset in energy that they remain entirely unpopulated.

7.2 Imaging two planes

The primary challenges in imaging a bilayer system are the need to distinguish between the signals from each plane and the small depth of focus typical for microscopy. We obtain separate high-resolution images of the two planes by making use of two technical

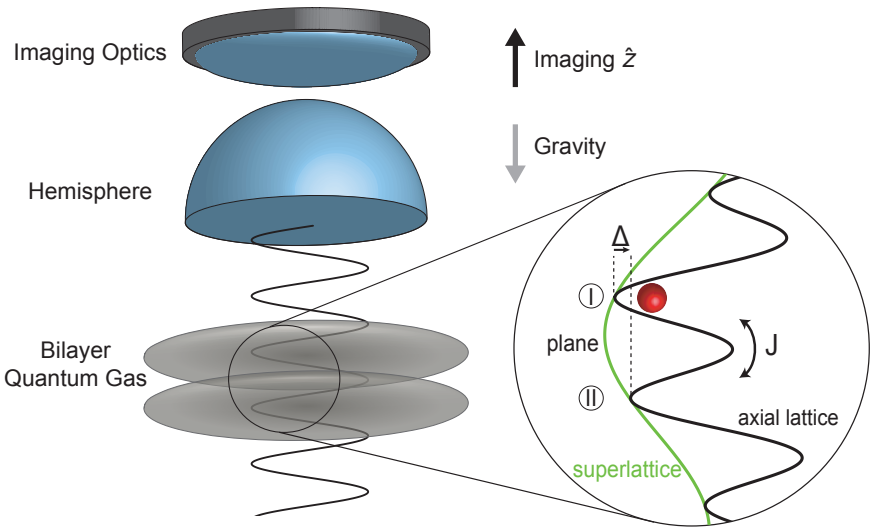

Figure 7.1: Preparation of a bilayer system. The degenerate gas of ^{87}Rb resides in two planes of the axial lattice. In combination with gravity, the axial lattice (spacing 1.5 μm) and the big lattice which acts like a 6$\times$ superlattice (spacing 9.2 μm) result in a double-well geometry with independently tunable tunnel-coupling J and offset Δ. With the 2D lattice projected onto the xy-plane, we realize a bilayer Bose-Hubbard system.

modifications: First, we shift the focus of our microscope between the two planes of interest by inserting a glass plate in the imaging path during the readout sequence. Second, we independently tune the fluorescence rates of atoms in the two planes of interest in real time, allowing us to image each plane independently.

7.2.1 The molasses configuration revisited

As described in Section 3.4 the molasses beams used for cooling in the pinning lattice are red-detuned to the D2 transition and aligned in the $lin \perp lin$ configuration along each 2D axis.

In this configuration, the molasses polarization oscillates in space between σ^+ and σ^- and the resulting light shifts form a state dependent lattice for the atoms in the two magnetic sublevels $m_F = +1/2$ and $m_F = -1/2$. As the atoms move in this state dependent potential, they are preferentially pumped from the state with higher energy to the state with lower energy and dissipate kinetic energy in the process. If no other light potentials are present, the equilibrium temperature for Sisyphus cooling in the $lin \perp lin$ configuration is on the order of the ground state light shift which scales as $I/|\delta_{mol}|$ [39]. δ_{mol} is the molasses detuning. The scattering rate, which determines the fluorescence counts we can collect, scales as I/δ_{mol}^2.

In the presence of strong confinement by the deep pinning lattice, the atoms can only move in small regions near the lattice sites. The pinning lattice is linearly polarized everywhere and state independent. Sisyphus cooling is still possible in the combined potential, where the cooling efficiency depends on the relative phase between the pinning lattice and the molasses lattice [102]. Cooling is efficient when the pinning lattice sites coincide with where the molasses potentials for $m_F = \pm 1/2$ cross, so that atoms can be pumped and cooled continuously. In our experiment, the retro-reflector is shaken to ensure all lattice sites experience uniform cooling. Since the tightly confined

atoms can only move up and down the molasses potentials over a small distance, each optical pumping process takes away less kinetic energy, comparing to the case without additional lattice where the atoms can move over a whole period of the molasses beam. Hence a higher molasses intensity might be needed to achieve efficient in-lattice cooling.

In our geometry (Fig. 3.3), the molasses beams are reflected at the *uncoated* substrate surface with a shallow angle and form standing wave patterns in the axial direction with a period of $\approx 2.8\,\mu$m.

Due to the different Fresnel coefficients, the standing wave formed by the s-polarized beam has an intensity minimum at the surface while that of the retro-reflected counter-propagating p-polarized beam has an intensity maximum at the surface. All four beams also have different intensities. This results in a particular intensity pattern for the molasses along the vertical direction, as shown in Figure 7.2 for one of the two axes of the molasses. The total intensity exhibit periodic variations in the vertical direction, so different axial plane could see different intensities and hence different fluorescence rates. We can tune the relative phase of the axial lattice and the molasses intensity pattern in the axial direction by changing the molasses incident angle, therefore changing the ratio of fluorescence rates in two adjacent axial planes.

In terms of cooling efficiency, we have now in general a $lin \perp lin$ configuration with imbalanced amplitudes of the two counter-propagating beams. A polarization gradients still exist, but instead of alternating between the two circular polarizations, the polarization will be elliptical with a changing ellipticity along the molasses axis. The difference in light shifts between the two m_F states gets smaller as the amplitude imbalance increases, and eventually the polarization gradient vanishes if one of the beams has vanishing amplitude and Sisyphus cooling stops (while scattering continues due to intensity from the remaining beam).

We have so far focused on the molasses beam along x-direction. The second beam

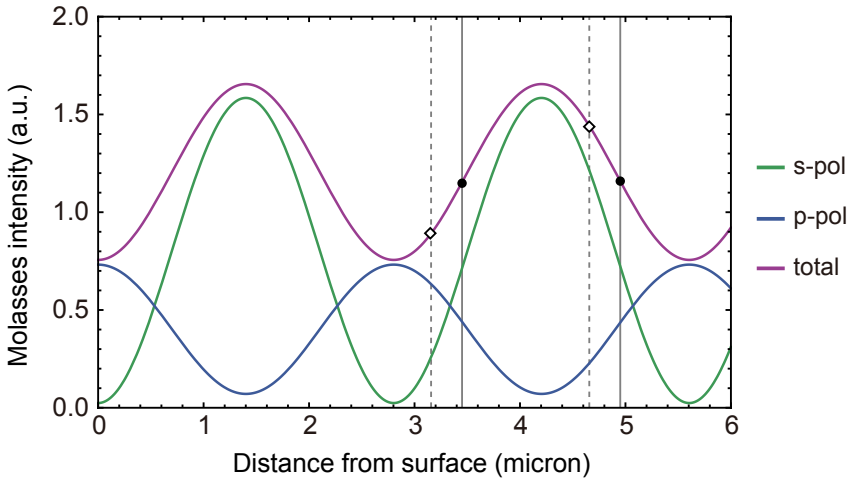

Figure 7.2: The intensity of the molasses beam in Figure 3.3 as a function of the distance to the surface, where the incident angle is set to 82°. The two polarizations each creats a standing wave but with opposite phase and different amplitude due to the Fresnel coefficients at the uncoated surface. Also shown is the total intensity which is directly related to the fluorescence rate. Sisyphus cooling is more efficient at places where the intensity of the two polarizations are similar. *Solid vertical lines:* Case where two adjacent axial planes separated by $1.5\mu m$ sits in similar molasses environment, and *Dashed vertical lines:* where the two planes have different fluorescence rates. In the experiment the atoms are about $10\mu m$ away from the surface and the phase between the axial lattice and the molasses standing wave can be varied by changing the incident angle of the molasses beam.

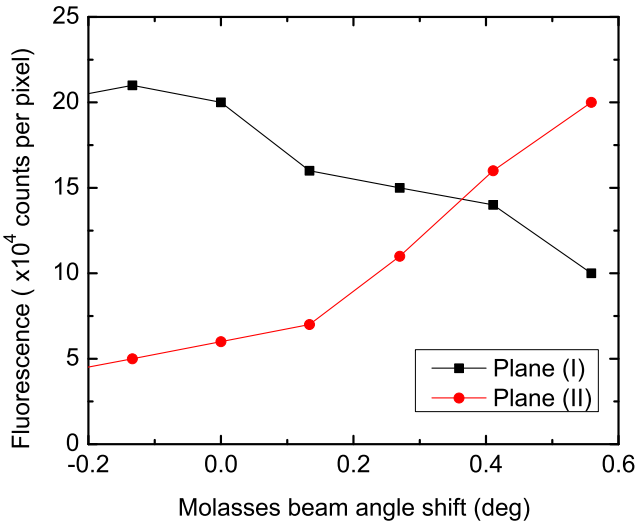

Figure 7.3: Measured fluorescence rates for atoms in two adjacent axial planes as the angle of the molasses beam is varied, showing our ability to tune the relative brightness of the two plane. Angles with large ratios in fluorescence rate, also corresponds to configurations with less efficient cooling due to the reduced polarization gradient from the imbalanced beams, and we observe decreased imaging lifetimes in the pinning lattice.

along y interferes with the first beam to create a polarization gradient and hence cooling along y. This, as well as the angle between each pair of incident and retro-reflected beam, all alters the final polarization configuration in the 2D plane of the atoms. But we expect polarization gradient cooling to work under a variety of different configurations albeit maybe with varying efficiencies [40]. In the vertical direction, we expect the discussion above and in Figure 3.3 to describe the proper qualitative behavior. This is verified in Figure 7.3, where the molasses beam's incident angle is varied (at fixed molasses power) to change the ratio between the fluorescence rates in two adjacent axial planes.

With any particular molasses configuration, the general experimental observation is that cooling and imaging works well for some intermediate molasses intensity. For

lower intensities the low fluorescence counts leads to higher noise and reduced fitting fidelity. For higher intensities, the initial fluorescence rate is high but the atoms have higher temperatures in the pinning lattice that leads to thermal hopping. This causes changes in the projected atom number distribution and atom loss due to light assisted pair collisions.

7.2.2 Imaging procedure and image analysis

The detailed procedure for imaging two planes is as follows: At the end of each experimental run, the atoms in both planes are localized in the deep pinning lattice, and cooled by the D2 molasses during the fluorescence imaging. The angle of incidence of the molasses beam is changed with a galvanometer, and we can tune the ratio of fluorescence rates in planes I and II between $1:1$ and $1:3$ in real time. At the beginning of the readout process, we image both planes at a fluorescence ratio $1:2$ for 500 ms: Atoms in plane II (high fluorescence rate), at the focus of the imaging system, are imaged primarily, while atoms in the out-of-focus plane I contribute a weak background. Next, we increase the fluorescence ratio to $1:3$ and apply a higher molasses power for 300 ms. Atoms in plane II are now heated rather than cooled by the high molasses intensity and are ejected from the pinning lattice, while atoms in plane I continue to be trapped. Simultaneously, we remove a 26 mm thick glass plate from the imaging path, shifting the focus of the imaging system to plane I. At this point, plane II has been cleared of atoms and we take a second exposure of atoms in plane I for 500 ms at an intermediate molasses power.

The atom positions in both planes can be obtained after post-processing: We first determine the positions of atoms in the second image, which contains only atoms in plane I. From the extracted distribution in plane I, we reconstruct the background contributed by these atoms to the first image. This background contribution is subtracted from

the first image to allowing us to determine the atom positions in plane II. For the fitting in both plane and the reconstruction of the background, we use separate lattice geometries and point spread functions for the atoms when focused on each plane, and also when atoms in plane I are out of focus. They are measured using images with sparsely distributed atoms. Figure 7.4 illustrates the image processing procedure.

To demonstrate our ability to image a bilayer system, we prepare decoupled two-dimensional Mott insulators of varying atom numbers in both planes. In experiments with a single plane, the big lattice is aligned so that its minimum is exactly aligned to a minimum of the axial lattice, by tuning the incident angle of the big lattice with respect to the substrate surface. Here we change the angle so that the big lattice minimum sits in between two adjacent minima of the axial lattice. Therefore when ramping up the axial lattice, the cloud is split and loaded into into exactly two adjacent axial planes. We control the ratio of the number of atoms in each plane by tuning the phase between the big lattice and the axial lattice via slight variations of the incident angle with a galvo. The 2D lattice has identical properties in both planes, and we drive the superfluid-insulator transition in the two decoupled planes simultaneously. Figure 7.4 shows one such image of Mott insulators in both planes of the axial lattice, demonstrating our ability to controllably load and image two planes of the axial lattice.

The fidelity of the readout process is primarily limited by our ability to hold atoms in plane I while imaging and ejecting atoms in plane II. For optimized parameters, the lifetime of atoms in plane I during the first exposure and ejection process is 27(2) s, resulting in a combined atom loss of 3.0% in plane I prior to imaging. The efficiency of the ejection of atoms from plane II is 99(1)%, leading to an occasional unwanted background from atoms in plane II in the second image. In combination, these effects lead to an imaging fidelity of 95% in plane I and 99% in plane II.

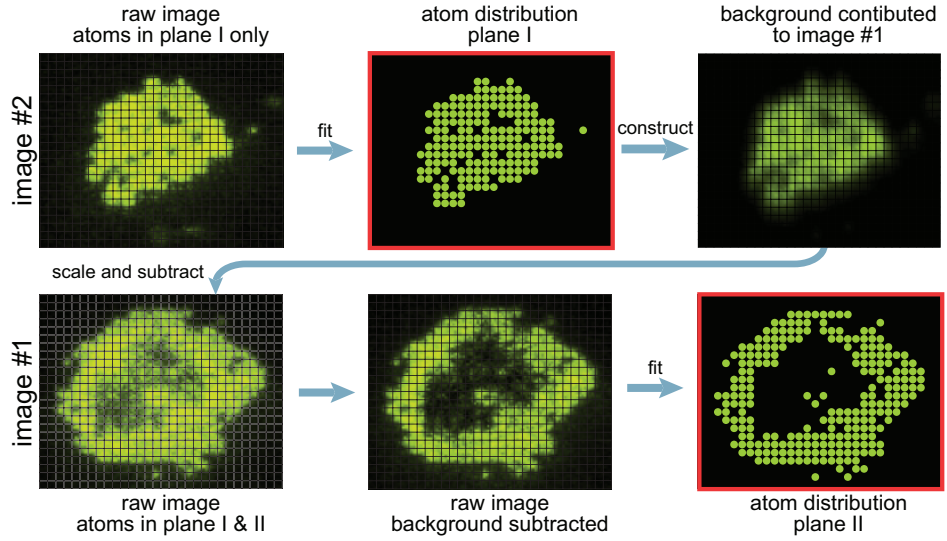

Figure 7.4: Imaging a bilayer degenerate gas. For each experimental run, two exposures are taken. After obtaining the atom distribution in plane I form image # 2, the background contributed to image # 1 can be calculated and subtracted. The resulting image yields the atom distribution in plane II. The procedure is illustrated here for decoupled Mott insulators in both planes, with up to $n = 2$ atoms per site. Red frames denote sketches of the fitted atom locations.

7.3 Coherent dynamics between resonant axial planes

We characterize the bilayer system by studying the double-well dynamics in the axial lattice direction. The experiments begin with a single-layered Mott insulator in plane I in a deep two-dimensional optical lattice, initially decoupled from plane II. Tunneling in the plane of the Mott insulator is negligible on time scales of our experiment and we concentrate on dynamics in the z-direction.

To enable tunneling between axial lattice planes, we first set the depth of the big lattice to bring planes I and II close to resonance. The axial lattice depth is then reduced from the initial $250\,E_r$ to $16\,E_r$ ($J \approx 2\pi \times 37\,\mathrm{Hz}$). After a hold time of $\tau_{hold} = 8\,\mathrm{ms}$, the axial lattice is ramped back to its original depth and we image both axial planes. Figure 7.5 (a) shows p_{odd}, the probability of odd occupancy in plane I, as a function of detuning Δ. The resonances near $\Delta = 0$ correspond to atoms tunneling within the ground band from plane I to plane II. The resonances near $\Delta \approx -2\pi \times 1.7\,\mathrm{kHz}$ correspond to atoms tunneling from the ground band in plane I to the first excited band in plane II. For both processes, the on-site interaction shift of $U \approx 2\pi \times 300\,\mathrm{Hz}$ between singly and doubly occupied sites is well-resolved. Second-order tunneling is expected to occur on a much slower timescale of $2J^2/U \approx 2\pi \times 9\,\mathrm{Hz}$ and cannot be detected due to our parity-projecting readout [103]. The horizontal scale is calibrated by measuring the offset Δ at various big lattice depths using modulation spectroscopy obtained by photon-assisted tunneling [104].

We observe coherent oscillations between axial planes by fixing the energy offset Δ at the respective resonances for singly and doubly occupied sites and varying the time τ_{hold} for which tunneling between the two planes can occur. Figure 7.5 (b) shows Rabi oscillations between the ground band of the two axial planes with respective frequencies of 114(3) Hz and 270(5) Hz. The single-particle dynamics are in good agreement with

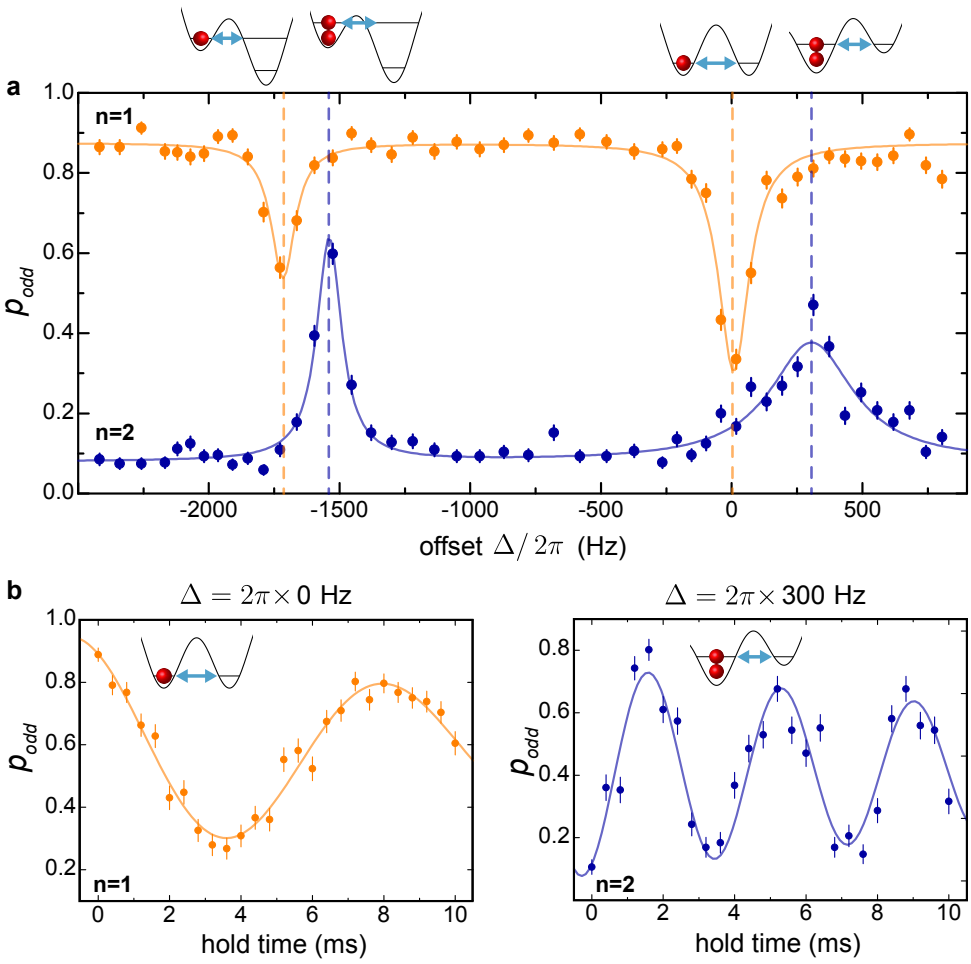

Figure 7.5: Inter-plane tunneling dynamics. **(a)** Spectrum for inter-plane tunneling. Sites with single ($n = 1$, orange) and double ($n = 2$, blue) occupancy are initially prepared in plane I. After inter-plane tunneling for $\tau_{hold} = 8\,\mathrm{ms}$ at an axial lattice depth of $16\,E_r$ ($J \approx 2\pi \times 37$ Hz), the probability to detect a single atom (p_{odd}) in plane I is measured as a function of the offset Δ. Resonances correspond to tunneling into plane II, as indicated by sketches. The interaction shift between $n = 1$ and $n = 2$ is clearly resolved ($U \approx 2\pi \times 300$ Hz). Solid lines are Lorentzian fits to the data. **(b)** Rabi oscillations for $n = 1$ and $n = 2$ at their respective ground band resonant offsets ($\Delta = 0$ and $\Delta = 2\pi \times 300$ Hz). Here, the axial lattice depth is reduced to $14.5\,E_r$, giving $J \approx 2\pi \times 55$ Hz.

a numerical diagonalization, while the rate of oscillations on doubly occupied sites is enhanced by more than a factor $\sqrt{2}$ expected from bosonic enhancement. This effect is due to a reduction of the effective barrier height when a tilt $\Delta \sim U$ is applied.

7.4 Bilayer system as imaging tools

7.4.1 Beyond parity imaging

Our technique of resonant transfer to a second axial plane can be used to circumvent the limitations imposed by parity imaging in optical lattice microscope experiments. We start by preparing a single-layered Mott insulator with singly and doubly occupied sites in plane I. With the axial tunnel coupling enabled ($J \approx 2\pi \times 48$ Hz), we sweep the offset from $\Delta = 2.1U$ to $\Delta = 0$ in 75 ms, across the tunneling resonance for doubly occupied sites. Atoms on singly occupied sites distribute over planes I and II with roughly equal probabilities. On doubly occupied sites, a single atom transitions at an offset corresponding to the on-site interaction U. The transfer of a second atom is suppressed by a collisional interaction blockade, leaving one atom in plane I and one atom in plane II [105]. At the end of the sweep we image both planes and obtain the distribution of holes, single atoms and doublons in the initial Mott insulator by adding the atom distributions from both planes. The reconstructed "wedding cake" structure of a Mott insulator is shown in Figure 7.6, for the first time combining single-site resolution [18, 16] and atom-number sensitive detection [106, 30]. Within the $n = 2$ shell the average detected atom number is 1.86, limited by the 97(1)% fidelity of separating a doublon into two planes and the slightly reduced imaging fidelity for the bilayer readout.

Next we employ our imaging technique to detect many-body ordering across a magnetic quantum phase transition in 1D tilted Mottt insulators as described in

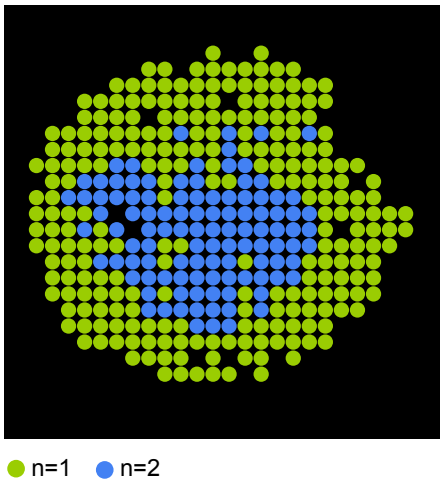

Figure 7.6: Single-shot image of the "wedding cake" structure of a two-shell Mott insulator, demonstrating the ability to image doublons using the bilayer system. After preparing a many-body state in plane I, occupation-sensitive transport of atoms to plane II allows the detection of occupancies from $n = 0$ to $n = 2$.

Section 6.4. Using a magnetic field gradient along the chains, we drive the transition from the paramagnetic state (unity filling) to the anti-ferromagnetic (density-wave ordered) state. We image the atom distribution at various points along the transition, carrying out the beyond-parity readout scheme as described above. The formation of doublon-hole pairs and anti-ferromagnetic ordering is visible in single-shot reconstructions of the atom distribution as shown in Figure 7.7. In contrast to the previous global detection of anti-ferromagnetic order noise correlation measurements [82], the ability to resolve individual doublon-hole pairs enables the direct measurement of the Neel order parameter, and detailed studies of phenomena such as domain formation, frustration and the dynamics of spin excitations in the underlying model.

A further generalization of our readout scheme allows the unambiguous detection of atom numbers $n = 0$ to $n = 3$. Using each side of the double-well as a "bit" that is either bright (odd occupancy) or dark (even occupancy) after parity projection, four

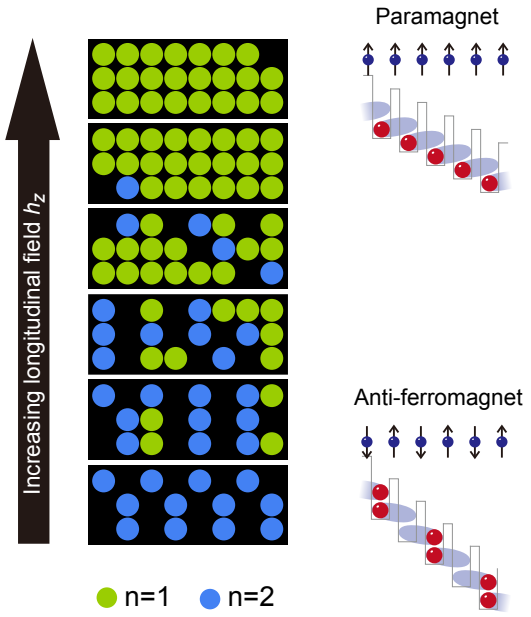

Figure 7.7: Direct imaging of many-body ordering using the bilayer scheme. One-dimensional phase transition from a paramagnetic phase to an anti-ferromagnetic phase. From top to bottom, an increasing tilt is applied horizontally along three decoupled chains of length eight, tuning the system from unity filling (top) via the formation of doublon-hole pairs (middle) to a density-wave ordered state.

different number states can be encoded. Figure 7.8 (a) illustrates the mapping for this "binary readout". After preparing a three-shell Mott insulator in plane I, we ramp the offset Δ through the resonances for $n = 2$ and $n = 3$ atoms per site, avoiding the $n = 1$ resonance at $\Delta = 0$. Figure 7.8 (b) shows p_{odd} after the ramp vs. radial distance for both planes. All plateaus of constant atom number from $n = 3$ at the center of the cloud to $n = 1$ on the outside edge can be identified.

The fidelity of the atom-number sensitive readout is limited by the small energy scales for dynamics in the z-direction. The relatively small interaction ($U \approx 2\pi \times 300$ Hz) and the large spacing of the axial lattice (1.5 μm) lead to slow dynamics and relatively high sensitivity to lattice disorder. By using a Feshbach resonance and a smaller axial lattice spacing, the robustness of the mapping process onto axial planes could be further improved for similar experiments.

7.4.2 Spin-resolved imaging

Instead of using a bilayer system to read out the site occupancies in one of the planes, we can make use of the double-well system to achieve spin-sensitive readout of a 2D gas of two-species mixture. The scheme is illustrated in Figure 7.9: A mixture of two appropriately chosen hyperfine states is initially confined to a two-dimensional system in plane I. To map out the distribution of both spin states in plane I, we enable transport between the two planes, after motion within the planes has been frozen out by a deep lattice. A magnetic field gradient in the z-direction causes atoms in one hyperfine state to transfer to plane II, while atoms in the second hyperfine state experience a force in the opposite direction and remain in plane I. The hyperfine spin degree of freedom is thus mapped to the two planes of the axial lattice, and both spin states can be imaged simultaneously.

We demonstrate spin-resolved readout for the two hyperfine states $|1, -1\rangle$ (labelled

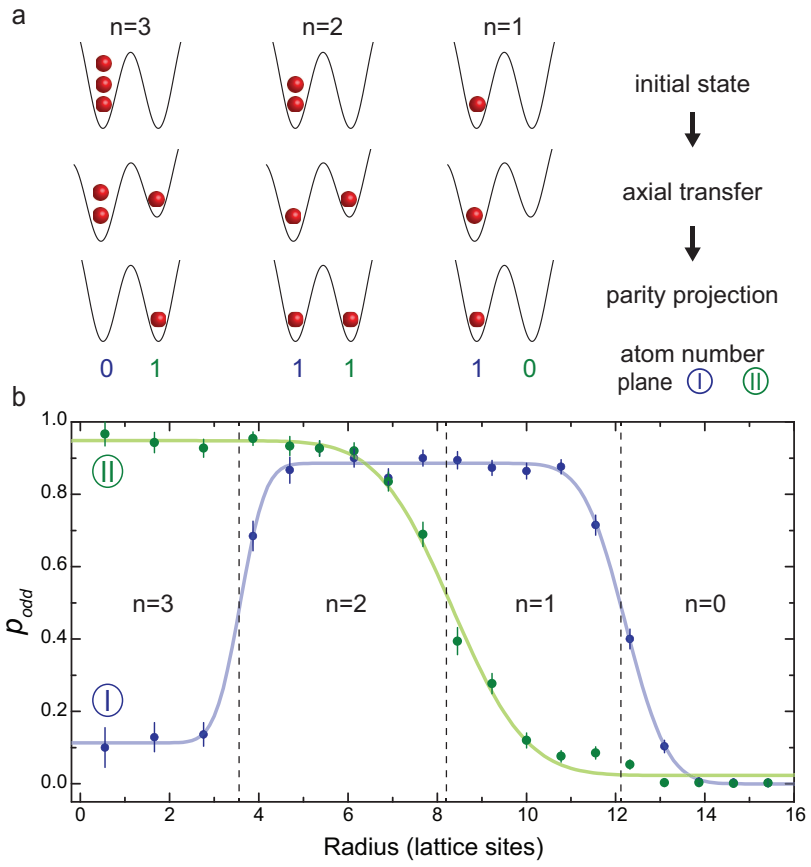

Figure 7.8: Binary readout scheme. **(a)** Occupations $n = 1$ to $n = 3$ in plane I are mapped to different distributions in plane I and II by transfer in the axial direction and parity projection. **(b)** Averaged p_{odd} in plane I (blue) and plane II (green) after preparing a three-shell Mott insulator in plane I and mapping the occupation onto axial planes. Mott-insulating regions from $n = 3$ at the trap center to $n = 1$ near the trap perimeter are resolved. The solid lines are fits with (concatenated) error functions.

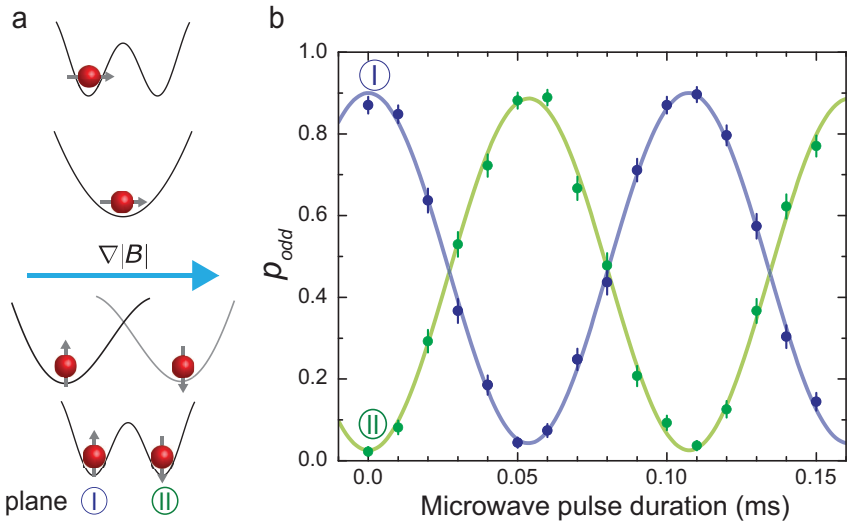

Figure 7.9: Spin-resolved readout. **(a)** Procedure for mapping the hyperfine spin onto different axial planes: After reducing the tunnel barrier in a double-well with an arbitrary spin in plane I to zero, a B-field gradient separates the $|\uparrow\rangle$ and $|\downarrow\rangle$ components into different axial planes. The two hyperfine states will appear in different planes in imaging. **(b)** A resonant microwave pulse is applied to a $n = 1$ Mott insulator in state $|\uparrow\rangle$ in plane I. The sinusoidal variation in hyperfine spin is mapped onto occupation in plane I (blue) and plane II (green). Solid lines are fits with sine functions.

$|\uparrow\rangle$) and $|2,-2\rangle$ ($|\downarrow\rangle$), for which $g_F m_F = +\frac{1}{2}$ and $g_F m_F = -1$, respectively. Initially, we prepare a $n = 1$ Mott insulator of atoms in $|\uparrow\rangle$ in plane I, and transfer atoms to the $|\downarrow\rangle$ state using a resonant microwave pulse in a bias field of 1.5 Gauss. After reducing the axial lattice depth to zero, we ramp up a magnetic field gradient of 30 Gauss/cm in the z-direction in 70 ms. While ramping the axial lattice back to its maximal depth, the magnetic field gradient causes atoms in state $|\downarrow\rangle$ to transfer to plane II, while atoms in state $|\uparrow\rangle$ remain in plane I. Figure 7.9 shows the population of both planes after mapping versus microwave pulse duration. The sinusoidal variation in anti-phase demonstrates the mapping of spin to plane degree of freedom. Taking into account imperfections in the preparation and imaging of the initial Mott insulator, the offset and amplitude of the fit yield a fidelity of 93(1)% for the microwave spin-flip (limited by magnetic field fluctuations) and a 98(1)% fidelity for the correct sorting of hyperfine spin into different axial lattice planes.

Unlike other experiments, in which only one of two spin states could be imaged *in situ*, our technique gives access to the full spin distribution in an interacting many-body system. This scheme will enable further studies of two-component systems, such as impurity dynamics [107] and collective excitations [50].

7.5 Outlook

Extensions using D1 molasses

Direct extensions to our bilayer imaging scheme could enable site-resolved detection in more than two planes. In particular, one could use additional molasses beams on the D1 line to cool all planes of atoms, and use the D2 molasses only for imaging each plane sequentially. The fluorescence filter in front of the camera blocks any molasses or scattered light on the D1 line. The two molasses can be alternatingly turned on

at frequencies on order of 1 kHz, and the duty cycle can be adjusted so that the D1 molasses provides sufficient cooling to compensate any possible heating during the D2 molasses imaging. In this configuration the intensity of the D2 molasses and the fluorescence rates can be varied over a much bigger range to achieve the best signal to noise ratio for resolving multiple planes. For imaging two adjacent planes, the dual molasses scheme would allow us to choose the D2 molasses angles and therefore the fluorescence ratios more easily without having to sacrifice imaging lifetime and fidelity. One could even envision future quantum gas microscopes where full tomography of atom number distrubution in a 3D lattice can be measured, using the sequential readout and an optical conveyer belt [108].

We have experimentally verified effective in-lattice cooling using molasses 20 MHz blue-detuned to the D1 $F = 2$ to $F' = 2$ transition, in the same configuration as our D2 molasses. The blue molasses also provides Sisyphus cooling, in this case of $F = F'$ by preferentially pumping between the internal dark and bright states [109]. The D1 molasses provides similar imaging lifetimes for a single plane compared to our regular D2 molasses, which is limited by atom loss from background gas collisions.

It should be noted that light assisted collisions also take place in blue-detuned molasses, where the atoms are excited to the repulsive molecular state instead of the attractive one in the case of red-detuned light [42]. The energy released in such a blue-photon assisted collision is about $\hbar|\delta_{mol}|$, well enough to eject the atom pair from the pinning lattice.

Spin-dependent physics

Making use of the magnetic field gradient in the z-direction, we have demonstrated spin-dependent transport and spin- and site-resolved readout of a two-species mixture.

This approach can for example facilitate the observation of anti-ferromagnetic ordering in the Fermi-Hubbard model in a fermionic quantum gas microscope [17] or spin-dependent phenomena such as spin-charge separation [50]. Following Kleine et al. [50], the latter case can be realized in strongly interacting 1D spinor gases with spin dependent interactions. In such systems where collective effects caused by interactions dominate, a single particle excitation fractionalizes into two separate collective excitations, a charge and a spin excitation. This separation could be observed as a difference in the velocities of the two types of excitations, by watching the time evolution of a single particle excitation.

Here we propose a method to produce tunable spin-dependent interaction, which could lead to experimental realization of systems with observable spin-charge separation. For ^{87}Rb the two hyperfine spin states $|1,-1\rangle$ and $|2,-2\rangle$ have almost identical scattering lengths. In a tightly confined 2D system, applying an axial magnetic field gradient pulls the two spin states slightly apart in the axial direction. The reduced wavefunction overlap leads to an reduced inter-species interaction U_{12} compare to the intra-species interaction U. For typical value of confinement in our big lattice and over the range of realistic field gradients, the ratio U_{12}/U is plotted in Figure 7.10. At the proposed interaction strengths ($U/J \sim 3$) in [50], we have reasonably fast energy scales for tunneling dynamics, with $J \sim 2\pi \times 60$ Hz and the exchange tunneling $\sim J^2/U \sim 2\pi \times 20$ Hz.

The preparation of initial states in such a spin-mixture can be realized using state dependent optical traps [110, 111], projected using the spatial light modulators discussed in Chapter 5. In particular, a tightly focused beam on a single site can be used to create the single particle excitation.

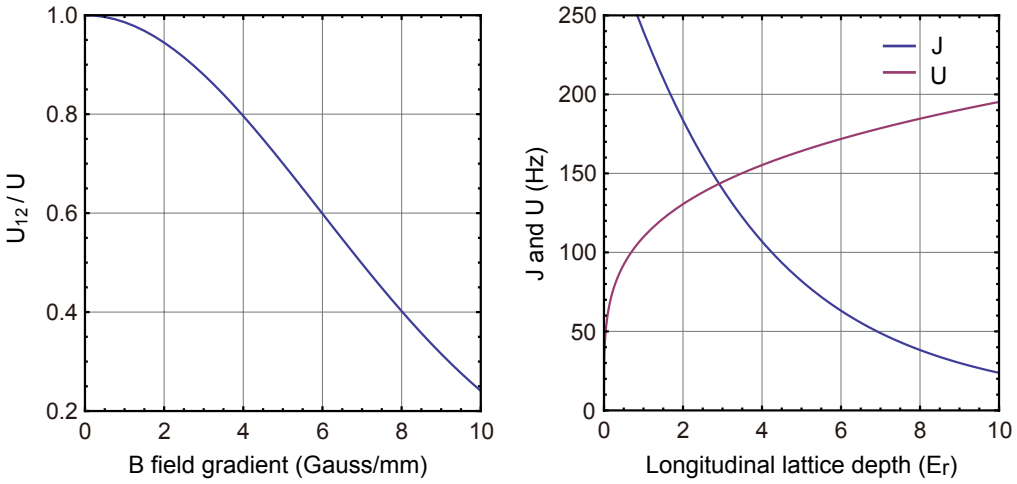

Figure 7.10: Left: Spin dependent interaction strength as a function of applied magnetic field gradient. Atoms in two different hyperfine spin states experience opposite magnetic forces and are pulled apart, leading to a reduced wavefunction overlap and therefore reduced inter-species interaction strength. Calculated for 2kHz out of plane confinement in the big lattice. Right: The values of tunneling and intra-species interaction for the same parameters, in 1D tubes created with $45E_r$ transverse lattice depth.

Other applications

Our techniques for the preparation and readout of resonant bilayer systems open numerous other possibilities for study of low-dimensional phenomena.

Interfering two planar superfluids should enable *in situ* observation of phase evolution in two dimensions and the dynamics of the Kosterlitz-Thouless phase transition [112]: By interfering the two planes, the creation and annihilation of thermally activated vortex-antivortex pairs, as well as the evolution of correlation functions can be directly imaged.

Many-body entanglement can be measured in a system of two copies of a planar system [113] and in combination with dipolar interactions [114, 115], bilayer lattice systems should exhibit supersolid phases [116] and interlayer superfluidity [117].

Our technique could also be used to reduce the entropy in two-dimensional Mott insulators. The superfluid phase with its large number fluctuations can store more entropy than the Mott insulator phase where defects are much less mobile. By having the Mott insulator in contact with a superfluid region during the transition, entropy could flow out of the Mott insulator into the superfluid [118]. Alternatively, lower entropy Mott insulators might be created by filling empty sites (defects) with atoms by merging with a reservoir plane [119].

Chapter 8

Conclusion

In this thesis, we have presented techniques and experiments to extend the toolbox in our quantum gas microscope for the generation and probing of strongly correlated many-body quantum states. These are important steps towards a reliable and versatile quantum simulator using ultracold atoms in optical lattices.

The problem of uncontrolled disorder in the lattice potential maybe somewhat specific to our system due to the projection scheme we employ for creating the optical potentials. But the spatially incoherent light sources we developed are general methods for countering the effects of imperfections in optical systems. The use of spatial light modulators allows us to achieve arbitrary wavefront shaping. The ability to use the atoms as direct probe of the aberration before actively correcting for it makes it possible to always achieve diffraction limited performance.

Starting with a clean potential, we can introduce disorder into the system by projecting disordered potential using the spatial light modulator. The high resolution would allow us to create disorder with spatial frequencies corresponding to the lattice spacing. The ability to tailor the disorder to having any spatial frequency spectra makes systematic comparison to theory a lot easier.

We have shown the use of photon assisted tunneling to probe and drive coherent dynamics in a many-body system. Creation of artificial gauge field using photon-assisted tunneling [95, 96] could bring the atoms into the high effective magnetic field limit to explore quantum Hall physics [94].

The photon assisted tunneling can be used together with the projected potential to create localize excitations in the many body system. For example amplitude modulation applied to only a single site in our 1D tilted Mott insulators would create elementary excitations in the magnetic model. In the paramagnetic state, such defects come as a single flipped spin which can hop around along the chain via a second order process. For the anti-ferromagnetic state, flipping one spin creates a domain wall which can break up into two domain boundaries each of which can move around and delocalize in the chain [120].

The creating and site-resolved imaging of tunnel coupled bilayer quantum gases open possibilities to study mixed dimensional systems, and bring new imaging capabilities for probing strongly-correlated states. By circumvent the limitations of parity imaging and obtain full number statistic, important information could be learnt about the growth of entanglement during the dynamical evolution of strongly correlated states in 1D.

Apart from these, the increasing level of control of the individual atoms in an optical lattice could lead to scalable quantum computers [121]. Gate operations between atoms on different sites could be realized using collisional phase shifts from the on-site interaction using axillary atoms, or via long range interactions such as those of atoms excited to Rydberg states.

References

[1] P. A. Lee and X.-G. Wen, "Doping a Mott insulator: Physics of high-temperature superconductivity," *Rev. Mod. Phys.* **78**, 17 (2006).

[2] H. Stormer, D. Tsui, and A. Gossard, "The fractional quantum Hall effect," *Rev. Mod. Phys.* **71**, S298 (1999).

[3] A. Auerbach, *Interacting Electrons and Quantum Magnetism* (Springer, 1994).

[4] V. Anisimov and Y. Izyumov, *Electronic Structure of Strongly Correlated Materials* (Springer, 2010).

[5] G. E. Moore *et al.*, "Cramming more components onto integrated circuits," *Proc. IEEE* **86**, 82 (1998).

[6] R. P. Feynman, "Simulating physics with computers," *Int. J. Theor. Phys.* **21**, 467 (1982).

[7] I. Bloch, J. Dalibard, and S. Nascimbène, "Quantum simulations with ultracold quantum gases," *Nature Phys.* **8**, 267 (2012).

[8] R. Blatt and C. F. Roos, "Quantum simulations with trapped ions," *Nature Phys.* **8**, 277 (2012).

[9] A. A. Houck, H. E. Türeci, and J. Koch, "On-chip quantum simulation with superconducting circuits," *Nature Phys.* **8**, 292 (2012).

[10] A. Aspuru-Guzik and P. Walther, "Photonic quantum simulators," *Nature Phys.* **8**, 285 (2012).

[11] I. Bloch, "Ultracold quantum gases in optical lattices," *Nature Phys.* **1**, 23 (2005).

[12] C. Chin, R. Grimm, P. Julienne, and E. Tiesinga, "Feshbach resonances in ultracold gases," *Rev. Mod. Phys.* **82**, 1225 (2010).

[13] M. Greiner, O. Mandel, T. Esslinger, T. W. Hänsch, and I. Bloch, "Quantum phase transition from a superfluid to a Mott insulator in a gas of ultracold atoms.," *Nature* **415**, 39 (2002).

[14] D. C. McKay and B. DeMarco, "Cooling in strongly correlated optical lattices: prospects and challenges," *Rep. Prog. Phys.* **74**, 054401 (2011).

[15] W. S. Bakr, J. I. Gillen, A. Peng, S. Fölling, and M. Greiner, "A quantum gas microscope for detecting single atoms in a Hubbard-regime optical lattice.," *Nature* **462**, 74 (2009).

[16] J. F. Sherson, C. Weitenberg, M. Endres, M. Cheneau, I. Bloch, and S. Kuhr, "Single-atom-resolved fluorescence imaging of an atomic Mott insulator.," *Nature* **467**, 68 (2010).

[17] F. Huber, *Site-resolved imaging with the Fermi gas microscope*, PhD thesis Harvard University 2014.

[18] W. S. Bakr, A. Peng, M. E. Tai, R. Ma, J. Simon, J. I. Gillen, S. Fölling, L. Pollet, and M. Greiner, "Probing the superfluid-to-Mott insulator transition at the single-atom level.," *Science* **329**, 547 (2010).

[19] M. Endres, M. Cheneau, T. Fukuhara, C. Weitenberg, P. Schauss, C. Gross, L. Mazza, M. C. Banuls, L. Pollet, I. Bloch, and S. Kuhr, "Observation of Correlated Particle-Hole Pairs and String Order in Low-Dimensional Mott Insulators," *Science* **334**, 200 (2011).

[20] M. Cheneau, P. Barmettler, D. Poletti, M. Endres, P. Schauß, T. Fukuhara, C. Gross, I. Bloch, C. Kollath, and S. Kuhr, "Light-cone-like spreading of correlations in a quantum many-body system," *Nature* **481**, 484 (2012).

[21] H. J. Metcalf and P. Straten, *Laser Cooling and Trapping* (Springer, 1999).

[22] D. Jaksch, C. Bruder, J. I. Cirac, C. W. Gardiner, and P. Zoller, "Cold bosonic atoms in optical lattices," *Phys. Rev. Lett.* **81**, 3108 (1998).

[23] K. I. Petsas, A. B. Coates, and G. Grynberg, "Crystallography of optical lattices," *Phys. Rev. A* **50**, 5173 (1994).

[24] P. Windpassinger and K. Sengstock, "Engineering novel optical lattices," *Rep. Prog. Phys.* **76**, 086401 (2013).

[25] U. Bissbort, *Dynamical effects and disorder in ultracold bosonic matter*, PhD thesis 2013.

[26] J. Weiner, V. S. Bagnato, S. Zilio, and P. S. Julienne, "Experiments and theory in cold and ultracold collisions," *Rev. Mod. Phys.* **71**, 1 (1999).

[27] P. Julienne, F. Mies, E. Tiesinga, and C. Williams, "Collisional Stability of Double Bose Condensates," *Phys. Rev. Lett.* **78**, 1880 (1997).

[28] S. Sachdev, *Quantum Phase Transitions* (Cambridge University Press, 2001).

[29] D. Rokhsar and B. Kotliar, "Gutzwiller projection for bosons," *Phys. Rev. B* **44**, 10328 (1991).

[30] G. K. Campbell, J. Mun, M. Boyd, P. Medley, A. E. Leanhardt, L. G. Marcassa, D. E. Pritchard, and W. Ketterle, "Imaging the Mott insulator shells by using atomic clock shifts.," *Science* **313**, 649 (2006).

[31] S. Fölling, A. Widera, T. Müller, F. Gerbier, and I. Bloch, "Formation of Spatial Shell Structure in the Superfluid to Mott Insulator Transition," *Phys. Rev. Lett.* **97**, 060403 (2006).

[32] W. S. Bakr, *Microscopic Studies of Quantum Phase Transitions in Optical Lattices*, PhD thesis Harvard University 2011.

[33] A. Peng, *Quantum Gas Microscope With Optical Lattice*, PhD thesis Harvard University 2010.

[34] J. I. Gillen, *The Quantum Gas Microscope*, PhD thesis Harvard University 2009.

[35] M. Greiner, I. Bloch, T. W. Hänsch, and T. Esslinger, "Magnetic transport of trapped cold atoms over a large distance," *Phys. Rev. A* **63**, 031401 (2001).

[36] T. Esslinger, I. Bloch, and T. W. Hänsch, "Bose-Einstein condensation in a quadrupole-Ioffe-configuration trap," *Phys. Rev. A* **58**, R2664 (1998).

[37] F. Gerbier and Y. Castin, "Heating rates for an atom in a far-detuned optical lattice," *Phys. Rev. A* **82**, 013615 (2010).

[38] H. Pichler, A. J. Daley, and P. Zoller, "Nonequilibrium dynamics of bosonic atoms in optical lattices: Decoherence of many-body states due to spontaneous emission," *Phys. Rev. A* **82**, 063605 (2010).

[39] J. Dalibard and C. Cohen-Tannoudji, "Laser cooling below the Doppler limit by polarization gradients: simple theoretical models," *J. Opt. Soc. Am. B* **6**, 2023 (1989).

[40] G. Grynberg and C. Robilliard, "Cold atoms in dissipative optical lattices," *Phys. Rep.* **355**, 335 (2001).

[41] T. Walker and P. Feng, "Measurements of collisions between laser-cooled atoms," *Adv. At., Mol., Opt. Phys.* **34**, 125 (1994).

[42] T. Grünzweig, a. Hilliard, M. McGovern, and M. F. Andersen, "Near-deterministic preparation of a single atom in an optical microtrap," *Nature Phys.* **6**, 951 (2010).

[43] K. D. Nelson, X. Li, and D. S. Weiss, "Imaging single atoms in a three-dimensional array," *Nature Phys.* **3**, 556 (2007).

[44] J. Billy, V. Josse, Z. Zuo, A. Bernard, B. Hambrecht, P. Lugan, D. Clément, L. Sanchez-Palencia, P. Bouyer, and A. Aspect, "Direct observation of Anderson localization of matter waves in a controlled disorder.," *Nature* **453**, 891 (2008).

[45] R. Yu, L. Yin, N. S. Sullivan, J. S. Xia, C. Huan, A. Paduan-Filho, N. F. Oliveira, S. Haas, A. Steppke, C. F. Miclea, F. Weickert, R. Movshovich, E.-D. Mun, B. L. Scott, V. S. Zapf, and T. Roscilde, "Bose glass and Mott glass of quasiparticles in a doped quantum magnet.," *Nature* **489**, 379 (2012).

[46] S. S. Kondov, W. R. McGehee, and B. DeMarco, "Interplay of disorder and interactions in an optical lattice Hubbard model," *arXiv:1305.6072* (2013).

[47] M. Shirasaki, "Virtually imaged phased array," *Fujitsu Sci. & Tech. J.* **35**, 113 (1999).

[48] W. S. Bakr, P. M. Preiss, M. E. Tai, R. Ma, J. Simon, and M. Greiner, "Orbital excitation blockade and algorithmic cooling in quantum gases," *Nature* **480**, 500 (2011).

[49] M. Knap, A. Kantian, T. Giamarchi, I. Bloch, M. D. Lukin, and E. Demler, "Probing Real-Space and Time-Resolved Correlation Functions with Many-Body Ramsey Interferometry," *Phys. Rev. Lett.* **111**, 147205 (2013).

[50] A. Kleine, C. Kollath, I. McCulloch, T. Giamarchi, and U. Schollwöck, "Spin-charge separation in two-component Bose gases," *Phys. Rev. A* **77**, 013607 (2008).

[51] A. Micheli, A. Daley, D. Jaksch, and P. Zoller, "Single Atom Transistor in a 1D Optical Lattice," *Phys. Rev. Lett.* **93**, 140408 (2004).

[52] J. Gillen, W. Bakr, A. Peng, P. Unterwaditzer, S. Fölling, and M. Greiner, "Two-dimensional quantum gas in a hybrid surface trap," *Phys. Rev. A* **80**, 021602 (2009).

[53] R. Ulichney, *Digital Halftoning* (MIT Press, 1987).

[54] R. W. Floyd and L. Steinberg, "An adaptive algorithm for spatial grey scale," *Proc. Soc. Inf. Disp.* **17**, 75 (1976).

[55] M. R. Dennis, R. P. King, B. Jack, K. OHolleran, and M. J. Padgett, "Isolated optical vortex knots," *Nature Phys.* **6**, 118 (2010).

[56] T. Čižmár, M. Mazilu, and K. Dholakia, "In situ wavefront correction and its application to micromanipulation," *Nature Photon.* **4**, 388 (2010).

[57] P. P. J. Zupancic, "Dynamic Holography and Beamshaping using Digital Micromirror Devices,", Master's thesis Ludwig-Maximilians-Universitat Munchen 2013.

[58] L. Kouwenhoven, S. Jauhar, J. Orenstein, P. McEuen, Y. Nagamune, J. Motohisa, and H. Sakaki, "Observation of Photon-Assisted Tunneling through a Quantum Dot," *Phys. Rev. Lett.* **73**, 3443 (1994).

[59] T. H. Oosterkamp, T. Fujisawa, W. G. van der Wiel, K. Ishibashi, R. V. Hijman, S. Tarucha, and L. P. Kouwenhoven, "Microwave spectroscopy of a quantum-dot molecule," *Nature* **395**, 873 (1998).

[60] S. Shapiro, "Josephson Currents in Superconducting Tunneling: The Effect of Microwaves and Other Observations," *Phys. Rev. Lett.* **11**, 80 (1963).

[61] B. Keay, S. Allen, J. Galán, J. Kaminski, K. Campman, A. Gossard, U. Bhattacharya, and M. Rodwell, "Photon-Assisted Electric Field Domains and Multiphoton-Assisted Tunneling in Semiconductor Superlattices," *Phys. Rev. Lett.* **75**, 4098 (1995).

[62] S. Wall, D. Brida, S. R. Clark, H. P. Ehrke, D. Jaksch, A. Ardavan, S. Bonora, H. Uemura, Y. Takahashi, T. Hasegawa, H. Okamoto, G. Cerullo, and A. Cavalleri, "Quantum interference between charge excitation paths in a solid-state Mott insulator," *Nature Phys.* **7**, 114 (2010).

[63] C. Sias, H. Lignier, Y. Singh, A. Zenesini, D. Ciampini, O. Morsch, and E. Arimondo, "Observation of Photon-Assisted Tunneling in Optical Lattices," *Phys. Rev. Lett.* **100**, 040404 (2008).

[64] V. Ivanov, A. Alberti, M. Schioppo, G. Ferrari, M. Artoni, M. Chiofalo, and G. Tino, "Coherent Delocalization of Atomic Wave Packets in Driven Lattice Potentials," *Phys. Rev. Lett.* **100**, 043602 (2008).

[65] E. Haller, R. Hart, M. J. Mark, J. G. Danzl, L. Reichsöllner, and H.-C. Nägerl, "Inducing Transport in a Dissipation-Free Lattice with Super Bloch Oscillations," *Phys. Rev. Lett.* **104**, 200403 (2010).

[66] R. Jördens, N. Strohmaier, K. Günter, H. Moritz, and T. Esslinger, "A Mott insulator of fermionic atoms in an optical lattice.," *Nature* **455**, 204 (2008).

[67] D. Clément, N. Fabbri, L. Fallani, C. Fort, and M. Inguscio, "Exploring Correlated 1D Bose Gases from the Superfluid to the Mott-Insulator State by Inelastic Light Scattering," *Phys. Rev. Lett.* **102**, 155301 (2009).

[68] D. Greif, L. Tarruell, T. Uehlinger, R. Jördens, and T. Esslinger, "Probing Nearest-Neighbor Correlations of Ultracold Fermions in an Optical Lattice," *Phys. Rev. Lett.* **106**, 145302 (2011).

[69] P. T. Ernst, S. Götze, J. S. Krauser, K. Pyka, D.-S. Lühmann, D. Pfannkuche, and K. Sengstock, "Probing superfluids in optical lattices by momentum-resolved Bragg spectroscopy," *Nature Phys.* **6**, 56 (2009).

[70] A. Alberti, V. V. Ivanov, G. M. Tino, and G. Ferrari, "Engineering the quantum transport of atomic wavefunctions over macroscopic distances," *Nature Phys.* **5**, 547 (2009).

[71] N. Poli, F.-Y. Wang, M. G. Tarallo, A. Alberti, M. Prevedelli, and G. M. Tino, "Precision Measurement of Gravity with Cold Atoms in an Optical Lattice and Comparison with a Classical Gravimeter," *Phys. Rev. Lett.* **106**, 038501 (2011).

[72] I. Carusotto, L. Pitaevskii, S. Stringari, G. Modugno, and M. Inguscio, "Sensitive Measurement of Forces at the Micron Scale Using Bloch Oscillations of Ultracold Atoms," *Phys. Rev. Lett.* **95**, 093202 (2005).

[73] M. Gustavsson, E. Haller, M. Mark, J. Danzl, G. Rojas-Kopeinig, and H.-C. Nägerl, "Control of Interaction-Induced Dephasing of Bloch Oscillations," *Phys. Rev. Lett.* **100**, 080404 (2008).

[74] M. Fattori, C. DErrico, G. Roati, M. Zaccanti, M. Jona-Lasinio, M. Modugno, M. Inguscio, and G. Modugno, "Atom Interferometry with a Weakly Interacting Bose-Einstein Condensate," *Phys. Rev. Lett.* **100**, 080405 (2008).

[75] A. R. Kolovsky, "Creating artificial magnetic fields for cold atoms by photon-assisted tunneling," *Europhys. Lett.* **93**, 20003 (2011).

[76] A. Sø rensen, E. Demler, and M. Lukin, "Fractional Quantum Hall States of Atoms in Optical Lattices," *Phys. Rev. Lett.* **94**, 086803 (2005).

[77] T. Kitagawa, E. Berg, M. Rudner, and E. Demler, "Topological characterization of periodically driven quantum systems," *Phys. Rev. B* **82**, 235114 (2010).

[78] M. Holthaus, "Collapse of minibands in far-infrared irradiated superlattices," *Phys. Rev. Lett.* **69**, 351 (1992).

[79] A. Zenesini, H. Lignier, D. Ciampini, O. Morsch, and E. Arimondo, "Coherent Control of Dressed Matter Waves," *Phys. Rev. Lett.* **102**, 100403 (2009).

[80] J. Struck, C. Ölschläger, R. Le Targat, P. Soltan-Panahi, A. Eckardt, M. Lewenstein, P. Windpassinger, and K. Sengstock, "Quantum simulation of frustrated classical magnetism in triangular optical lattices.," *Science* **333**, 996 (2011).

[81] Y.-A. Chen, S. Nascimbène, M. Aidelsburger, M. Atala, S. Trotzky, and I. Bloch, "Controlling Correlated Tunneling and Superexchange Interactions with ac-Driven Optical Lattices," *Phys. Rev. Lett.* **107**, 210405 (2011).

[82] J. Simon, W. S. Bakr, R. Ma, M. E. Tai, P. M. Preiss, and M. Greiner, "Quantum simulation of antiferromagnetic spin chains in an optical lattice.," *Nature* **472**, 307 (2011).

[83] S. Will, T. Best, U. Schneider, L. Hackermüller, D.-S. Lühmann, and I. Bloch, "Time-resolved observation of coherent multi-body interactions in quantum phase revivals.," *Nature* **465**, 197 (2010).

[84] P. R. Johnson, E. Tiesinga, J. V. Porto, and C. J. Williams, "Effective three-body interactions of neutral bosons in optical lattices," *New J. Phys.* **11**, 093022 (2009).

[85] D.-S. Lühmann, O. Jürgensen, and K. Sengstock, "Multi-orbital and density-induced tunneling of bosons in optical lattices," *New J. Phys.* **14**, 033021 (2012).

[86] U. Bissbort, F. Deuretzbacher, and W. Hofstetter, "Effective multibody-induced tunneling and interactions in the Bose-Hubbard model of the lowest dressed band of an optical lattice," *Phys. Rev. A* **86**, 023617 (2012).

[87] S. Sachdev, K. Sengupta, and S. Girvin, "Mott insulators in strong electric fields," *Phys. Rev. B* **66**, 075128 (2002).

[88] K. Sengupta, S. Powell, and S. Sachdev, "Quench dynamics across quantum critical points," *Phys. Rev. A* **69**, 053616 (2004).

[89] F. Meinert, M. J. Mark, E. Kirilov, K. Lauber, P. Weinmann, A. J. Daley, and H.-C. Nägerl, "Quantum Quench in an Atomic One-Dimensional Ising Chain," *Phys. Rev. Lett.* **111**, 053003 (2013).

[90] T. Keilmann, S. Lanzmich, I. McCulloch, and M. Roncaglia, "Statistically induced phase transitions and anyons in 1D optical lattices.," *Nat. Commun.* **2**, 361 (2011).

[91] A. J. Daley and J. Simon, "Effective three-body interactions via photon-assisted tunneling in an optical lattice," *arXiv:1311.1783* (2013).

[92] A. Fetter, "Rotating trapped Bose-Einstein condensates," *Rev. Mod. Phys.* **81**, 647 (2009).

[93] Y.-J. Lin, R. L. Compton, K. Jiménez-García, J. V. Porto, and I. B. Spielman, "Synthetic magnetic fields for ultracold neutral atoms.," *Nature* **462**, 628 (2009).

[94] D. Jaksch and P. Zoller, "Creation of effective magnetic fields in optical lattices: the Hofstadter butterfly for cold neutral atoms," *New J. Phys.* **5**, 56 (2003).

[95] M. Aidelsburger, M. Atala, M. Lohse, J. T. Barreiro, B. Paredes, and I. Bloch, "Realization of the Hofstadter Hamiltonian with Ultracold Atoms in Optical Lattices," *Phys. Rev. Lett.* **111**, 185301 (2013).

[96] H. Miyake, G. A. Siviloglou, C. J. Kennedy, W. C. Burton, and W. Ketterle, "Realizing the Harper Hamiltonian with Laser-Assisted Tunneling in Optical Lattices," *Phys. Rev. Lett.* **111**, 185302 (2013).

[97] M. Atala, M. Aidelsburger, M. Lohse, J. T. Barreiro, B. Paredes, and I. Bloch, "Observation of the Meissner effect with ultracold atoms in bosonic ladders," *arXiv:1402.0819* (2014).

[98] T. Ohta, A. Bostwick, T. Seyller, K. Horn, and E. Rotenberg, "Controlling the electronic structure of bilayer graphene.," *Science* **313**, 951 (2006).

[99] K. S. Novoselov, E. McCann, S. V. Morozov, V. I. Falko, M. I. Katsnelson, U. Zeitler, D. Jiang, F. Schedin, and a. K. Geim, "Unconventional quantum Hall effect and Berrys phase of 2π in bilayer graphene," *Nature Phys.* **2**, 177 (2006).

[100] J. P. Eisenstein and A. H. Macdonald, "Bose-Einstein condensation of excitons in bilayer electron systems.," *Nature* **432**, 691 (2004).

[101] J. Orenstein, "Advances in the Physics of High-Temperature Superconductivity," *Science* **288**, 468 (2000).

[102] M. D. Shotter, "Large photon number extraction from individual atoms trapped in an optical lattice," *arXiv:1011.5426* (2010).

[103] S. Fölling, S. Trotzky, P. Cheinet, M. Feld, R. Saers, A. Widera, T. Müller, and I. Bloch, "Direct observation of second-order atom tunnelling," *Nature* **448**, 1029 (2007).

[104] R. Ma, M. E. Tai, P. Preiss, W. Bakr, J. Simon, and M. Greiner, "Photon-Assisted Tunneling in a Biased Strongly Correlated Bose Gas," *Phys. Rev. Lett.* **107**, 1 (2011).

[105] P. Cheinet, S. Trotzky, M. Feld, U. Schnorrberger, M. Moreno-Cardoner, S. Fölling, and I. Bloch, "Counting atoms using interaction blockade in an optical superlattice," *Phys. Rev. Lett.* **101**, 90404 (2008).

[106] N. Gemelke, X. Zhang, C.-L. Hung, and C. Chin, "In situ observation of incompressible Mott-insulating domains in ultracold atomic gases.," *Nature* **460**, 995 (2009).

[107] T. Fukuhara, A. Kantian, M. Endres, M. Cheneau, P. Schauß, S. Hild, D. Bellem, U. Schollwöck, T. Giamarchi, C. Gross, I. Bloch, and S. Kuhr, "Quantum dynamics of a mobile spin impurity," *Nature Phys.* **9**, 235 (2013).

[108] S. Kuhr, W. Alt, D. Schrader, M. Muller, V. Gomer, and D. Meschede, "Deterministic delivery of a single atom.," *Science* **293**, 278 (2001).

[109] M. McGovern, A. J. Hilliard, T. Grünzweig, and M. F. Andersen, "Counting atoms in a deep optical microtrap.," *Opt. Lett.* **36**, 1041 (2011).

[110] O. Mandel, M. Greiner, A. Widera, T. Rom, T. W. Hänsch, and I. Bloch, "Controlled collisions for multi-particle entanglement of optically trapped atoms.," *Nature* **425**, 937 (2003).

[111] O. Mandel, M. Greiner, A. Widera, T. Rom, T. W. Hänsch, and I. Bloch, "Coherent Transport of Neutral Atoms in Spin-Dependent Optical Lattice Potentials," *Phys. Rev. Lett.* **91**, 010407 (2003).

[112] L. Mathey, K. Günter, J. Dalibard, and A. Polkovnikov, "Dynamic Kosterlitz-Thouless transition in 2D Bose mixtures of ultra-cold atoms," *arXiv:1112.1204* (2011).

[113] A. Daley, H. Pichler, and J. Schachenmayer, "Measuring entanglement growth in quench dynamics of bosons in an optical lattice," *arXiv:1205.1521* (2012).

[114] M. Lu, N. Burdick, and B. Lev, "Quantum Degenerate Dipolar Fermi Gas," *Phys. Rev. Lett.* **108**, 1 (2012).

[115] K. Aikawa, A. Frisch, M. Mark, S. Baier, A. Rietzler, R. Grimm, and F. Ferlaino, "Bose-Einstein Condensation of Erbium," *Phys. Rev. Lett.* **108**, 1 (2012).

[116] C. Trefzger, C. Menotti, and M. Lewenstein, "Pair-Supersolid Phase in a Bilayer System of Dipolar Lattice Bosons," *Phys. Rev. Lett.* **103**, 1 (2009).

[117] R. Lutchyn, E. Rossi, and S. Das Sarma, "Spontaneous interlayer superfluidity in bilayer systems of cold polar molecules," *Phys. Rev. A* **82**, 6 (2010).

[118] M. Popp, J.-J. Garcia-Ripoll, K. G. Vollbrecht, and J. I. Cirac, "Ground-state cooling of atoms in optical lattices," *Phys. Rev. A* **74**, 013622 (2006).

[119] M. C. Tichy, K. Mølmer, and J. F. Sherson, "Shaking the entropy out of a lattice: Atomic filtering by vibrational excitations," *Phys. Rev. A* **86**, 033618 (2012).

[120] J. Honer, J. C. Halimeh, I. McCulloch, U. Schollwöck, and H. P. Büchler, "Fractional excitations in cold atomic gases," *Phys. Rev. A* **86**, 051606 (2012).

[121] G. K. Brennen, C. M. Caves, P. S. Jessen, and I. H. Deutsch, "Quantum Logic Gates in Optical Lattices," *Phys. Rev. Lett.* **82**, 1060 (1999).